

Time-resolved spectroscopy of  
two-dimensional systems:  
from the conventional method to  
a novel cavity-enhanced solution

**Dissertation**

zur Erlangung des akademischen Grades doctor rerum naturalium

(Dr. rer. nat)

vorgelegt dem Rat der Chemisch-Geowissenschaftlichen Fakultät der

Friedrich-Schiller-Universität Jena



**FRIEDRICH-SCHILLER-  
UNIVERSITÄT  
JENA**

von Neus Allande Calvet  
geboren am 09.12.1989 in Barcelona

Gutachter:

1. Prof. Dr. Benjamin Dietzek-Ivanšić
2. Jun. Prof. Dr. Giancarlo Soavi

Tag der Verteidigung: 28.08.2023

# Table of contents

<b>List of abbreviations</b>	<b>V</b>
<b>Acknowledgements</b>	<b>VII</b>
<b>1 Introduction</b>	<b>1</b>
1.1 Subject matter and motivation . . . . .	1
1.2 Aim of this work . . . . .	3
1.3 Outline . . . . .	4
<b>2 Light-matter interactions</b>	<b>6</b>
2.1 Linear optics . . . . .	6
2.1.1 Semi-classical Maxwell's equations . . . . .	7
2.1.2 The material's response: optical properties of matter . . . . .	9
2.1.3 The wave equation . . . . .	10
2.1.4 Propagation of ultrashort pulses . . . . .	15
2.2 Nonlinear optics . . . . .	20
2.2.1 The wave equation in nonlinear dispersive media . . . . .	22
2.2.2 Conservation laws for photons in nonlinear optics . . . . .	23

2.2.3	Second-order nonlinearities . . . . .	26
2.2.4	Third-order nonlinearities . . . . .	31
2.3	Ultrafast spectroscopy . . . . .	38
2.3.1	Transient absorption spectroscopy (TAS) . . . . .	39
<b>3</b>	<b>Spectroscopic analysis of van der Waals heterojunctions</b>	<b>51</b>
3.1	Introduction . . . . .	51
3.1.1	Semiconductor physics . . . . .	52
3.1.2	Building a heterojunction: the system under study . . . . .	63
3.2	Methodology . . . . .	70
3.2.1	Experimental design . . . . .	70
3.2.2	Samples . . . . .	70
3.2.3	Steady state absorption measurements . . . . .	74
3.2.4	Transient absorption measurements . . . . .	75
3.3	Results . . . . .	77
3.3.1	Steady state absorption (SSA) . . . . .	77
3.3.2	Transient absorption spectroscopy (TAS) . . . . .	80
3.4	Discussion: Coupling analysis . . . . .	91
3.4.1	Indications of layer coupling . . . . .	94
3.4.2	Proposed model for the exciton dynamics . . . . .	100
3.4.3	Why only in S-het? . . . . .	102
3.5	Conclusions . . . . .	105
<b>4</b>	<b>Cavity ring-down transient absorption spectroscopy (CRD-TAS)</b>	<b>106</b>
4.1	Introduction . . . . .	106
4.1.1	Previous research and state of the art . . . . .	108
4.1.2	Theory of cavity ring-down spectroscopy (CRDS) . . . . .	110



4.1.3	The novel CRD-TAS technique . . . . .	118
4.2	The setup design . . . . .	123
4.2.1	CRD-TAS setup . . . . .	123
4.2.2	Electronic equipment . . . . .	127
4.3	The software . . . . .	131
4.3.1	The CRDS software . . . . .	131
4.3.2	The CRD-TAS software . . . . .	135
4.4	Methodology . . . . .	141
4.4.1	First steps: Characterization of the light . . . . .	141
4.4.2	CRDS measurements . . . . .	143
4.4.3	CRD-TAS measurements . . . . .	145
4.5	Results . . . . .	147
4.5.1	CRDS results . . . . .	147
4.5.2	CRD-TAS: Coherent artifacts . . . . .	151
4.5.3	CRD-TAS: Samples . . . . .	157
4.6	Discussion . . . . .	159
4.6.1	Evaluation of the steady state CRDS . . . . .	159
4.6.2	Evaluation of the CRD-TAS . . . . .	160
4.6.3	Evaluation of sample measurements . . . . .	161
4.6.4	Limitations of the CRD-TAS technique . . . . .	162
4.6.5	Further strategies for an improved CRD-TAS . . . . .	167
4.7	Conclusion . . . . .	169
<b>5</b>	<b>Summaries</b>	<b>170</b>
5.1	Summary . . . . .	170
5.2	Zusammenfassung . . . . .	173

## *TABLE OF CONTENTS*

---

Bibliography	174
Declatarion of Originality	195

# List of abbreviations

<b>0K</b>	absolute zero temperature
<b>2D</b>	two-dimensional
<b>AFM</b>	atomic force microscopy
<b>BBO</b>	beta barium borate
<b>CB</b>	conduction band
<b>CRD-TAS</b>	cavity ring-down transient absorption spec- troscopy
<b>CRDS</b>	cavity ring-down spectroscopy
<b>CT</b>	charge transfer
<b>CVD</b>	chemical vapour deposition
<b>DFG</b>	difference frequency generation
<b>DNTT</b>	<i>dinaphtho</i> [2,3- <i>b</i> :2'3'- <i>f</i> ]- <i>thieno</i> [3,2- <i>b</i> ]- <i>thiophene</i>
<b>ESA</b>	excited state absorption
<b>FWHM</b>	full width half maximum
<b>GLA</b>	global lifetime analysis
<b>GSB</b>	ground state bleach

<b>GVD</b>	group velocity dispersion
<b>HOMO</b>	highest occupied molecular orbital
<b>IRF</b>	instrument response function
<b>KK</b>	Kramers-Kronig relations
<b>LUMO</b>	lowest unoccupied molecular orbital
<b>MoS<sub>2</sub></b>	Molibdenum disulfide
<b>OPA</b>	optical parametric amplification
<b>OPG</b>	optical parametric generation
<b>OPO</b>	optical parametric oscillator
<b>SE</b>	stimulated emission
<b>SFG</b>	sum frequency generation
<b>SHG</b>	second harmonic generation
<b>SI</b>	International System of Units
<b>SNR</b>	signal to noise ratio
<b>SPM</b>	self-phase modulation
<b>SSA</b>	steady state absorption
<b>SVEA</b>	slowly varying amplitude approximation
<b>TA</b>	transient absorption
<b>TAS</b>	transient absorption spectroscopy
<b>TMD</b>	transition metal dichalcogenides
<b>TPA</b>	two-photon absorption
<b>VB</b>	valence band
<b>vdW</b>	van der Waals
<b>XPM</b>	cross-phase modulation

## Acknowledgements

To begin, I would like to acknowledge the skilful work of my collaborators and their sample preparations. Thanks to Dr. Uwe Hübner for the gold nanodisc samples, thanks to Sirri Batuhan Kalkan for the organic nanosheets, thanks to Emad Najafidehaghani and Dr. Antony George for the  $MoS_2$  and graphene samples, and to Prof. Andrey Turchanin and his group for their collaborative spirit. Thanks also to Alexandre Guilbault for working on the measuring software during his undergraduate research stay.

I continue by expressing my gratitude to the advisors and prospective reviewers of this thesis: Prof. Benjamin Dietzek-Ivanšić and Prof. Giancarlo Soavi; thank you both for your valuable advice and for always finding the time for scientific discussions. To the main supervisor of my thesis, Prof. Dietzek-Ivanšić, thank you for supporting my research activities, for your trust, and for granting me the freedom to pursue my own goals and ambitions.

I would like to thank Dr. Wolfgang Paa and Dr. Felix Herrmann-Westendorf for their explanations, trainings, and their excellent technical counselling. Additionally, I want to show appreciation to my office colleagues: Ratnadip De, Shruthi Santhosh Nair, Niklas Klosterhalfen and Heiner Schmidt, for always fostering a cooperative and friendly atmosphere in the workplace. A special thanks to Ratnadip for his corrections in the introduction and conclusion chapters, and to Niklas for correcting the German Zusammenfassung.

Lastly, I want to express my most sincere appreciation for my special persons: those who have stood by me, often from the distance, and made the most out of the little time I could give. "Gràcies" Dani, "Gràcies" Àngela, "Terima kasih" Kezia and "Danke" Tino. Our conversations are precious to me; you inspire me to reconnect with my humanity.



# Chapter 1

## Introduction

### 1.1 Subject matter and motivation

Recent advancements on thin film technology have allowed the development of atomically (or molecularly) thin layers with outstanding and unconventional semiconducting properties. The most acclaimed example of this breakthrough is the isolation of a graphene monolayer, that remained a theoretical construct until Geim and Novoselov exfoliated a single layer (graphene) sheet from graphite, with a straightforward method called the *Scotch tape technique* [1, 2]. This work was awarded with the Nobel Prize in physics in 2010 [3] and since then, two-dimensional semiconductors have been in the spotlight of modern semiconductor research [4–7], as their structure-function relationship was yet to be empirically assessed.

One of the most explored characteristics of semiconducting thin films is their optical and excitonic properties, precisely the mechanisms of charge carrier generation upon absorp-

tion of a photon, the evolution of those charges and the products of photoexcitation over time. This constitutes the analysis of the exciton dynamics of a two-dimensional system, and requires a spectroscopic method that has a time resolution in the few femtoseconds ( $10^{-15}$  s) to sub picosecond ( $10^{-12}$  s) range, as it must be able to follow every stage of the fast-paced development of the electronic configuration of the system [8, 9].

A popular tool to inquiry the excited state dynamics of a photoactive system is ultrafast transient absorption spectroscopy, which granted Zewail the Nobel Prize in Chemistry in 1999 [10, 11]. Together with the development of ultrafast lasers during the past four decades [12], the time resolution of transient absorption spectroscopic methods has increased and greatly surpassed [13] the aforementioned requirement to temporally resolve the exciton dynamics of semiconductors [9].

Reciprocally, the remarkable efforts in improving the time resolution of transient absorption spectroscopy were not accompanied by the same progress in the detection of weak transient absorption signals of condensed optically thin samples. To solve this issue, some research groups have opted for implementing lock-in amplifiers to remove periodic noises in transient absorption signals [14–16].

One may presume that a possible strategy for enhancing signals is to stack more single layers of the same semiconductor, to achieve a higher interaction length. However, this was proven to be an invalid approach, as the optical and band gap properties of bulk semiconductors greatly differ from their single-layer features. These modifications in the semiconducting behaviour are really severe: for example, the direct band gap of monolayered semiconductors of the transition metal dichalcogenide (TMD) family becomes indirect with the stacking of further layers [17]; moreover, the charge carrier mobility of organic semiconductors can increase by one order of magnitude with increments in



thickness of few nanometers ( $10^{-9}$  m) [18].

For this reason, it is imperative in the research of two-dimensional systems to develop a method that is capable of characterizing the photophysics of semiconducting layers with low optical density and/or weak transient absorption signals. The analysis of the nature of their photogenerated excitations and their relaxation pathways will allow to understand and fine-tune their optical and optoelectronic properties, and assess their utility in future avant-garde optoelectronic devices.

## 1.2 Aim of this work

The work presented in this thesis is dedicated to the characterization of the excited state dynamics of thin films through time-resolved spectroscopy, with emphasis on developing a methodology that is able to resolve weak transient absorption signals from optically thin films.

With this aim, the conventional transient absorption spectroscopy method is first utilized to characterize semiconducting monolayers and organic nanosheet semiconductors. Although these are physically thin, they present relatively strong transient absorption signals of a few mOD (units of optical density), which allows to characterize their excited state dynamics with the conventional machinery, not needing further signal enhancements or complex noise-minimizing techniques.

Nonetheless, the former does not represent the reality of detecting the transient photoexcited dynamics of few-layered systems. For this reason, the last chapter of this thesis introduces a new approach for the sensitive detection of two dimensional samples with marginal molecular extinction coefficients: A novel methodology that multiplies the

interaction length of the light with the sample, designated **cavity ring-down transient absorption spectroscopy (CRD-TAS)** [19]. Being at the present time in the midst of its development, the prospect efficiency and working capabilities of the novel CRD-TAS technique are hereby evaluated, and the strategies for further improvements are discussed.

## 1.3 Outline

In the present work, the upcoming **chapter 2** is dedicated to introduce the fundamentals of light propagation in media. With this purpose, an outlined derivation of the equations describing the linear and nonlinear interactions of light with matter is presented, highlighting the physical phenomena that engender measurable signals, influences the data collection and analysis; additionally, a detailed representation of each nonlinear process involved actively or passively in the generation of transient absorption signals is explored. At the end of chapter 2, the framework of ultrafast spectroscopy is elucidated, standing as the spinal methodology that interconnects all the chapters of this work. Hence, not only the theory is explained, but also the interpretation of signals and the technical details about the experimental setup.

**Chapter 3** is dedicated to the investigation of two-dimensional semiconductors and different configurations of van der Waals heterostructures. The introductory section of chapter 3 recaps the properties of semiconductors and junctions alongside the photophysical properties of the specific organic and inorganic molecules utilized for the construction of the investigated heterostructures. After the methodology for data retrieval is explained and the results are presented, the discussion section proceeds to assess the excitonic behaviour of the junctions under study, to ultimately elucidate the potential capabilities of the novel heterostructured system.

Finally, **chapter 4** focuses on the development of an innovative technique, cavity ring-down transient absorption spectroscopy (CRD-TAS), for the characterization of the excited state dynamics of solid-state two-dimensional samples that are optically very thin, i.e., that present a transient absorption signal that is too small to be resolved with conventional techniques. Following a short theoretical introduction, the technical peculiarities and the requirements for CRD-TAS are elucidated. Subsequently, and once the experimental layout is exposed, the experiments that allowed the characterization of the CRD-TAS setups are explained in the results section. Lastly, the current stage of development and the prospective utility of the CRD-TAS technique are carefully evaluated, and compared to the state-of-the-art alternatives for time-resolved measurements of optically thin samples.

# Chapter 2

## Interaction of light with matter.

## Theory and experimental techniques

### 2.1 Linear optics

In nature, matter responds to sunlight by reflecting, refracting or absorbing the incident light; the same happens when artificial luminaire shines on materials. Reflection and refraction are defined by classical wave theory and the Snell's law [20], that depends on the refractive indexes of the materials at play. Light absorption requires a quantum-mechanical treatment as it depends on the molecular orbitals or energy levels of the absorbing materials [21]. Regardless of the classical or quantum nature of the interaction, these processes are all described within the frame of **linear optics**, as the material response to light illumination behaves linearly with respect to the electric field of the incident light wave [22].

This linear correspondence holds no more when the material is irradiated with a laser source, especially when it consists of ultrashort pulses. Unlike light bulbs and LEDs, that emit diverging and incoherent photons, laser's stimulated emission is coherent, thus has the property of being well collimated; this high directionality makes laser emission able to propagate long distances without significant enlargement in beam profile size. On top of that, if the laser source is pulsed, a greater amount of photons are impinging in the material in a very short time, increasing the probability that the system absorbs more than one photon simultaneously.

The present introductory chapter is dedicated to explain in detail all the nonlinear optical processes that play a role in the experiments performed in this thesis. The introduction will start by setting the theoretical basis of light propagation from the Maxwell's equations, that are derived into the equations for the material's response and the dispersion relation. Subsequently, the fundamentals of nonlinear optics are explained, as well as an elaboration on the specific nonlinear processes that are involved actively (in the generation of signal) or passively (as a part of the experimental setup) in the retrieval of data presented in the later chapters. In the successive section 2.2, the experimental techniques for nonlinear spectroscopy will be outlined, focusing mostly on ultrafast spectroscopy and the specifics of transient absorption spectroscopy. Within that final section, there is a subsection dedicated to explore the extra coherent nonlinearities that appear in transient absorption signals, typically referred to as coherent artifacts.

### 2.1.1 Semi-classical Maxwell's equations

The most general description of light propagating in condensed matter is described through a semi-classical interaction by the four Maxwell's equations in (2.1) to (2.4). The semi-classical framework responds to a classical treatment of the light as an electromagnetic

field represented by the electric vector  $\mathbf{E}(\mathbf{r}, t)$  and the magnetic induction  $\mathbf{B}(\mathbf{r}, t)$ <sup>1</sup> [22]. The non-classical character arises as the quantized nature of the atomic energy levels needs to be accounted for to describe the interaction of  $\mathbf{E}(\mathbf{r}, t)$  and  $\mathbf{B}(\mathbf{r}, t)$  with matter, since classical mechanics is unable to describe electronic transitions, e.g., the resonant absorption of a photon in an atom. Moreover, this treatment contemplates a continuous description of matter in a macroscopic sense, where the atomic point charges are not treated individually but instead presenting a collective and averaged response. With this standpoint clear, three further auxiliary fields are defined that relate the influence of matter in the propagation of the electromagnetic field: the electric current density  $\mathbf{J}(\mathbf{r}, t)$ , the magnetic vector  $\mathbf{H}(\mathbf{r}, t)$ , and the electric displacement field  $\mathbf{D}(\mathbf{r}, t)$ . The latter represents the electromagnetic wave and its action on the free and bound charges of a medium [23].

In a non-magnetic material with the magnetic permeability of free space  $\mu_0 = 4\pi \cdot 10^{-7} \text{ N/A}^2$ , there is no magnetic polarization  $\mathbf{M}(\mathbf{r}, t) = 0$ , which implies that the magnetic vector becomes directly proportional to the driving magnetic field  $\mathbf{B}(\mathbf{r}, t) = \mu_0 \mathbf{H}(\mathbf{r}, t)$  [22]. Considering  $\rho$  the charge density of the material (that becomes zero in the absence of free charges), the Maxwell's equations in the International System of Units (SI) take the following form:

$$\nabla \times \mathbf{E}(\mathbf{r}, t) = - \frac{\partial}{\partial t} \mathbf{B}(\mathbf{r}, t) \quad (2.1)$$

$$\nabla \times \mathbf{B}(\mathbf{r}, t) = \mu_0 \left[ \mathbf{J}(\mathbf{r}, t) + \frac{\partial}{\partial t} \mathbf{D}(\mathbf{r}, t) \right] \quad (2.2)$$

$$\nabla \cdot \mathbf{D}(\mathbf{r}, t) = \rho \quad (2.3)$$

$$\nabla \cdot \mathbf{B}(\mathbf{r}, t) = 0 \quad (2.4)$$

---

<sup>1</sup>Notation: All magnitudes in bold correspond to vectorial quantities.

The semi-classical approach has its limitations, as it fails to rigorously describe spontaneous emission and its transition lifetimes without taking into account the quantum nature of light [24]. Nevertheless, it manages to derive results that are equivalent to a full quantum-mechanical treatment, which suffices to describe the phenomenology within the scope of this thesis.

### 2.1.2 The material's response: optical properties of matter

The electromagnetic fields described by Maxwell's equations (2.1) to (2.4) have an influence on the medium where they propagate as they separate the atomic bound charges. The electric field  $\mathbf{E}(\mathbf{r}, t)$  displaces the atomic nuclei collinearly and the electrons in the opposite direction, creating microscopic dipoles at each atom. As the driving electric field  $\mathbf{E}(\mathbf{r}, t)$  has a sinusoidal time dependency, it will trigger an oscillatory motion of the atomic dipoles in the material with the same frequency as the driving  $\mathbf{E}(\mathbf{r}, t)$  field, as long as the material response remains in the linear regime (described by equation (2.6)). This complex many-body interaction is typically simplified by the so-called Drude-Lorentz model, that interprets electrons as damped harmonic oscillators driven by the external force of the electromagnetic fields [25]. Moreover, the Born-Oppenheimer approximation is used to consider the atom nuclei to remain static, as these are much heavier than the electrons [26].

The light-driven atomic dipoles generate a macroscopic response of the medium that is characterised by a dipole moment per unit volume [20]. The mathematical description of the former introduces a new magnitude: the polarization density  $\mathbf{P}(\mathbf{r}, t)$ . This material's polarization is defined, in time domain, through the phenomenological constituent equation of the auxiliary field  $\mathbf{D}(\mathbf{r}, t)$  described in equation (2.5), where  $\varepsilon_0 = 8.85 \cdot 10^{-12} \text{ F/m}$  is the electric permittivity of free space [27].

$$\begin{aligned}
\mathbf{D}(\mathbf{r}, t) &= \varepsilon_0 \mathbf{E}(\mathbf{r}, t) + \mathbf{P}(\mathbf{r}, t) \\
&= (1 + \chi^{(1)}) \varepsilon_0 \mathbf{E}(\mathbf{r}, t)
\end{aligned}
\tag{2.5}$$

In order to remove the dependency on  $\mathbf{D}(\mathbf{r}, t)$ , equation (2.5) introduces the complex proportionality factor  $\chi^{(1)}$ , the linear susceptibility, that is strictly material-dependent and quantifies its degree of polarization<sup>2</sup> [24]. In this manner, the linear polarization  $\mathbf{P}^{(1)}(\mathbf{r}, t)$  can be uniquely defined in terms of the driving  $\mathbf{E}(\mathbf{r}, t)$  field, through the relation in equation (2.6).

$$\mathbf{P}^{(1)}(\mathbf{r}, t) = \varepsilon_0 \chi^{(1)} \mathbf{E}(\mathbf{r}, t) \tag{2.6}$$

The two former equations (2.5) and (2.6) with the scalar constant  $\chi^{(1)}$  are only valid in media that are isotropic, homogeneous, non-dispersive, and respond linearly to the external  $\mathbf{E}(\mathbf{r}, t)$  field [28]. In a more generalized picture (but still under the linear optics regime)  $\chi_{ij}^{(1)}$  is the susceptibility tensor that, in frequency ( $\omega$ ) domain, represents the Fourier transform of the linear response function of the medium  $R_{ij}^{(1)}$  to the external  $\mathbf{E}(\mathbf{r}, t)$  field, as defined in equation (2.7) [20].

$$R_{ij}^{(1)}(t) = \frac{1}{2\pi} \int_{-\infty}^{\infty} \chi_{ij}^{(1)}(\omega) e^{-i\omega t} d\omega \tag{2.7}$$

### 2.1.3 The wave equation

In this subsection, the origin of the relevant magnitudes involved in light propagation in media are discussed; however, the complete derivation of the mathematical equations is not specified in a detailed fashion. For an exhaustive connection between all the steps of

---

<sup>2</sup>All susceptibilities and response functions are assumed to have local effects only, which allows to remove the spatial dependency ( $\mathbf{r}$ ) for a more simplified picture [20].



the mathematical derivation, the reader is invited to check the cited references [20, 21, 29].

To obtain the wave equation that propagates in a media, one must take the curl of Maxwell's equation (2.1) and introduce Maxwell's equation (2.2) into it. Using also equation (2.5) to express the dependency on  $\mathbf{P}(\mathbf{r}, t)$ , and substituting the magnetic permeability by  $\mu_0 = 1/\varepsilon_0 c^2$ , the general wave equation can be written as follows [21]

$$\nabla \times \nabla \times \mathbf{E}(\mathbf{r}, t) + \frac{1}{c^2} \frac{\partial^2}{\partial t^2} \mathbf{E}(\mathbf{r}, t) = -\frac{1}{\varepsilon_0 c^2} \frac{\partial}{\partial t} \left[ \mathbf{J}(\mathbf{r}, t) + \frac{\partial}{\partial t} \mathbf{P}(\mathbf{r}, t) \right] \quad (2.8)$$

With the goal of finding physical solutions to the wave equation (2.8), the following adjustments are introduced:

- The double curl in equation (2.8) can be simplified through the classical calculus identity as demonstrated in equation (2.9); here, the first term of the equality can be neglected ( $\nabla(\nabla \cdot \mathbf{E}) = 0$ ) by using the *slowly varying amplitude approximation (SVEA)* [21]. This approach is commonly applied in linear and nonlinear optics, and assumes that the envelope of the pulse propagating through the media varies slowly in time and space, in comparison to the fast oscillating frequencies [30].

$$\nabla \times \nabla \times \mathbf{E} = \nabla(\nabla \cdot \mathbf{E}) - \nabla^2 \mathbf{E} \approx -\nabla^2 \mathbf{E} \quad (2.9)$$

- The mathematical manipulation is less cumbersome in the Fourier space, as the Fourier transformation of time derivatives become complex frequencies  $-i\omega$ , and monochromatic  $\mathbf{E}(\mathbf{r}, t)$  fields can be expressed as  $\mathbf{E}(\mathbf{r}, \omega)e^{i\omega t}$  [21, 31].
- The polarization of the materials is considered linear (for now), which allows to introduce equation (2.6).

- Use the constitutive relation (2.10) to express the current density  $\mathbf{J}(\omega, t)$  in terms of the electric field  $\mathbf{E}(\omega, t)$ , via the conductivity tensor of the medium  $\sigma_{ij}(\omega)$  [29].

$$\mathbf{J}_i(\omega, t) = \sigma_{ij}(\omega) \cdot \mathbf{E}_j(\omega, t) \quad (2.10)$$

With these considerations, the general wave equation in frequency domain takes the form of equation (2.11), that can be further simplified when applying the specific properties of the material: For example, in an isotropic and linear medium the tensorial quantities  $\chi_{ij}^{(1)}(\omega)$  and  $\sigma_{ij}(\omega)$  would become scalar, ( $\chi(\omega)$  and  $\sigma(\omega)$ ), but complex-valued in general. To simplify the mathematical relations, we work under this assumption until the end of the section<sup>3</sup>.

$$\nabla^2 \mathbf{E}_j(\mathbf{r}, \omega) = \frac{\omega^2}{c^2} \mathbf{E}_j(\mathbf{r}, \omega) \underbrace{\left[ 1 + \chi_{ij}^{(1)}(\omega) + \frac{i}{\varepsilon_0 \omega} \sigma_{ij}(\omega) \right]}_{\varepsilon(\omega)} \quad (2.11)$$

The term in equation (2.11) contained in big brackets defines a new quantity, the complex dielectric function  $\varepsilon(\omega)$ , that embodies the electrical properties of the material [21] and can be written in terms of its real and imaginary parts as  $\varepsilon(\omega) = \varepsilon'(\omega) + i\varepsilon''(\omega)$ . Through equation (2.11), one can express  $\varepsilon'(\omega)$  and  $\varepsilon''(\omega)$  as a function of the real  $\chi'(\omega)$ ,  $\sigma'(\omega)$  and imaginary  $\chi''(\omega)$ ,  $\sigma''(\omega)$  parts of the susceptibility and conductivity [32], respectively, as follows

$$\varepsilon'(\omega) = 1 + \chi'(\omega) - \sigma''(\omega) \quad (2.12)$$

$$\varepsilon''(\omega) = \frac{1}{\varepsilon_0 \omega} \sigma'(\omega) + \chi''(\omega) \quad (2.13)$$

The complex dielectric function defines the dependencies between the physical and optical properties of a material [33], as it is demonstrated hereafter, by solving the wave equation and analysing its implications.

---

<sup>3</sup>Notice that the extrapolation to anisotropic media will only require to recover the  $\{ij\}$  subscripts and treat the equalities as tensorial.

### Solutions of the wave equation

With the purpose of finding physical solutions to the wave equation (2.11), let us assume a monochromatic plane wave propagating in the media with an electric field  $\mathbf{E}_{pw}(\mathbf{r}, \omega) = \mathbf{E}(\omega)e^{i\mathbf{k}\mathbf{r}}$ , where  $\mathbf{k}$  is the complex wavevector [21]. Introducing the aforementioned  $\mathbf{E}_{pw}$  into (2.11) and taking into consideration Maxwell's equation (2.3) that infers<sup>4</sup>  $\mathbf{E} \perp \mathbf{k}$ , the wave equation (2.11) reduces to:

$$\left[ -\mathbf{k}^2 + \frac{\omega^2}{c^2} \varepsilon(\omega) \right] \mathbf{E}(\omega) = 0 \quad (2.14)$$

From equation (2.14) it is straightforward to isolate the complex wavenumber  $k(\omega) = \sqrt{|\mathbf{k}|^2}$ . This reveals the so-called **dispersion relation** presented in equation (2.15), that models the frequency dependency of the propagation of an electromagnetic field in a material.

$$k(\omega) = \frac{\omega}{c} \sqrt{\varepsilon(\omega)} = \frac{\omega}{c} \underbrace{[n(\omega) + i\kappa(\omega)]}_{\bar{n}(\omega)} \quad (2.15)$$

Therefore, transverse plane waves are solutions of the wave equation if the dispersion relation in (2.15) is fulfilled. As the dispersion relation has a clear physical meaning, it allows to define two important optical magnitudes from the real and imaginary part of  $k(\omega)$ . The quantity in brackets  $\bar{n}(\omega)$  is **the complex index of refraction** with a real part  $n(\omega)$  that is dispersive, representing the refractive index of a material, and the imaginary part  $\kappa(\omega)$ , that defines the frequency-dependent extinction coefficient caused by energy damping of the wave in the material [34]. To reveal the actual dependencies of  $n(\omega)$  and  $\kappa(\omega)$  with the optical properties of the material, let us now relate equations

---

<sup>4</sup>Implies that electromagnetic waves oscillate transversally with respect to the propagation direction.

(2.12) and (2.13) with equation (2.15).

$$\varepsilon'(\omega) = n^2(\omega) - \kappa^2(\omega) = 1 + \chi'(\omega) - \sigma''(\omega) \quad (2.16)$$

$$\varepsilon''(\omega) = n(\omega) \cdot \kappa(\omega) = \frac{1}{\varepsilon_0 \omega} \sigma'(\omega) + \chi''(\omega) \quad (2.17)$$

In this manner, equations (2.16) and (2.17) demonstrate that both the susceptibility and the conductivity of a material define its optical properties, as the refractive index and the chromatic dispersion, as well as the frequency-dependent absorption of the material are mathematically related.

### Causality of the linear response function: the Kramers-Kronig relations

$R_{ij}^{(1)}(t)$  in equation (2.7) obeys the principle of causality, which holds that the instantaneous polarization  $\mathbf{P}^{(1)}(\mathbf{r}, t)$  cannot depend on an electric field  $\mathbf{E}(\mathbf{r}, t')$  that happens in a future time  $t' > t$  [35]. From this notion of causality one can derive the Kramers-Kronig relations (KK) that, using Cauchy's theorem [36], relate the real and imaginary parts of the complex dielectric function  $\varepsilon(\omega)$  through the linear susceptibility  $\chi(\omega)$  [37]; the complete deduction of the KK relations, described in equations (2.18) with  $\mathcal{P}$  being the *Cauchy principal value* [36], can be found in the literature [32, 38, 39].

$$\varepsilon'(\omega) = \frac{2}{\pi} \mathcal{P} \int_0^\infty \frac{\bar{\omega} \varepsilon''(\bar{\omega})}{\bar{\omega}^2 - \omega^2} d\bar{\omega} + 1 \quad (2.18)$$

$$\varepsilon''(\omega) = -\frac{2}{\pi} \omega \mathcal{P} \int_0^\infty \frac{\varepsilon'(\bar{\omega}) - 1}{\bar{\omega}^2 - \omega^2} d\bar{\omega} \quad (2.19)$$

Together with the wave equation, the KK relations aid on determining the optical properties of the material [24, 33]. Moreover, the KK relations are in agreement with the Drude-Lorentz dipole oscillator model under the considerations of well-behaved physical asymptotes, which is typically done by the introduction of a damping factor [40]. This

implies that the oscillator energy does not become infinity at the resonance frequencies  $\omega_i$  or, in other words, that the imaginary part of the dielectric function  $\varepsilon''(\omega)$  behaves like a delta function in the vicinity of  $\omega_i$  [41].

### 2.1.4 Propagation of ultrashort pulses

Up to this point, the description of light propagation in media has been described for monochromatic plane waves. Although these were useful to introduce the topic, the simplification fails to represent the light-matter interaction and the material propagation of ultrashort pulsed beams. Ultrashort pulses have a temporal duration as brief as few femtoseconds, travelling through space as "wavepackets" that only contain a few cycles of the electromagnetic field oscillation under its envelope [42].

Ultrashort pulses are described mathematically through a complex Gaussian pulse shape that reproduces the temporal profile of the pulse as a Gaussian function [28]. Its electric field  $E(t)$  presented in equation (2.20) is defined by the carrier frequency  $\omega_0$ , that represents the central frequency of the pulse, and a complex field amplitude  $\tilde{E}(t)$ . The intensity profile of the pulse  $I(t)$  is the absolute square value of the electric field and represents its envelope with a full width half maximum (FWHM) corresponding to the pulse duration  $T_p$ , as described in equation (2.21) .

$$E(t) = \tilde{E}(t) \exp(i\omega_0 t) \quad (2.20)$$

$$I(t) = |E(t)|^2 = \exp \left[ -4 \ln 2 \left( \frac{t}{T_p} \right)^2 \right] \quad (2.21)$$

This approach manages to successfully represent all the physical features of pulsed beams [28]. Moreover, the FWHM of the Gaussian pulse in the Fourier space, i.e., the frequency domain, represents the bandwidth  $\Delta\omega_p$  or spectral width of the optical pulse [9]. As the

Fourier transform of a Gaussian is still Gaussian-shaped, the distribution of frequencies around the carrier frequency is also Gaussian.

**Time-bandwidth product** Since the temporal and spectral profiles of the Gaussian pulse are related through Fourier transforms, the pulse duration and its bandwidth are not defined independently. Their interconnection is a consequence of the *Heisenberg's uncertainty principle* [43], that claims that any non-commutative magnitudes (expressed as canonically conjugate operators in quantum mechanics) cannot be simultaneously determined without an inherent uncertainty [44]. The affected quantities within the framework of ultrashort pulses are time  $t$  and energy  $\mathcal{E}_\gamma$ , and the aforementioned principle entails that the product of their uncertainties has a minimum intrinsic value:  $\Delta t \Delta \mathcal{E}_\gamma > \hbar/2$  [45]. As the energy and the frequency are proportional (the energy of a photon is defined by  $\mathcal{E}_\gamma = \hbar\nu = \hbar\omega/(2\pi)$ ), given a pulse with a certain duration, there is a limit in the minimum spectral bandwidth that the pulse can have. In the case of Gaussian pulses, this limit is defined by equation (2.22) [42]; the detailed derivation of this values can be found in the textbooks<sup>5</sup>.

$$\Delta\omega_p \cdot T_p \geq 0.44 \quad (2.22)$$

If the equality in equation (2.22) holds, the pulse duration is as short as it *can* be, considering the spectral components it contains. In this scenario, the pulse is referred to as bandwidth- or transform-limited, also known as unchirped [28]; the concept of chirp will be elucidated at the end of this section.

The experimental implications of the time-bandwidth limitation are really important to account for, as the use of any spectral filter to decrease the spectral bandwidth of an optical pulse inevitably turns into an increase of its pulse duration.

---

<sup>5</sup>Specifically in [9] pages 11-12 and [46] page 38.

### Velocity of a pulse in a medium

In the presence of dispersion  $k(\omega)$ , the speed in which an electromagnetic wave propagates through the material is not uniquely defined. For this reason, it is useful to represent the higher nonlinear orders of dispersion through the Taylor expansion of  $k(\omega)$  [9, 47], as exemplified in equation (2.23)

$$k(\omega) \approx k(\omega_0) + \left. \frac{\partial k(\omega)}{\partial \omega} \right|_{\omega_0} (\omega - \omega_0) + \frac{1}{2} \left. \frac{\partial^2 k(\omega)}{\partial \omega^2} \right|_{\omega_0} (\omega - \omega_0)^2 + \dots \quad (2.23)$$

The physics inherited in the dispersion relation  $k(\omega)$  allows to define the three expansion coefficients as new magnitudes with physical significance:

- **Phase velocity**  $v_{ph}$ . The first term of the Taylor expansion of  $k(\omega)$  is related to the speed of the phase front, i.e., a surface of equal phase in the propagating medium, described as:

$$v_{ph} = \frac{\omega_0}{k(\omega_0)} \quad (2.24)$$

- **Group velocity**  $v_g$ . The velocity at which electromagnetic waves carry energy is called the group velocity  $v_g$ , and corresponds to the inverse of the second term of the Taylor expansion [48], as expressed in equation (2.25). Using the previous equation (2.15),  $v_g$  can also be expressed in terms of the complex index of refraction  $\bar{n}(\omega)$  as:

$$v_g(\omega) = \left( \left. \frac{\partial k(\omega)}{\partial \omega} \right|_{\omega_0} \right)^{-1} = \frac{c}{\bar{n}(\omega) + \omega \frac{\partial \bar{n}(\omega)}{\partial \omega}} \quad (2.25)$$

- **Group velocity dispersion (GVD)** If the wave vector was a linear function of the frequency as happens in non-dispersive media, the Taylor expansion could be

terminated with the aforementioned terms. However, that would not successfully represent light propagation in a real medium with chromatic dispersion, in which the group velocity  $v_g(\omega)$  depends on the refractive index [9]. This introduces the new variable in equation (2.26), the group velocity dispersion (GVD), that parametrizes the spreading of the frequency components over time, after passing through dispersive media, as a consequence of their different propagation velocities.

$$GVD = \left. \frac{\partial^2 k(\omega)}{\partial \omega^2} \right|_{\omega_0} \quad (2.26)$$

The GVD is an important parameter to take into account for ultrashort laser pulses, as they are composed by several frequencies that each propagate in a different group velocity (and hence, the dispersion) [20]. The effect in an optical pulse of the GVD is often referred to as **chirp**  $\xi(\omega)$ , which depends also on the thickness  $L$  of the dispersive material that it propagates through, as defined in equation (2.27), and therefore it is a cumulative measurement of the GVD [21].

$$\xi(\omega) = GVD(\omega) \cdot L \cdot \Delta\tau_p \quad (2.27)$$

Figure 2.1 demonstrates the effect of a chirp in a propagating ultrashort pulse.

**Use.** GVD greatly affects the broadband probe pulses of the transient absorption spectroscopy setup (TAS), explained in section 2.3.1. As the probe pulses are chirped, each wavelength contained in the probe spectrum will interact with the pump at a different mutual delays. For this reason, this effect needs to be accounted for in the post-processing of the data by applying a chirp correction method, before the global fitting technique can be performed.



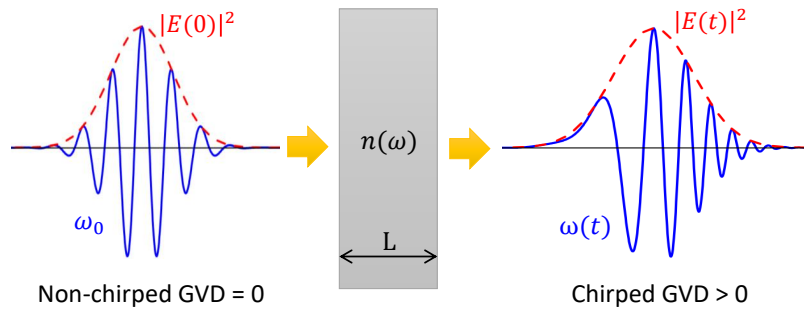


Figure 2.1: Comparison of a transform-limited Gaussian pulse (left) that, after propagating through a dispersive material, becomes chirped, and therefore with an extended pulse duration.

## 2.2 Nonlinear optics

The need for a nonlinear description of light-matter interaction was first discovered by Maria Goeppert-Mayer in 1931, who, in her doctoral thesis, presented a theoretical prediction of two-photon absorption, i.e., two photons being simultaneously absorbed in a material [49]. In such exemplary scenario, the influence of the driving  $\mathbf{E}$  field in the material could not be described by the linear response function  $R_{ij}^{(1)}(t)$  any longer, and therefore required a reformulation of the theoretical framework.

Shortly after the construction of the first operating ruby laser in 1960 by Theodore Maiman [50], the experimental manifestation of nonlinear optical effects were confirmed; almost simultaneously in 1961, Franken et al. published their paper on "Generation of Optical Harmonics", where they experimentally demonstrated second harmonic generation in crystalline quartz [51]. In parallel, Kaiser and Garret at the Bell Labs corroborated, as Maria Goeppert Maier predicted 30 years before, the experimental feasibility of two-photon absorption in a calcium fluoride window [52].

In order to trigger nonlinear effects on a medium the driving electromagnetic field must be sufficiently strong. There is no theoretically-defined threshold from which nonlinearities can be detected, but literature reports that the nonlinear response of matter is observable starting from field intensities of  $\mathbf{E}_{NL} = 3 \cdot 10^5$  V/m [53]. The electromagnetic force exerted by  $\mathbf{E}_l$  on the atoms of the material can be treated as a weak perturbation as long as the values for  $\mathbf{E}_{NL}$  lay below the minimum electric field needed to ionize the atoms. This corresponds, in average, to  $\mathbf{E}_{at} \approx 3 \cdot 10^{10}$  V/cm for the valence electrons [53]. For extremely high light intensities above the Schwinger limit of  $\mathbf{E}_S \approx 10^{18}$  V/m, the vacuum itself is expected to become nonlinear and the light-particle interactions need to be treated in the framework of quantum electrodynamics theory [54]. The former stands here only as

curiosity, as the value for  $\mathbf{E}_S$  is unattainable in the laser systems used in our experiments based on chirped pulsed amplification of titanium-sapphire oscillators.

In the regime where the external electromagnetic field  $\mathbf{E}$  lays between the aforementioned values of  $\mathbf{E}_{NL}$  and  $\mathbf{E}_{at}$ , perturbation theory is used to extrapolate towards a generalized description of the polarization through a Taylor series expansion of the linear definition from equation (2.6) [24, 55]. The definitions of the higher order susceptibilities and the electrical fields involved in the interaction take a more physically-descriptive form when written in terms of its Fourier components, as they showcase the appearance of new frequencies  $\omega_1, \omega_2, \omega_3, \dots$  generated from the nonlinear interaction. For this reason and from now onwards, the nonlinear polarization introduced in equation (2.28) is written designating its dependency on the frequencies; a more detailed explanation about the newly generated  $\omega_{1,2,\dots}$  will be exemplified in the following subsections alongside the descriptions of the specific nonlinear effects at play.

$$\begin{aligned}
\mathbf{P}_i(\omega) = & \varepsilon_0 \sum_j \chi_{ij}^{(1)}(\omega) \mathbf{E}_j(\omega) + \\
& + \varepsilon_0 \sum_j \sum_k \chi_{ijk}^{(2)}(\omega; \omega_1, \omega_2) \mathbf{E}_j(\omega_1) \mathbf{E}_k(\omega_2) + \\
& + \varepsilon_0 \sum_j \sum_k \sum_l \chi_{ijkl}^{(3)}(\omega; \omega_1, \omega_2, \omega_3) \mathbf{E}_j(\omega_1) \mathbf{E}_k(\omega_2) \mathbf{E}_l(\omega_3) \\
& + \dots
\end{aligned} \tag{2.28}$$

The nonlinear polarization of equation (2.28) takes the same significance as in the linear regime: the electromagnetic wave incident on the medium induces a phased array of dipoles, that coherently radiate electromagnetic waves at new frequencies [20]. As expressed in equation (2.28), each order of the nonlinear polarization is modelled through a different susceptibility tensor, that remains real valued provided that the frequency

$\omega$  of the driving field is far from frequencies that could be absorbed at the material, i.e., that are in resonance with transitions of the system<sup>6</sup>. In this manner,  $\chi_{ijk}^{(2)}$  is a third rank tensor (with 27 components) characterizing the second order nonlinearity,  $\chi_{ijkl}^{(3)}$  is a fourth rank tensor (with 256 components) which characterizes the third order nonlinearity, and so forth [21]. However, when applying symmetry conditions, e.g., the intrinsic permutation symmetry that allows the permutability of the  $\{jkl\}$  subscripts alongside the frequency components with subscripts  $\{123\}$ , or the structural symmetries of the material, the number of non-zero independent components of the susceptibility tensor reduces dramatically [21].

Undoubtedly, if the value of the external  $\mathbf{E}$  is well below the aforementioned value of  $\mathbf{E}_{\text{NL}}$  higher order susceptibilities  $\chi_{ij}^{(2)}$ ,  $\chi_{ijk}^{(3)}$ , etc. become negligible, and equation (2.28) is expressed only by its first line, and therefore reduces to the linear expression of equation (2.6).

### 2.2.1 The wave equation in nonlinear dispersive media

At the previous section, the retrieval of the wave equation was made in the linear regime where the nonlinear polarization  $P^{NL} = P^{(2)} + P^{(3)} + \dots$  was neglected. Obviously, this approximation cannot hold any longer when describing intense pulse propagation in nonlinear media, and the generalized wave equation from equation (2.8) has to be resolved in a different way. Nevertheless, the SVEA approximation that simplified the double curl still holds [20, 21]. In this manner, the terms of  $P_{NL}$  encapsulating the nonlinear interactions can be added into the wave equation (2.8) as a source term [56], or just by substituting into the wave equation the generalized form of  $\mathbf{D}(\mathbf{r}, t)$ , that contains the nonlinear term  $P^{NL}$ . Moreover, the total electric field  $\mathbf{E}(\mathbf{r}, t)$  and nonlinear polarization

---

<sup>6</sup>To simplify the mathematical treatment, this assumption is applied from now onwards, except if indicated otherwise.

$\mathbf{P}^{NL}(\mathbf{r}, t)$  accounting for pulses with various frequencies propagating through dispersive media can be modelled by a superposition of the magnitudes in each frequency  $\omega_n$  as exemplified in equation (2.29).

$$\begin{aligned}\mathbf{E}(\mathbf{r}, t) &= \sum_n \mathbf{E}_n(\mathbf{r}) e^{-i\omega_n t} \\ \mathbf{P}^{NL}(\mathbf{r}, t) &= \sum_n \mathbf{P}_n(\mathbf{r}) e^{-i\omega_n t}\end{aligned}\tag{2.29}$$

With all the aforementioned considerations, the final form of the wave equation that applies to Gaussian pulses interacting nonlinearly with the dispersive media as they propagate, is presented in equation (2.30) [21].

$$\nabla^2 \mathbf{E}_n(\mathbf{r}) + \frac{\omega_n^2}{c^2} \varepsilon(\omega_n) \mathbf{E}_n(\mathbf{r}) = -\frac{\omega_n^2}{\varepsilon_0 c^2} \mathbf{P}_n^{NL}(\mathbf{r})\tag{2.30}$$

Notice that the complex dielectric function  $\varepsilon(\omega_n)$  is still linear, as it is contained in the part of the wave equation that models the linear interaction, in opposition to the terms at the right side of the equation (2.30), that represent the nonlinear perturbation.

### 2.2.2 Conservation laws for photons in nonlinear optics

The laws of photon energy  $\mathcal{E}_\gamma$  and momentum  $\mathbf{k}$  conservation must be applied in order to find physically-allowed frequencies that are generated from the incident frequency. As the photon energy is defined as  $\mathcal{E}_\gamma = \hbar\omega$ , energy conservation implies that the sum of generated frequencies  $\omega_n$  must be equal to the frequency of the incident  $\mathbf{E}(\omega)$  field, as shown in equation (2.31).

### Phase-matching conditions

Momentum conservation implies that equation (2.32) must hold, relating the momentum of the incident light  $\mathbf{p} = \hbar\mathbf{k}$  and the sum of momentums of the electromagnetic waves generated through the nonlinear interaction.

$$\omega = \sum_{n=1}^{\infty} \omega_n \quad (2.31)$$

$$\mathbf{k} = \sum_{n=1}^{\infty} \mathbf{k}_n \quad (2.32)$$

The two relations in equations (2.31) and (2.32) constitute the fundamental phase-matching conditions of nonlinear optical interactions. The conversion of the incident frequency  $\omega$  into new frequencies  $\omega_n$  can only happen efficiently if the phase matching conditions are carefully selected, specially for parametric processes<sup>7</sup> where the quantum state of the medium is unchanged and the materials response is instantaneous [21, 57]. From a microscopic perspective, equation (2.32) conveys that the atomic dipoles of the material driven by  $\mathbf{E}_i(\omega)$  are in phase, and therefore the field(s) emitted by them  $\mathbf{E}_{j,k,l}(\omega)$  add coherently in the same propagation direction as  $\mathbf{E}_i(\omega)$ .

However, one has to consider that, in the realistic scenario of dispersive media, each of the frequencies  $\omega$  and  $\omega_n$  will propagate through the material with a different group velocity, so there will be a significant phase mismatch accumulated after the propagation length. The easiest way to address this complication experimentally is by using birefringent crystals [21], which are anisotropic crystalline materials that present different refraction indices for different polarizations of the incident wave<sup>8</sup>. In this manner, a birefringent crystal can be designed with a specific orientation of the crystal axis, to produce the same amount of phase delay for each of the frequencies propagating in the material, for a defined

---

<sup>7</sup>This is the case for all the nonlinear interactions described, except when specified otherwise.

<sup>8</sup>In opposition to the material's polarization  $\mathbf{P}$ , the polarization of a wave refers to the direction of the oscillation of the electric field, that is often decomposed in  $\mathbf{s}$  and  $\mathbf{p}$  directions, meaning perpendicular or parallel with respect of the incidence plane, respectively.

propagating length. This technique for phase matching is called *critical* or *angle* phase matching, as it requires a careful alignment of the crystal axis with the incoming light beam [58].

### Quasi-phase-matching

When the phase matching condition of equation (2.32) is not satisfied, the efficiency in which frequency-converted photons are generated decreases, and the output intensity in the nonlinear frequency is diminished [21].

In circumstances where the use of a birefringent material is not possible, the so-called quasi-phase-matching conditions can be used, where equation (2.32) is eased into a slightly less restrictive relation. Here,  $\Delta\mathbf{k}$  is the phase mismatch that ideally has to be as close as possible to zero  $\Delta\mathbf{k} \simeq 0$  for an efficient frequency conversion through the nonlinear optical process [20], as exemplified in figure 2.2.

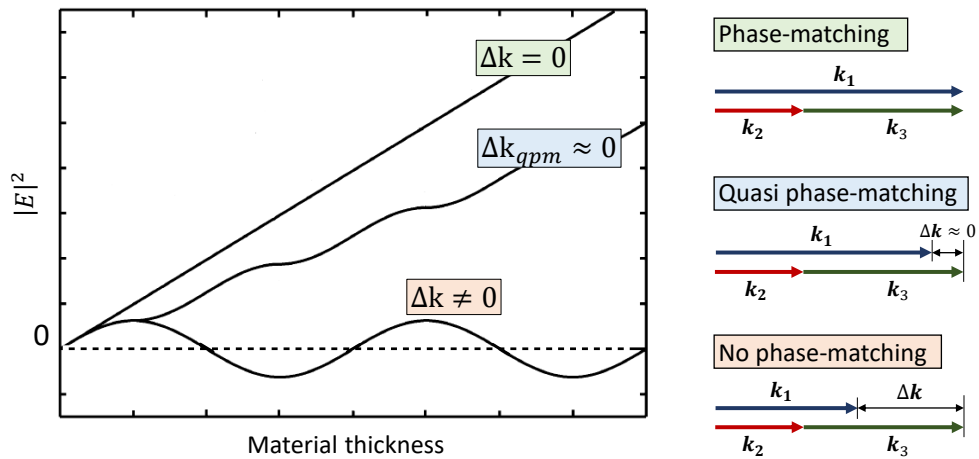


Figure 2.2: Example of the output intensity  $|E|^2$  of a second order nonlinear process as a function of the material thickness, for different phase matching conditions. The momentum vectors  $\mathbf{k}_1, \mathbf{k}_2, \mathbf{k}_3$  exemplify the case of collinear phase matching.

Quasi-phase-matching can only be achieved by implementing a periodic structure within

the nonlinear material, which adds an extra momentum contribution that is carefully tuned to reach the ideal situation where  $\Delta\mathbf{k}$  turns zero. This is typically made by periodic polling of crystals, that are designed to switch between negative and positive values of  $\chi^{(n)}$  by flipping the crystal axis at a regular interval [59]. The output intensity<sup>9</sup> of the nonlinear interaction is close to the perfect phase-matching condition and, as depicted in figure 2.2, it shows a sinusoidal modulation, that has the same periodicity as the polling of the crystal axis.

Nevertheless, there are, in general, different types of phase matching conditions that can work for a specific nonlinear effect depending on the symmetries of the materials, the order of the nonlinearity and the frequencies involved in the interaction [53].

### 2.2.3 Second-order nonlinearities

The generation of new frequencies  $\omega_1, \omega_2$  through a second-order polarization  $\mathbf{P}^{(2)}(\omega)$  requires a medium with a non-negligible second-order susceptibility tensor  $\chi_{ijk}^{(2)}$ . In practice, this can only occur in materials that do not comprise a center of inversion symmetry, which disqualifies gases, liquids, all amorphous solids, and many crystals as well, from producing any second-order nonlinear interactions. In fact, there is only one class of materials, the so-called non-centrosymmetric crystals, that can display a non-vanishing  $\chi_{ijk}^{(2)}$  and produce an efficient conversion of the fundamental (or incident) frequency  $\omega$  into new frequencies  $\omega_1, \omega_2$ .

The typical second-order nonlinear processes are sum frequency generation (SFG), where the sum of the converted frequencies  $\omega_1$  and  $\omega_2$  equals the incident frequency  $\omega$  ( $\omega = \omega_1 + \omega_2$ ) and difference frequency generation (DFG) with  $\omega = \omega_1 - \omega_2$ .

---

<sup>9</sup>The light intensity is proportional to the amplitude of the electric field, calculated as  $|E|^2$ .



### Second harmonic generation

Second harmonic generation (SHG) is the degenerate case of SFG where two photons of the incident field  $E(\omega)$  interact simultaneously in the material, generating an output frequency that is twice the incident one [58]. SHG is a nonresonant process<sup>10</sup>, i.e., the absorption of the incident photons does not trigger an electronic transition from the ground state to an actual energy level of the crystal, but instead it is interpreted as a virtual-state-assisted conversion, as depicted in figure 2.3.

The specific expressions for the second order polarization and the phase matching conditions of SHG processes take the form in equations (2.33) and (2.34), respectively.

$$\mathbf{P}_i^{(2)}(2\omega) = \varepsilon_0 \sum_{j,k} \chi_{ijk}^{(2)}(2\omega; \omega, \omega) \mathbf{E}_j(\omega) \mathbf{E}_k(\omega) \quad (2.33)$$

As all the electromagnetic fields involved in the interaction are propagating collinearly (in the same direction), the phase-matching conditions become a scalar equality [20].

$$\Delta k = k(2\omega) - 2k(\omega) \quad (2.34)$$

In SHG interactions, there are different ways to fulfil the phase matching conditions at the material, giving rise to different *types* of phase matching, that can efficiently produce a frequency-doubled output, i.e., a  $\mathbf{E}(2\omega)$  with measurable intensity [53]. In the so-called *type 0* SHG, for example, a quasi-phase matching crystal is used to combine two photons from  $E(\omega)$  with the same polarization direction, constituting one output photon with frequency  $2\omega$  and the same polarization. This interaction is modelled uniquely by the susceptibility tensor component  $\chi_{xxx}^{(2)}$ .

---

<sup>10</sup>This will be the case for all the nonlinear interactions described, except when specified otherwise.

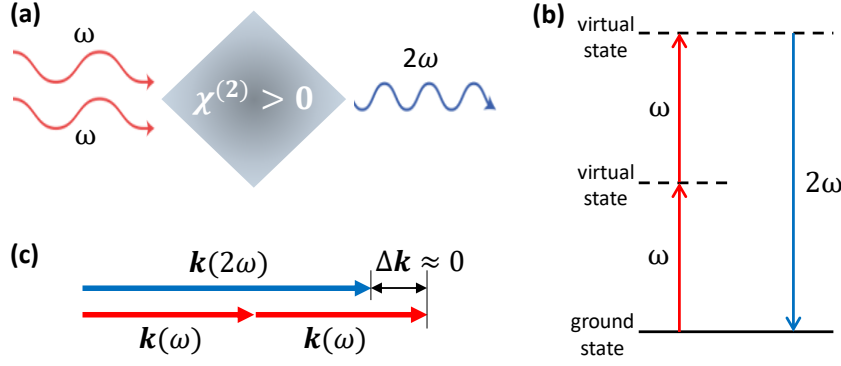


Figure 2.3: Depiction of the SHG nonlinear interaction: (a) displays the simultaneous nonresonant absorption of two photons with  $\omega$  that are frequency-doubled in a crystal with  $\chi^{(2)} > 0$  to one photon with  $2\omega$ ; the remaining fundamental is not depicted, but in general, not all incident photons are frequency-doubled. (b) Diagram of the virtual-state assisted frequency-doubling. (c) Example of a valid phase matching condition for SHG.

On the contrary, *type II* and *type III* rely purely on critical self-matching conditions and the material's polarization is modelled through different components of the susceptibility tensor: for *type I* only the susceptibility component  $\chi_{xyy}^{(2)}$  is non-zero, and for *type II* the total response is modelled through a sum of  $\chi_{xyy}^{(2)} + \chi_{yyx}^{(2)}$  [20].

**Use.** In the experimental setup for transient absorption spectroscopy, described in section 2.3.1, the fundamental wavelength of the titanium-sapphire laser (center wavelength: 800 nm) is frequency-doubled with a barium borate crystal (BBO) in a critical phase-matching fashion. As depicted in figure 2.3, the output consists of a remaining fundamental beam at 800 nm, and a powerful up-converted beam at 400 nm, that can be separated through frequency filtering (i.e., chromatic filters or dichroic mirrors). The efficient generation of coherent light through SHG, that results in a laser beam with a wavelength of 400 nm, allows to optically pump the samples of interest in their resonant frequencies.

### Optical parametric generation

Optical parametric generation (OPG), also called parametric fluorescence, is a specific case of parametric down-conversion or difference frequency generation, in which an input beam called *pump* with frequency  $\omega_p$  is converted into two lower-frequency beams, the so called *signal* and *idler* with  $\omega_s$  and  $\omega_{id}$ , respectively [60]. A graphic description of an OPG process is depicted in figure 2.4.

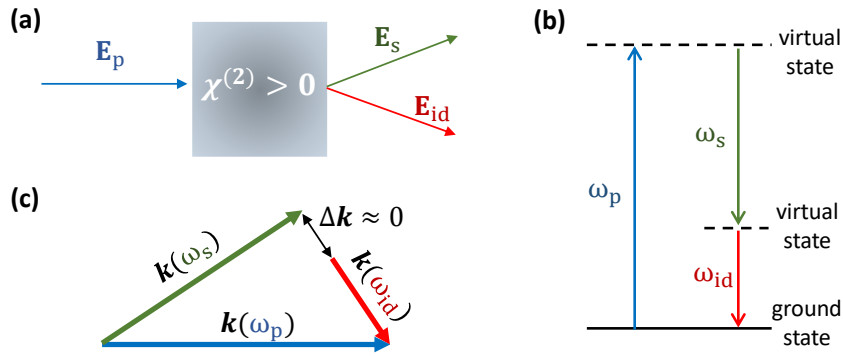


Figure 2.4: Representation of the OPG noncollinear interaction: (a) displays the down-conversion of  $E(\omega_p)$  in a crystal with  $\chi^{(2)} > 0$  to two fields  $E(\omega_s)$  and  $E(\omega_{id})$ ; the remaining nondepleted  $E(\omega_p)$  that transmits through the crystal is not depicted. (b) Diagram of the virtual-state assisted OPG. (c) Vectorial phase-matching condition for OPG.

Hence, the energy conservation of this process implies  $\omega_s = \omega_p - \omega_{id}$  [57], and the second-order polarization is represented by:

$$\mathbf{P}_i^{(2)}(\omega_s) = \varepsilon_0 \sum_{jk} \chi_{ijk}^{(2)}(\omega_s; -\omega_p, \omega_{id}) \mathbf{E}_j(-\omega_p) \mathbf{E}_k(\omega_{id}) \quad (2.35)$$

As usual, when the phase matching conditions are met, i.e.,  $\Delta \mathbf{k} = \mathbf{k}_p - (\mathbf{k}_{id} + \mathbf{k}_s) \approx 0$ , there is a high conversion efficiency of the pump frequency into powerful *signal* and *idler* beams. Thanks to the vectorial nature of  $\Delta \mathbf{k}$ , the output frequencies  $\omega_s$  and  $\omega_{id}$  can be modified by tuning the incidence angle of the pump beam with respect the optical axis of the  $\chi^{(2)}$  crystal [20].

**Amplification and tunability of the OPG signal.** The optical powers of the down-converted *signal* and *idler* are often not sufficiently high to be further employed in spectroscopy and microscopy techniques for sample characterization [61]. For this reason, the two different mechanisms explained below and shown in figure 2.5, are used to subsequently amplify a specific frequency of the *signal* beam resulting from an OPG.

**Optical parametric amplification (OPA)** is a difference-frequency generation process, in which the incident *pump*  $E(\omega_p)$  is seeded with a weak  $E(\omega_s)$  that has the desired frequency for the output *signal* beam [20]. The effect of introducing a selected  $\omega_s$  heavily restricts the freedom of the system: as  $\omega_p$  and  $\omega_s$  are defined by the input beams, energy conservation leaves no other choice for the idler frequency, as  $\omega_{id} = \omega_p - \omega_s$ . Moreover, the dipoles of the crystal responding through the  $\chi^{(2)}$  interaction, are driven to oscillate in phase with the incoming  $E(\omega_s)$ , resulting in an amplification of the output field, and the subsequent decrease in number of photons of the *pump* beam, that remains in a so-called "nondepleted" condition, as the down-conversion efficiency never reaches 100% .

OPA can be experimentally performed in multiple settings [57]. One option is to combine OPG and OPA in two steps, i.e., at two different non-centrosymmetric crystals pumped with  $E(\omega_s)$ , and using the low-intensity  $E(\omega_s)$  generated at the first step, as a *seed* beam for the second step. Alternatively, the most convenient approach that achieves a **highly-tunable OPA** is to use a chirped broadband pulse<sup>11</sup> as a *seed* beam; by mutually delaying the temporal overlap of the *pump* and broadband *seed* pulses, one can select the frequency component of the *seed* that the *pump* interacts with, allowing to obtain a range of amplified frequencies at the output.

---

<sup>11</sup>The mechanisms of supercontinuum generation of broadband pulses are explained at the next section.

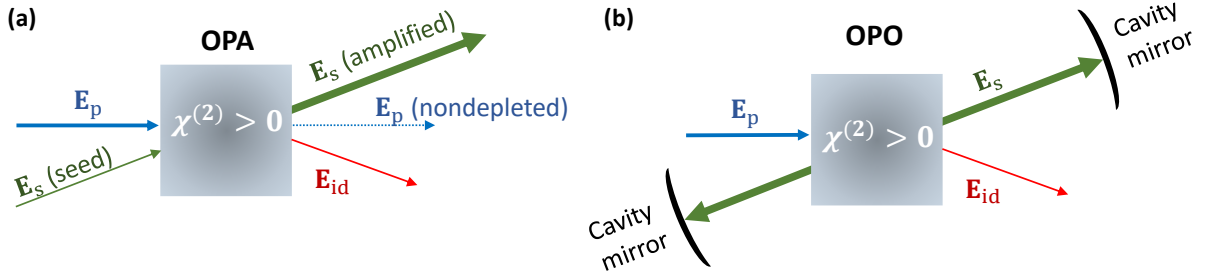


Figure 2.5: Different means of amplification of an OPG-generated *signal* beam: (a) by OPA (b) by OPO

**Optical parametric oscillator (OPO)** is a different approach for amplifying the power of the *signal* beam by combining OPG with an optical cavity. As depicted in figure 2.5, the OPG crystal is enclosed in a cavity where the *signal* beam interferes with itself producing a standing wave that has an amplified  $E(\omega_s)$  [61]. For this to happen, the cavity length has to be in resonance with the signal frequency  $\omega_s$ , in the same manner that it would be done in a laser cavity amplification [57]. If the source beams are pulsed, self-interference and the generation of the standing wave requires that the cavity length is matched with the repetition rate of the pulses. For an efficient amplification of  $E(\omega_s)$  the parametric gain at the crystal has to exceed the losses of the resonator [20].

**Use.** OPA is the most widely used method for the generation of frequency-tunable ultrashort pulses with high output powers [57, 62]. In all the experiments presented in this thesis where ultrafast spectroscopy is involved (and therefore the use of pulsed laser sources), the excitation frequencies are achieved thanks commercially available, highly-tunable OPAs.

### 2.2.4 Third-order nonlinearities

Third-order (or cubic) nonlinear processes happen in an illuminated material when the nonlinear polarization has a significant contribution of  $\chi_{ijkl}^{(3)}(\omega; \omega_1, \omega_2, \omega_3)$ . It is often

described as a four-wave mixing process, as three waves with frequencies  $\omega_1, \omega_2, \omega_3$  mix to generate a fourth wave with frequency  $\omega$  [63]. Unlike second-order processes, cubic nonlinearities can happen also in centrosymmetric materials, engendering a diverse range of nonlinear effects [21, 57]. However, the third-order nonlinear polarization  $P^{(3)}$  yields a significant contribution in non-centrosymmetric materials, where  $\chi^{(2)} = 0$ .

### Two-photon absorption

Two-photon absorption (TPA) is a third-order nonlinear response of a medium that resonantly absorbs two photons from one or two incident beams  $E(\omega_1)$ , and  $E(\omega_2)$ , and radiates one single photon with frequency  $\omega_3$  through a relaxation process that is not necessarily emissive [52].

In opposition to SHG, TPA constitutes a resonant process, as the sum of the energies of the two incident photons coincides with an optical transition of the system [57]. In other words, unlike all the other nonlinearities described in this section, TPA is a non-parametric process, as the quantum state of the system is modified upon the interaction. This translates into a complex-valued susceptibility tensor  $\tilde{\chi}^{(3)}$  with an imaginary part that models the absorption of energy at the nonlinear material [20]. As a consequence, the emitted frequency  $\omega_3$  can be, in general, not equal to the sum of the incident  $\omega_1 + \omega_2$ ; instead, there can be a portion of the input energy that remains in the system, that is generally released non-instantaneously through non-radiative processes and/or heat.

For this reason, and as depicted in figure 2.6, TPA is considered a four-wave mixing process, as the absorbed energy  $\mathcal{E}_{abs}$  has to be taken into account to fulfil energy conservation as  $\hbar\omega_1 + \hbar\omega_2 = \hbar\omega_3 + \mathcal{E}_{abs}$ .

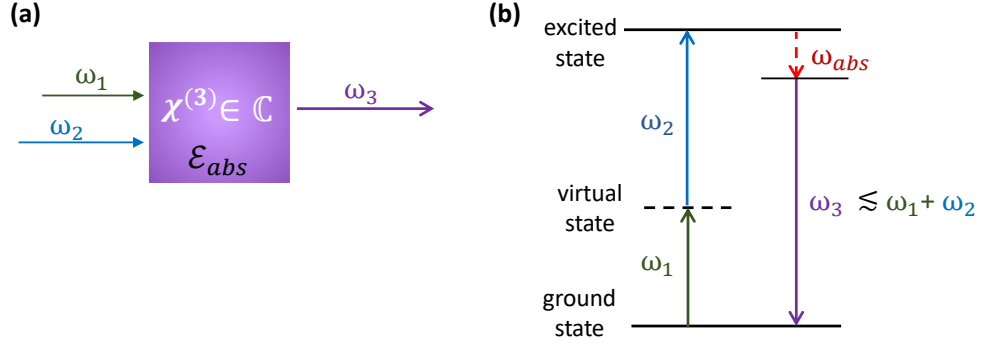


Figure 2.6: Representation of the TPA. (a) Input and output frequencies in a medium with a cubic and complex susceptibility. (b) Diagram of the TPA excitation and the subsequent relaxation involving a possible non-radiative transition assigned as  $\omega_{abs}$ .

**Use.** TPA is one of the nonlinear process contributing to the short-lived coherent artifact signal, generated (even) at the substrate material of a sample that is characterized through any kind of transient absorption technique that employs a two-pulse interaction, as will be presented in detail in section 2.3.1.

### Optical Kerr effect, self-phase modulation and white-light generation

In a centrosymmetric material (with  $\chi^{(2)} = 0$ ) and a non-negligible contribution of  $\chi^{(3)}$ , the total polarization, considering the symmetries and summation over all  $\chi_{ijkl}^{(3)}$  [21], can be expressed as:

$$P_{total}(\omega) = P^{(1)} + P^{(3)} = \varepsilon_0 E(\omega) \underbrace{\left[ \chi^{(1)} + \frac{3}{4} \chi^{(3)} |E(\omega)|^2 \right]}_{\chi_{eff}} \quad (2.36)$$

The quantity in brackets in equation (2.36) can be understood as an effective susceptibility  $\chi_{eff}$ , that contains the linear and nonlinear contributions. Considering the previous definition of the complex refractive index in equation (2.15), now applied to a transparent

( $\bar{n} = n \in \mathbb{R}$ ) and non-conductive material,  $\chi_{eff}$  is equivalent to:

$$\bar{n}^2 = (n_l + n_{nl})^2 = n_l^2 + 2n_l n_{nl} + \overbrace{n_{nl}^2}^{\approx 0} = \quad (2.37)$$

$$= 1 + \chi_{eff} = 1 + \chi^{(1)} + \frac{3}{4}\chi^{(3)}|E(\mathbf{r}, \omega)|^2 \quad (2.38)$$

Equation (2.37) reveals that the cubic polarization introduces a further nonlinear refractive index  $n_{nl}$  that depends on the amplitude of the field  $|E(\mathbf{r}, \omega)|^2$  and consequently on the instantaneous intensity of the incident pulses, as  $|E(\mathbf{r}, \omega)|^2 \propto I(\mathbf{r}, t)$ . This interaction is commonly defined as the optical **Kerr effect** [64]. The term  $n_{nl}^2$  in equation (2.37) can be neglected, as it is always orders of magnitudes lower than the linear contribution  $n_l$  [21]. In this manner, the additional nonlinear refractive index  $n_{nl}$  generated from the cubic nonlinear response of the medium under intense light irradiation is indicated in equation (2.39); the total index of refraction  $\bar{n}$  to which the propagating pulse is subjected to considering also its linear contribution  $n_l$  is presented in equation (2.40).

$$n_{nl} = \frac{3}{8n_l}\chi^{(3)} \quad (2.39)$$

$$\bar{n} = n_l + \frac{3}{8n_l}\chi^{(3)} I(\mathbf{r}, t) \quad (2.40)$$

**Self phase modulation and white-light generation.** Self-phase modulation (SPM) is a direct consequence of the intensity-dependent refractive index. In Gaussian beams the spatial profile of the propagating light has a Gaussian-shaped distribution of intensities, as depicted in figure 2.7<sup>12</sup>. The intensity of the beam is highest at the center and therefore it will generate an increased  $n_{nl}$ , with a gradual variation in the transverse plane of the

---

<sup>12</sup>Notice that a Gaussian beam is a different concept than the previously-introduced Gaussian pulse (with Gaussian temporal and frequency profile)



beam propagation. As a consequence, the light at the center of the beam propagates slower, causing a phase delay due to its own propagation or, as the name of the effect indicates, a self modulation of its own phase. This event can be also understood as a self-lensing effect, as the mere propagation of the beam affects the way it propagates, by emulating a more dispersive material as the intensity is increased. This leads to a progressive curvature of the phase front of the wave (e.g., would turn a plane wave to a spherical wave), and therefore the material itself behaves identically to a converging lens (and hence the term "focusing"), when intense beams propagate through it. This is demonstrated by figure 2.7 as the lateral size of the initial beam is decreased by the self-generated  $n_{nl}$ .

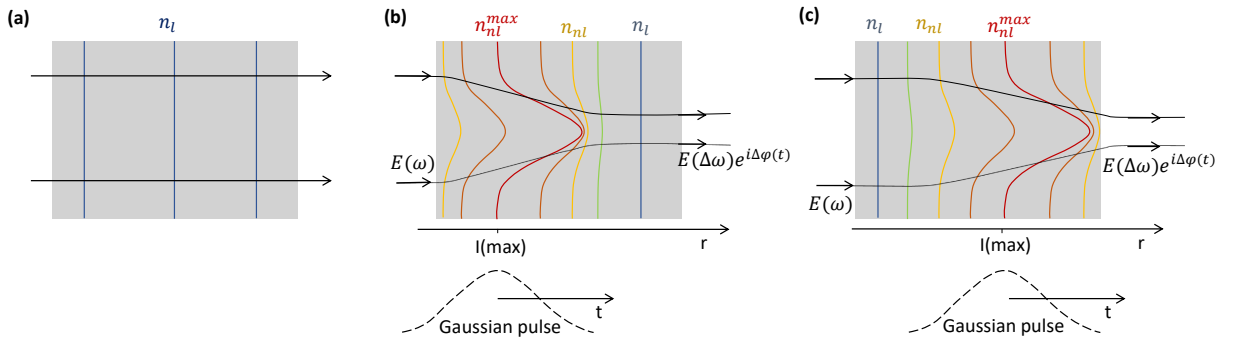


Figure 2.7: Representation of the optical Kerr effect on a medium in three different stages. a) There is no intense pulse propagating in the material. b) a Gaussian pulse enters the material propagating in  $\mathbf{r}$  direction, inducing a  $n_{nl}$  that propagates together with the temporal intensity profile (dashed line below). The Gaussian beam also has a transversal distribution of intensities spatially, originating the multiple position-dependent profiles of  $n_{nl}$  and the lensing effect, that adds new frequencies  $\Delta\omega$  through new phase components  $\Delta\phi$  (c) Idem, but in a later time, in which the pulse has propagated further inside the material.

Furthermore, the Kerr effect and SPM have even another implication: a substantial spectral broadening of the pulse known as generation of **white-light supercontin-**

**uum** [64]. The intensity-dependent  $n_{nl}$  generates a time-dependent phase shift of the propagating phase front; as the temporal derivative of the phase  $\phi$  corresponds to the instantaneous angular frequency, i.e.,  $\omega(t) = -\partial\phi_{nl}(t)/\partial t$  [56], new phase components that are time-dependent instigate newly-generated higher frequencies, and therefore a broadened spectral profile of the initial pulse that is gradual and continuous, and can easily cover the entire visible range [64].

**Use.** The generation of broadband probe pulses for the transient absorption setup utilizes the effect of white-light supercontinuum generation, performed experimentally on a calcium fluoride plate, but it is also commonly performed on sapphire or a KDP (potassium deuterium phosphate) crystal [65]. This method is the most commonly used for obtaining chirped broadband pulses with a bandwidth that covers the visible spectrum and part of the UV, when generated from a fundamental 800 nm wavelength; moreover it maintains the same properties of the fundamental input regarding collimation and coherence.

### Cross-phase modulation

Cross-phase modulation (XPM) is the same physical interaction as SPM, as it also relies on the Kerr effect. In contrast to SPM, XPM happens in a material when two distinct pulses temporally and spatially overlap in it, typically an intense pump pulse, that heavily modifies the material introducing the additional  $n_{nl}$ , and a weaker probe pulse. XPM characterizes how the material modification (i.e., Kerr effect) introduced by the pump affects the propagation of the probe, and therefore it pays attention only to the changes in  $E_{probe}$ , as represented in figure 2.8(b).

**Use.** Together with TPA, XPM is another nonlinearity contributing to the overall coherent artifact of transient absorption measurements. In chapter 4, the aforementioned nonlinear contributions will be characterized in different transparent substrates.

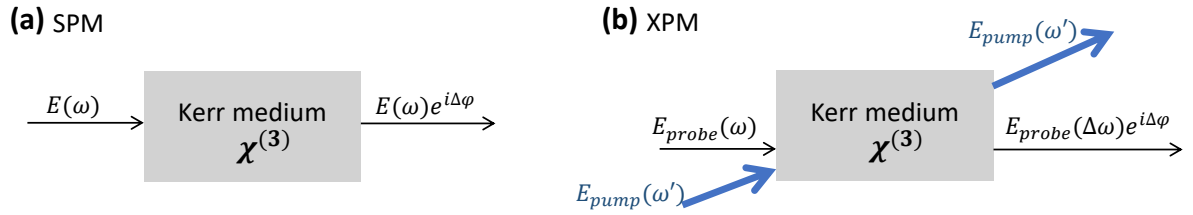


Figure 2.8: Comparison of the two interactions produced by the Kerr effect: (a) SPM and (b) XPM.

## 2.3 Ultrafast spectroscopy

**Spectroscopy** is the broad range of techniques used to determine the quantized energy levels of matter by externally triggering the transitions between these energetic levels, typically by means of optical pumping. In this manner, when the incident photon energies coincide with the energy difference between the energetic levels of the system, the incident photons can be absorbed, engendering the absorption bands of the system.

The first publication describing the concept of *spectrum* of light was submitted to the Royal Society by Newton in 1672 [66], in which the use of a prism was reported to spread (or disperse) the natural sunlight into a rainbow of colours [67]. It was not until 1815 that Fraunhofer improved the design of a spectrometer by using a diffraction grating instead of a prism [68]. Additionally, he observed different sets of dark lines in the spectral analysis of the light emitted by various astronomical objects, and wisely concluded that the placement of these lines must depend on the nature of the light source [69]; this pioneering work is considered the starting point of stellar spectroscopy. Since then, and alongside the development of the fundamental understanding of absorption spectra through quantum mechanics, spectroscopic techniques have greatly developed to become the primary tool for elucidating the electronic and molecular structures, energy spacing, and bond strengths of complex molecular systems and semiconductors [8].

**Ultrafast spectroscopy** encases the collection of spectroscopic techniques involving ultrafast laser sources, that emit pulses of laser light with a duration that ranges from few femtoseconds to nanoseconds. Employing pulsed lasers to trigger the excitations of the system under study allows to acquire an extra dimension of information compared to steady state spectroscopic techniques: the **time resolution** [70]. Through the analysis of the additional time variable, the temporal decays of the photoexcited transitions are

identified to ultimately reveal the excited state dynamics and relaxation pathways of the system. With this investigation, the absorption bands of the system (that are typically characterized with steady state spectroscopy) can be assigned to the specific transition from which they are originated.

There are many techniques that fall into the category of ultrafast spectroscopy, and often more than one of them are needed to completely characterize the system under study and build a model for the relaxation path of its phototriggered processes. Nevertheless, this section concentrates on describing the time-resolved technique employed in all upcoming chapters of this thesis, either as a powerful tool on its own for characterizing exciton dynamics (chapter 3) or as the basis from which a more advanced technique is developed (chapter 4).

### **2.3.1 Transient absorption spectroscopy (TAS)**

Broadband transient absorption spectroscopy (TAS) is a well-developed method for time-resolved spectroscopy that uses a pulsed laser source to investigate the excited state absorption (ESA) of a sample. With the so-called pump-probe technique, the dynamics of photoactivated processes are investigated by pumping the system to an electronically excited state and monitoring the photo-induced absorption changes with a broadband probe pulse. As sketched in figure 2.9(a), the light emitted by ultrafast laser source is divided into two beams: a powerful pump beam and much weaker probe beam. Pump pulses are quasi-monochromatic, with a wavelength resonant with the electronic transition of the photosystem under study, and enough intensity to excite a relatively small fraction (0,1% to tens of percent [71]) of the absorbers. Conversely, the probe beam is modulated into broadband pulses, allowing to probe the photoactivated dynamics of the system, typically in the entire visible range of wavelengths.

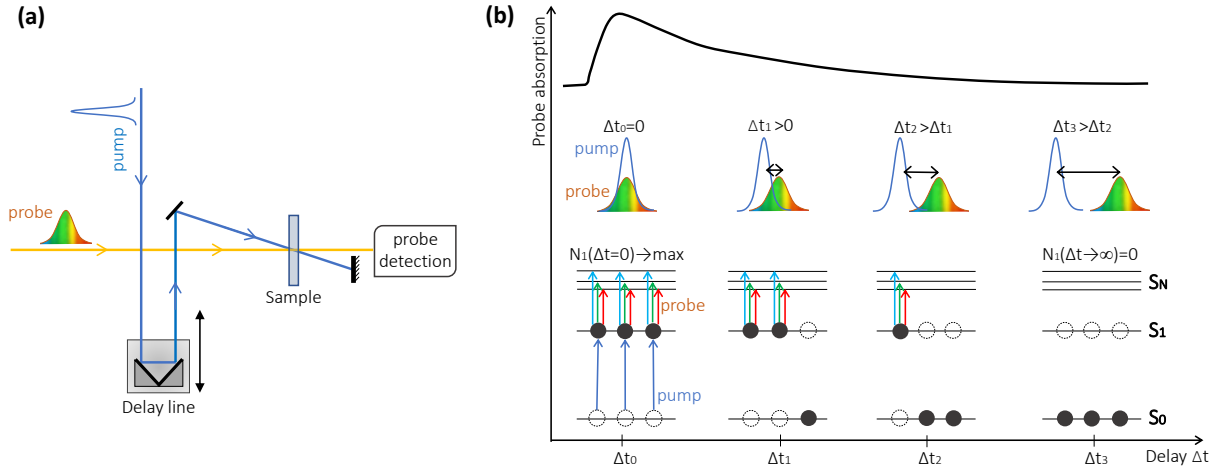


Figure 2.9: Working principle of TAS. a) Simplified TAS setup. b) Sample dynamics of ground state bleach.

### Nonlinearities in TAS

The mechanisms of TAS involve a third order nonlinear interaction of the pulses with the material, where the photogenerated dipoles are driven coherently by the external pump and probe fields, and radiate constructively in the same direction of excitation. Precisely, the investigated sample interacts twice with the electric field of the pump  $E_{pu}$ , and only once with the electric field of the probe  $E_{pr}$ , from which one photon is absorbed at the sample. The macroscopic magnitude that quantifies the collective dipole moment per unit volume is the nonlinear polarization  $P^{(3)}(\omega_{sig})$ , where  $\omega_{sig}$  is the frequency of the measured transient absorption (TA) signal. In TAS, the sample response to this third-order interaction modelled by the susceptibility tensor  $\chi^{(3)}$ , can be described as in equation (2.41), that derives from the general representation of a nonlinear polarization as specified in equation (2.28) in section 2.2.

$$P^{(3)}(\omega_{sig}) = \epsilon_0 \sum_i \chi_i^{(3)}(\omega_{sig}; \omega_{pu}, -\omega_{pu}, \omega_{pr}) |E_{pu}|^2(\omega_{pu}) E_{pr}(\omega_{pr}) \quad (2.41)$$

Where  $\omega_{pu}$  and  $\omega_{pr}$  are the frequencies of the pump and the probe beam respectively and  $\epsilon_0$  is the dielectric permittivity constant.

Under the rule of momentum conservation, equation (2.42) depicts the phase matching conditions of the TA signal with wavevector  $\vec{k}_{sig}$ . This establishes how the sample has to interact twice with the pump field, but the vectorial momentum contributions with wavevector  $\vec{k}_{pu}$  from the double pump interaction must have opposite directions. As a result, the TA signal is radiated in the same direction as the transmitted probe pulses with wavevector  $\vec{k}_{pr}$ .

$$\vec{k}_{sig} = \vec{k}_{pr} + \vec{k}_{pu} - \vec{k}_{pu} \quad (2.42)$$

### Coherent artifacts: the signature of a nonlinear response

In addition to the aforementioned nonlinear response that originates the transient signal, the system under study undergoes a further assortment of nonlinear responses that are present only for short pump-probe delays, when both pulses are present in the material. This additional signal constitutes the so-called coherent artifact.

As demonstrated in section 2.2 and equation (2.40), the existence of a nonlinear response in an isotropic material depends quadratically on the intensity of the incident electromagnetic field; for this reason, any time-resolved measurements that involve the use of pulses that temporally and spatially overlap in a material, entails the creation the coherent artifact: It results from the immensely high pulse energy that concentrates in matter for a very short time, and produces a transitory nonlinear effect that concludes in a time span of the same order of magnitude<sup>13</sup> than the duration of the exciting pulses.

---

<sup>13</sup>the precise duration of the coherent artifact depends on the specific nonlinear effect from which it originates.

The adjective "coherent" attached to the definition of the artifact conveys that the interfering pulses generating the coherent artifact have a high degree of spatial coherence [72] and therefore, are in constant relative phase when they interact at the sample.

**Use.** The coherent artifact is often considered a perturbation when characterizing the short-lived excited state dynamics of a sample, as it overlaps with its characteristic transient signal in the first few tens of femtoseconds and it is quite cumbersome to isolate and correct [73]. However, the identification of the coherent artifact has, in fact, many uses within the framework of TAS, such as:

1. **Chirp correction of the data.** TA measurements that utilize a broadband probe (as the one described at the end of this chapter) engender a set of data in a wide range of wavelengths; however, its generation through the white-light supercontinuum effect provides the resulting probe pulses with a notable chirp. This implies that every wavelength component within the probe pulse temporally overlaps with the pump pulses at a different delay time, which needs to be corrected in the post-processing of the TAS data. This correction is often made by fitting the strong and short-lived signal of the coherent artifact, and subsequently flattening the curved profile of the measured TA signal versus wavelength.
2. **Characterization of new measuring setup.** The origins of a coherent artifact are extensively reported [56, 73–78], which allows to simulate its signal profile once the participating nonlinear effects are identified.
3. **Instrumental response function (IRF).** When the measured coherent artifact stems only from a TPA nonlinearity, it can be used to determine the instrument response function [79]. As detailed in the next section, this cross-correlated signal



also encapsulates the duration of the pump and probe pulses, similarly to the auto-correlation technique used to determine the pulse duration of an ultrafast laser source [80].

### Time resolution

The temporal resolution of a pump-probe setup is achieved by introducing a temporal delay between pump and probe pulses, typically by tuning the optical path of either pump or probe with an optical delay line. In this manner, a fast photodetector is not needed, and the time resolution is limited by the pulse duration of the laser source, as will be explained in the next paragraph. However, one must not forget that the temporal sampling rate corresponds to the smallest possible translational step of the delay line, which typically falls in the range of few tens of attoseconds.

Generally, the time resolution of an instrument is defined by the instrument response function (IRF) and corresponds to the convolution of the temporal response of the detection system and the shape of the laser pulse arriving to the detector [81]. In the particular case of TAS, the IRF is defined by the cross correlation of pump and probe pulses, and it is also observable as TA signal, but only at the close vicinity of zero pump-probe delay. Although its detection is useful for determining the IRF, it is often referred to as an "artifact" (precisely *coherent* artifact, as introduced in the previous section), as it restricts the identification of short-lived processes right after excitation by dominating the dynamics of the investigated system.

It is also relevant to notice here that there is a fundamental limitation on how short the pulses *can be*. The idea is to excite a single electronic transition and for that, a fairly monochromatic pump (i.e., with narrow spectral bandwidth) is needed. Therefore, one

has to keep in mind time-bandwidth limit from equation (2.22). This time-bandwidth relationship implies that shortening the pump pulse duration  $T_p$  would intrinsically translate to an increase of the pump spectral width  $\Delta\omega_p$  which, if taken too far, could lead to multiple excitations of different electronic transitions of the photosystem under study. This scenario is avoided in the present case, since it would greatly interfere with the analysis of retrieved data.

With these considerations, it is essential to select a laser source and length of delay line according to the time scales of the photoactivated dynamics of interest. Precisely, the IRF at sample position must be shorter than the fastest relaxation process that one wants to resolve in the system under study. In turn, the length of the delay line should ideally correspond to at least the mean lifetime of the slowest transition to evaluate. In the present case and generally in photophysics, pulse durations of few to several tens of femtoseconds are considered ideal, since they allow the resolution of the dynamics of transitions activated by light absorption. An example of a relevant processes involved in semiconductor materials and photocatalytic systems is charge transfer, that can occur among different moieties or functional groups within a same molecule [82, 83], between the  $P$  and  $N$  layers of a semiconductor junction [84–86] and in general, between donor and acceptor sites of a photoactive system.

### Data collection and interpretation

The measured magnitude in TAS is the probe intensity transmitted through the sample  $I(\lambda)$ , which is wavelength dependent and related to the sample absorbance  $A(\lambda)$  and the incident probe intensity  $I_0(\lambda)$  by equation (2.43).

$$A = -\log \frac{I}{I_0} \tag{2.43}$$

Nevertheless, the variable to retrieve in TAS is precisely the transient absorbance  $\Delta A(\lambda, t_d)$ , which is a multivariate function that records the change in sample absorbance as a function of the probe wavelength  $\lambda$  and delay time  $t_d$  between pump and probe pulses.  $\Delta A(\lambda, t_d)$  is a differential quantity, obtained by subtracting the pumped sample absorbance  $A_p(\lambda, t_d)$  by the non-pumped sample absorbance  $A_{np}(\lambda, t_d)$  as described by equation (2.44).

$$\begin{aligned}\Delta A(\lambda, t_d) &= A_p(\lambda, t_d) - A_{np}(\lambda, t_d) = -\log \frac{I_p(\lambda, t_d)}{I_0(\lambda)} + \log \frac{I_{np}(\lambda)}{I_0(\lambda)} \\ &= \log \frac{I_{np}(\lambda)}{I_p(\lambda, t_d)}\end{aligned}\tag{2.44}$$

The nature of this differential signal requires an experimental setting that allows the consecutive detection of the transmitted probe intensities of the pumped  $I_p(\lambda, t_d)$  and non-pumped  $I_{np}(\lambda)$  sample. For this purpose, a mechanical chopper is added to the pump beam path, and is set to block every second pulse by tuning its frequency to half the repetition rate of the laser; in our system sketched in figure 2.11, the chopper runs at 500 Hz and laser source has a repetition rate of 1 kHz.

### **What information is encoded in $\Delta A(\lambda, t_d)$ ?**

The sign of  $\Delta A(\lambda, t_d)$  depends on which physical processes dominate the TA signal of the system under study; according their relative phase, pump and probe beams interfere either constructively, originating ground state bleach or stimulated emission, or destructively, giving rise to excited state absorption [87].

Negative contributions to  $\Delta A(\lambda, t_d)$ : A ground state bleach (GSB) signal is generated by the depopulation of the systems' ground state upon absorption of the pump pulse. Due to the decrease in carriers at the ground state, the transmission of the probe increases

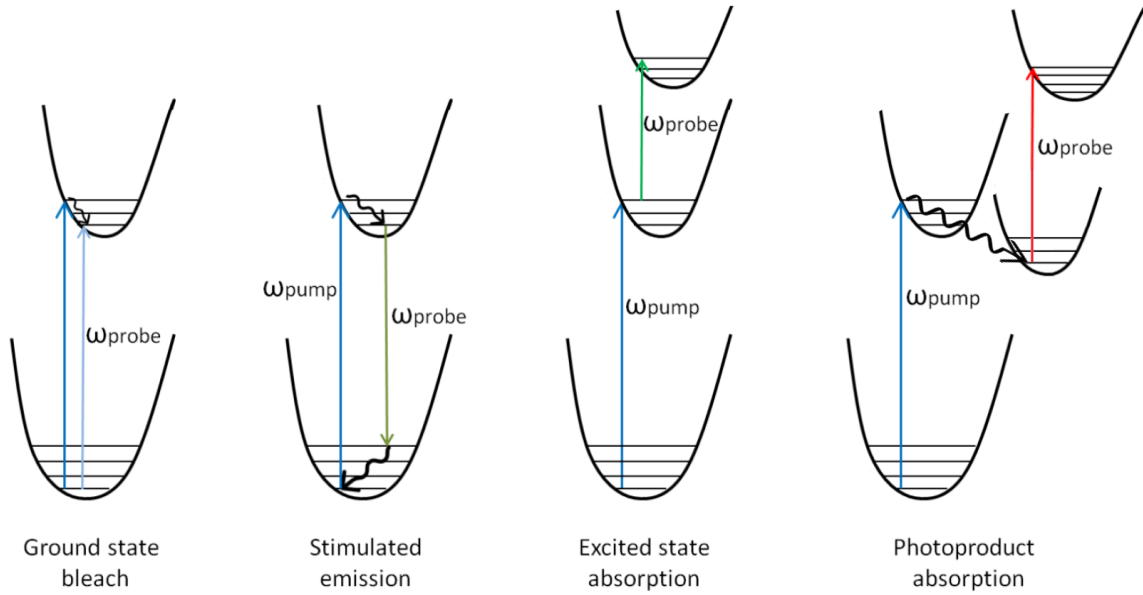


Figure 2.10: Diagrams of the different possible contributions to the overall TA signal.

and thus the contribution to the overall  $\Delta A(\lambda, t_d)$  is negative. Stimulated emission (SE) originates at those wavelengths where the probe pulses are in resonance with a fluorescence emission. This induces an increase of probe photons and appears also as a negative  $\Delta A(\lambda, t_d)$ , but its spectra differs from the GSB thanks to the naturally occurring Stokes-shift of fluorescence. Therefore, SE spectra is red-shifted with respect to GSB, but in most cases partially overlapping with it.

Positive contributions to  $\Delta A(\lambda, t_d)$ : ESA happens in those spectral regions where the probe pulses are absorbed by carriers located at the excited state, prompting their transition to a further excited state. Another positive contribution to  $\Delta A(\lambda, t_d)$  happens upon photoproduct absorption. In this case, the absorption of pump pulses provokes the formation of new species in the system under study, for example an oxidated or reduced version of the original compound. The appearance of new species comes with

new allowed transitions at the system, opening up new spectral regions where probe pulses can be absorbed. In both instances, the probe absorption is enhanced in a specific spectral region, where the transmitted probe intensity decreases, and therefore results in a positive contribution to the  $\Delta A(\lambda, t_d)$  signal.

### Data modelling of TAS

In an over-simplistic photosystem like the one depicted in figure 2.9(b), there is only one possible pathway for the relaxation of the photopumped population inversion: a simple monoexponential decay can be fitted to the decay curve, and the lifetime of the one and only excited state can be retrieved. In such scenario,  $\Delta A(\lambda, t_d)$  can be fitted by single term ( $i = 1$ ) of the summation in equation (2.45), where  $C_i(\lambda)$  are the pre-exponential factors (also referred to as decay associated spectra) and  $s_i$  the lifetimes associated with the different photoexcited transitions [88].

$$\Delta A(\lambda, t_d) = \sum_i C_i(\lambda) \cdot \exp(-t_d/s_i) \quad (2.45)$$

Unfortunately, the reality of an intricate photosystem is quite far from the depicted simplification, and there are multiple possible relaxation mechanisms that may compete all at once, or take over the dynamics of the photoexcited states at different timescales. This translates into a complex multiexponential decay described in equation (2.45), this time with ( $i = 1$ ). For this reason, a consistent methodology for the analysis of TA signals is required, that is able to test different hypothesis according to prior assumptions of the phototriggered electronic transitions of the sample under study. Global lifetime analysis (GLA) is, by far, the most commonly used strategy for the simultaneous analysis at different wavelengths of multiple kinetic profiles [81]. In this manner, the raw TA signal is filtered, chirp corrected and fitted though an iterative algorithm that ultimately

expresses  $\Delta A(\lambda, t_d)$  as a superposition of multiple first-order exponential functions.

In order to identify the reaction steps of the system under study, different fitting models for relaxation dynamics have been tested. The parallel kinetic model assumes that each photoexcited state follows its own relaxation pathway, independent from the other decaying processes. In the present work, a modelling of  $\Delta A(\lambda, t_d)$  through parallel kinetics was found adequate to fit the evolution of the excited states of the system. By iteratively optimizing the parameters  $i$  and  $s_i$  in equation (2.45), one will eventually encounter the best fit that allows to accurately model the experimental data with minimum deviation.

### Experimental setup for TAS

Figure 2.11 shows the experimental setup for TAS; the names of the elements in the figure are referenced in the text as (TYPEWRITER CAPS). A combination of a titanium-sapphire oscillator and chirped pulsed amplifier ((TI:SA + CPA), Coherent Legend) emits pulses of 50 fs duration at 800 nm, with a pulse energy of 1 mJ and repetition rate of 1 kHz. By means of a 90:10 beam splitter (BS1), the beam is divided into pump pulses with 90% of the incident intensity and probe pulses with the residual 10%.

On one side, pump pulses are frequency tuned, either by means of an optical parametric amplifier ((OPA), Topas C Light Conversion) or by second harmonic generation at a beta barium borate (BBO) crystal (BBO), which frequency doubles the fundamental 800 nm into 400 nm pulses. The repetition rate of the pump is halved by means of a chopper ((C), Terahertz Technologies Inc. D-995) at 500 Hz, and sent into a delay line (DL) composed of a retroreflective mirror (Thorlabs HRR203-P01) and a translational stage (Thorlabs DDS300/M) with 30 cm ( $\simeq 2$  ns) length and a minimum incremental movement of 100 nm ( $\simeq 0.3$  fs). A combination of a Berek compensator ((B), Newport) and a linear Glan

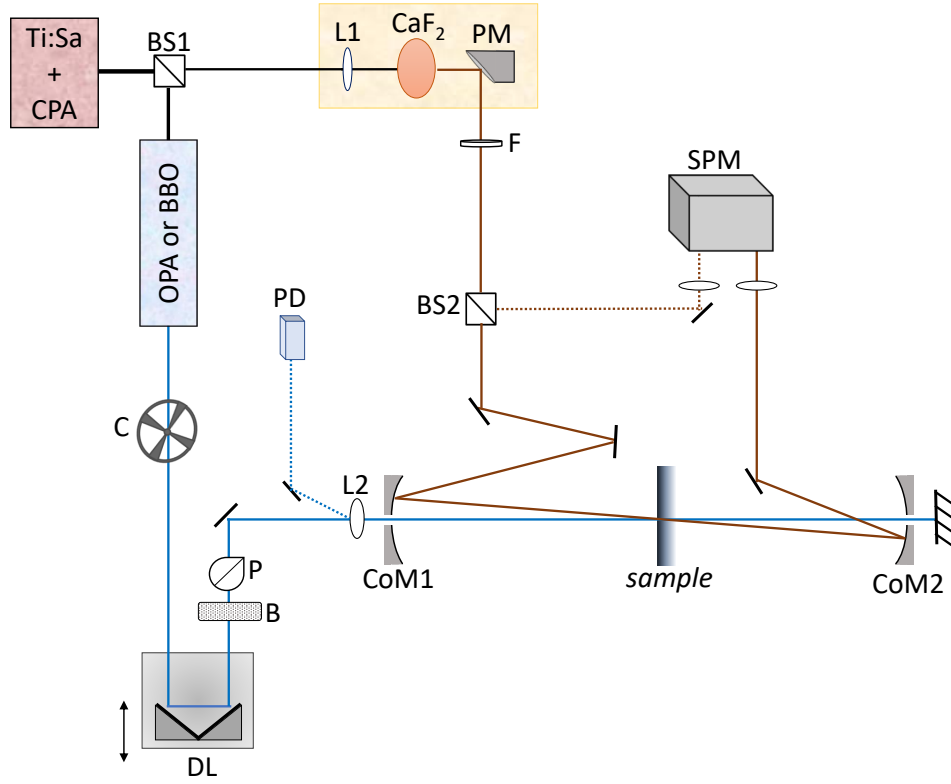


Figure 2.11: Sketch of the TAS setup

polarizer ((P), Thorlabs GL15) is used to set the pump polarization to linear, and at a  $54.7^\circ$  angle with respect of the polarization of the probe. This corresponds to the so-called magic angle, and avoids the additional signal contributions arising from molecular rotations [89]. Thereafter, the pump pulses are focused by means of a lens (L2) with a focal length of 500 mm and sent towards the sample position, located close to (but not exactly at) the focal point of (L2). Notice that the pump beam passes through holes drilled at the center of two 2"  $\varnothing$  concave mirrors ((CoM1) and (CoM2)) and it is dumped after the second one. Alternatively, a reflection from (L2) of the pump beam is detected with a photodiode (PD) and sent to the measuring software, to differentiate and classify pumped and non-pumped shots.

On the other side, probe pulses are focused with a 100 mm lens (L1) into a calcium fluoride plate of 1 mm thickness ( $\text{CaF}_2$ ), which spectrally broadens the 800 nm towards the visible wavelength range via white light supercontinuum generation, process in which the polarization of the pump is conserved. To prevent burning the  $\text{CaF}_2$  within few minutes, the plate is constantly kept in translational periodic motion with a custom-made motorized ensemble. In order to avoid chromatic aberration, the broadband probe is collimated with a parabolic mirror (PM). Subsequently, a spectral filter (F) is used to remove the residual 800 nm, and a 50:50 beamsplitter (BS2) divides the probe into two beams: One of them serves as a reference, and therefore it is directly focused into a double-beam monochromator/spectrograph ((SPM), Teledyne Princeton Instruments Acton SP2150). The second portion of the probe beam is sent towards the first concave mirror (CoM1), that directs it towards the sample, where it is spatially overlapped with the pump beam in a quasi-collinear regime. Subsequently, they are collimated by the second concave mirror (CoM2) and lastly recorded with the same spectrograph (SPM) as the reference portion of the probe beam.



# Chapter 3

## Spectroscopic analysis of van der Waals heterojunctions

### 3.1 Introduction

The research dedicated to the fabrication of semiconductor heterostructures, where two different types of semiconducting materials are combined, has opened up unique opportunities for the development of modern optoelectronics [6, 90]. The current research in heterostructured systems is mostly focused on exploring their promising performance in light harvesting devices, such as photodetectors, phototransistors, solar cells and photocatalysts for hydrogen fuel production [7, 86, 91].

In the past decade, there has been special interest in developing hybrid van der Waals (vdW) heterojunctions made of a combination of organic and inorganic layers [92–94]. The interfacing of two functional units with distinctive properties aims to combine the

benefits of both worlds, potentially enabling the development of ideal interfaces with advanced functionalities [95].

This chapter is dedicated to characterize the spectroscopic properties and the ESA of an exemplary vdW heterostructure proposed by our collaboration partners<sup>1</sup>, consisting of a combination of an organic semiconductor nanosheet and a monolayer of a transition metal dichalcogenide (TMD). With this analysis, one expects to unravel the response of such multilayered semiconductors upon illumination, precisely, which are the phototriggered electronic transitions, the photogenerated energy transfers and the photoproducts of light absorption.

In this first introductory section, the theory of semiconductor physics is briefly explained, as it will become indispensable to understand the dynamics of the charge carriers and their possible signatures in TAS data. Consecutively, the investigated heterostructure is presented, together with the detailed description of its individual layers and their reported photoabsorption. Afterwards, the experimental methodology is described, alongside the employed samples and spectroscopic techniques. Finally, the empirical data is presented and discussed, followed by the analysis of the functionality of the heterostructured system and its applicability to an operational optoelectronic devices.

### 3.1.1 Semiconductor physics

The semiconducting behaviour of some materials was first discovered in the 1820's while experimenting with their electrical properties [96], but it was not until 1874 that Karl Ferdinand Braun developed, purely by experimental trial, the first semiconductor device: the so-called *Cat's whisker detector* (or *crystal detector*). This apparatus became a

---

<sup>1</sup>They will be properly introduced in subsection 3.2.2, when discussing sample fabrication.

fundamental piece of radio receivers, as it was capable of demodulating the audio signal from the radio frequency carrier wave [97].

Although this device is nowadays obsolete, it gave an extra push towards the fundamental investigation of semiconductors, as their underlying physics could still not be understood under the laws of classical physics. It was not until 1920 with the foundation of quantum mechanics that the groundwork of semiconductor physics could be established [98]. Since then, the amount of research dedicated to designing new semiconductor devices has never stopped growing, and the machinery derived from these studies became an indispensable part of modern technology and our everyday life. Still nowadays, the research area of semiconducting devices has remained an infinite fountain of new discoveries and has expanded along with the ever-improving capacities in nanoengineering and thin film technology [99, 100].

The conductivity of a material depends on the amount of free electrons in the system; the exceptional characteristic that makes semiconducting materials special is their mutability: depending on the temperature, the conditions of light illumination and the applied potential they can either become conductive or behave like insulators.

### **Band theory**

The physical origin behind the unique performance of semiconductors is elucidated through band theory. Similarly to energy levels in molecular systems, the allowed energies for electrons in a semiconductor are calculated through their quantum mechanical wave functions, typically defined by the Schroedinger equation [98]. Distinctively, the atoms in semiconductor materials are closely located in a periodic lattice, which puts the discreet individual orbitals closely spaced. As a result, the orbitals merge into continuous energy

levels called **bands**, in a process known as hybridization of electron orbitals [101].

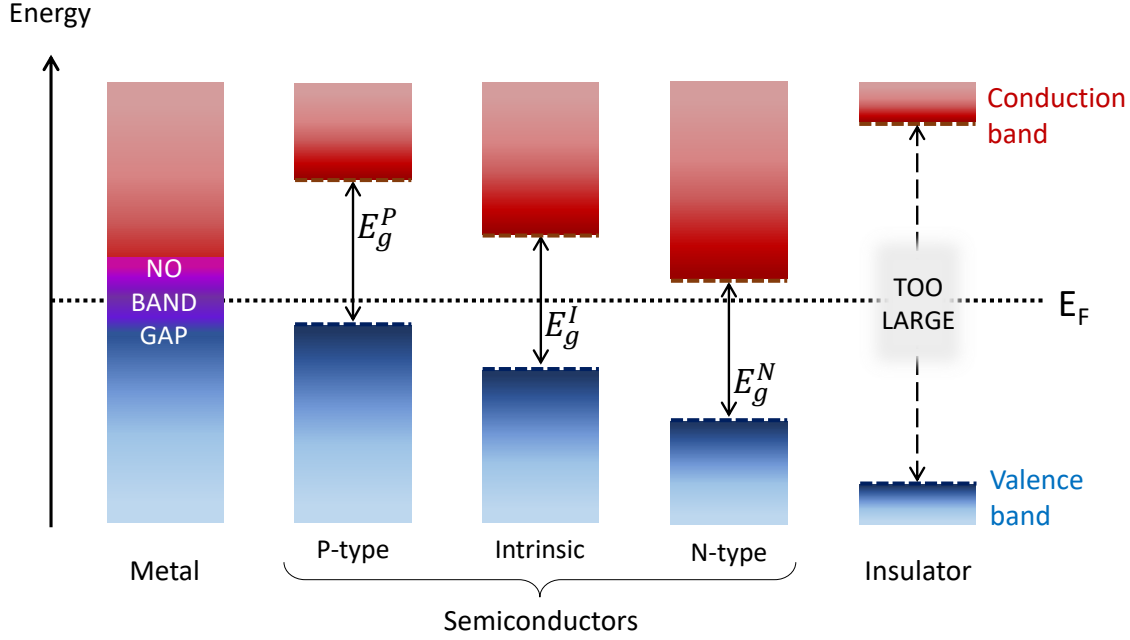


Figure 3.1: Sketch of the band structure and conductivity-related parameters of different kinds of solids. Under the umbrella of semiconductors, there are three main categories with band gaps  $E_g^P$ ,  $E_g^I$ ,  $E_g^N$  that will be described in detail in the next section.

Figure 3.1 shows a representation of the distinct band structures of different kinds of solids. In this framework, we refer to the Fermi energy level  $E_F$  as the maximum energy within the collection of electron energy levels at absolute zero temperature (0K). The lower energy orbitals form a band called the **valence band (VB)**, denoting the highest energy level that is completely filled, at zero Kelvin (0K). Alternatively, the **conduction band (CB)** corresponds to the lowest partially-filled energy level at 0K. The distance between the VB and the CB is called **band gap**  $E_g$ , defined as the minimum amount of energy required for the electron to transition between the VB and the CB, at 0K. In other words, it determines the minimum energy that an incident photon needs to

have in order to be absorbed by the semiconductor, consequently triggering an electronic transition from the VB to the CB. As shown in figure 3.1, the band gap is one of the most distinctive properties of a material, since it determines its behaviour regarding electrical conductivity. Particularly for semiconductors, the band gap energy usually lies in the visible, near infrared or near UV, whereas for an insulator the band gap is so large that it cannot be accessed via photonic excitations. Contrarily, in the case of metals there is an overlap of the CB and VB, which increases the amount of free electrons in the CB and makes the material conductor.

### Types of semiconductors and doping

Semiconductors are not amorphous solids; instead, their atoms are located in a periodic manner according to a crystal lattice. The semiconducting properties can be greatly tuned by the controlled addition of impurities into the crystal structure, process known as **doping**. The insertion of specific atoms with a different number of valence electrons into the lattice will modify the amount of free electrons at the semiconductor.

For the purpose of explaining the effect of doping, let us focus on the example of silicon (Si), the most commonly used semiconductor due to its abundance in earth. In its pure form, it is categorized as an intrinsic semiconductor with a band gap  $E_g^I = 1.17$  eV and the Fermi level located at the middle of it, as depicted in figure 3.1 for intrinsic semiconductors. The Si atom has four valence electrons at its outermost shell that form covalent bonds with the valence electrons of its neighbouring Si atoms, crystalizing into a diamond cubic lattice where each atom is surrounded by eight electrons. This robust lattice structure leaves virtually zero free charge carriers, which translates into a low conductivity [27].

Replacing very few of the Si lattice atoms with a valence-five element such as phosphorus

(P) will cause to have an extra electron additional to the four covalent bonds that are established with the nearest neighbours. This extra electron is a free electron added to the semiconductor, which changes it into a **N-type** semiconductor, since it is electron-rich and therefore negatively charged. Instead, if the doping atom is a valence-three element like boron (B), there will be a missing electron in the crystalline structure which, in the frame of semiconductor physics is referred to as a hole, i.e., a positively charged vacancy in the lattice. This electron-lacking or hole-rich material is called a **P-type** semiconductor, for being positively charged.

As the consequence of doping is the insertion of free charge carriers into the system, it has the capacity of tuning the conductivity of the semiconductor. For example, adding only 1 B atom for every  $10^5$  Si atoms increases the conductivity of pure silicon by a factor of a thousand [27]. The band properties of all the aforementioned types of semiconductors are represented in the previous figure 3.1.

### Lattices and Brillouin zone

There are 14 different possible lattice geometries, also called Bravais lattices, each defined with a set of non-coplanar vectors [27]. With the purpose of correlating the effect of the spatial lattice structure with the optoelectronic properties of the material, we want to work in the reciprocal lattice space, which is mathematically calculated as the Fourier transform of the Bravais lattice. As the the Fourier transform of space is momentum, the spatial lattice vectors in the Bravais lattice are transformed into wavevectors  $\mathbf{k}$ , that belong to the momentum space. This change of domain gives a more realistic picture of the crystal structure (and not the points where the atoms are located), and also allows to define the Brillouin zones and band diagrams of semiconductors.

**The Brillouin zone** is a mathematical construction that displays the lattice base (or unit cell) in the momentum space. As depicted in figure 3.2, the Brillouin zones are defined by drawing lines between any points in the reciprocal lattice, and thus dividing it into areas of equal volume. In this manner, one can define specific points of high symmetry, also called critical points, from which the Brillouin Zone can be cloned to reproduce the lattice. In general, the crucial point  $\Gamma$  defines the center of the Brillouin zone and, depending on the lattice geometry, a few other crucial points are defined, as demonstrated in figure 3.2.

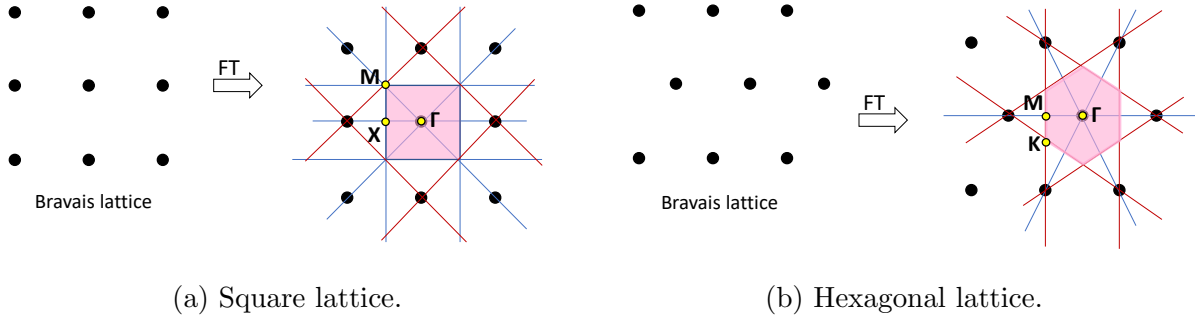


Figure 3.2: Depiction of the Bravais and reciprocal lattice, together with the Brillouin zones (pink area) and the crucial points (yellow dots) of two different types of crystal grids: (a) Square lattice, with crucial points  $\Gamma$ ,  $X$  and  $M$ ; (b) Hexagonal lattice with crucial points  $\Gamma$ ,  $K$  and  $M$ .

**Band diagrams** represent the allowed energy levels<sup>2</sup> of a semiconductor as a function of wavevector in the x-axis, usually displayed in terms of the symmetry points of the Brillouin zone, that depend on the lattice geometry. Using the example case of the diamond cubic crystal structure of silicon the band diagram takes the form represented in figure 3.3, with its typical crucial points  $\Gamma$ ,  $K$  and  $M$  [102].

<sup>2</sup>Retrieved from the solutions of the Schroedinger equation using Block states as the wavefunctions of electrons in semiconductors [27].

All the relevant optoelectronic properties of a semiconducting material are represented in the band diagram. To start, one wants to pay attention to the band gap and the positions of the CB and VB in relation to the Fermi level, that are sketched in figure 3.1. Equally important are the positions of the CB and VB peaks (minimum and maximum, respectively) with respect to the x-axis; if the CB minimum and the VB maximum appear at the same wavenumber the semiconductor is **direct**; if there is a horizontal shift in the peak positions of CB and VB, the semiconductor is **indirect**. The former defines whether the electronic transition between CB and VB can happen upon photon absorption only (direct) or if it has to be a phonon assisted transition (indirect). As depicted in figure 3.3 silicon constitutes an indirect semiconductor, and therefore its band gap  $E_g$  is depicted as a skewed arrow.

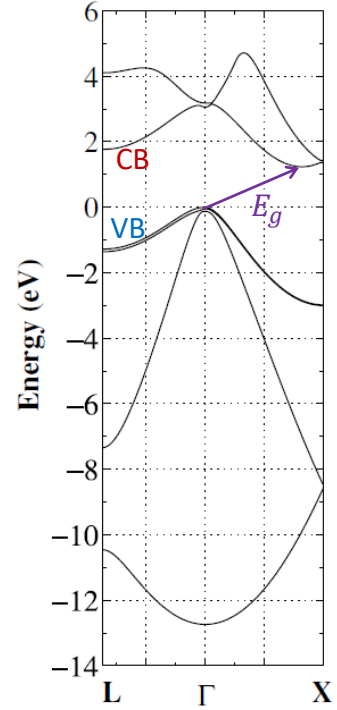


Figure 3.3: Band diagram of silicon. Image adapted from [102].

The distinction between direct and indirect semiconductor is of special interest for optoelectronic devices since direct band gap materials provide more efficient absorption and emission of light. On top of that, band diagrams are useful in comparing the band structures of different materials that are to be placed in physical contact, as explained in the following section.



### Semiconductor junctions

With the purpose of fabricating semiconductor devices, various types of semiconductors are combined in a same appliance. The most common class of composites are the so-called **PN junctions**, in which a P-type and an N-type semiconductor are placed in direct contact, as depicted in figure 3.4. These PN junctions constitute the fundamental building blocks of modern electronic devices from which diodes, LEDs, transistors and solar cells are built, among many others [100]. Their main property is that they allow the electrical current to be transferred in one direction only, since the electrons can easily flow from the N-type to the P-type semiconductor, but not in the opposite direction. To understand this phenomena better, let us explore the charge carrier transport across the junction in three different environments, as represented in figures 3.4 and 3.5.

**Zero bias** When an N-type and a P-type semiconductor (from now on, P and N) are placed in contact, there is a prompt charge carrier reorganisation at the interface of both materials. The holes at P are electrostatically attracted towards the junction; the same happens to the electrons at N. By thermal migration, charge carriers are transferred across the junction, i.e., electrons diffuse from N to P, as depicted in figure 3.4(a)<sup>3</sup>.

Upon crossing the junction, the charge carriers recombine with their opposite charge carrier. This process depletes the natural (or majority) charge carriers of each type, i.e., consuming the holes in P and the electrons in N, which forms the so-called **depletion region** near the junction. In this region, N and P have lost a notable amount of their majority charge carriers, which causes the energy bands to bend: in N, the CB and VB increase in energy (bending upwards) and in P, the opposite happens.

---

<sup>3</sup>Note: The junction represented in figures 3.4 to 3.6 is an example case where both P and N have the same band gap and band edges (homojunction). Although this does not represent the most general picture (where band gaps and edges can be different) it fulfils the purpose of the simplified sketch to aid in the explanations of band bending and charge accumulation in a PN junction.

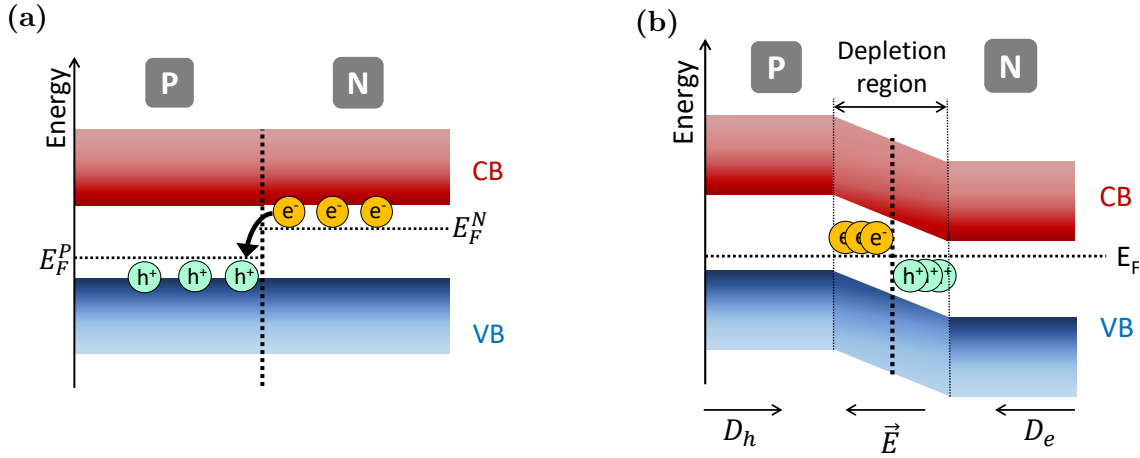


Figure 3.4: Unbiased PN junction and charge carrier behaviour: (a) before and (b) after equilibrium is reached. For simplicity, only the majority carriers in each type are depicted.

The condition of equilibrium, represented in figure 3.4(b), is reached when the charge carrier diffusion has ended. The process of charge recombination and depletion leaves a positively charged layer at the boundary of N and, inversely, a negatively charged layer at the boundary of P. This creates a built-in potential  $V_{Bi}$  and an electric field  $\vec{E}$  that opposes the diffusion forces ( $D_h$  for holes and  $D_e$  for electrons), which dynamically counteracts the process of charge diffusion and maintains the equilibrium. The charge density at each side is equivalent to the net doping level of each semiconductor type, and therefore can be flexibly adjusted for best device performance.

**Forward bias** Figure 3.5(a) depicts what happens when a PN junction is connected to a forward bias, i.e., the negative terminal of a battery is connected to N, and the positive to P. The externally applied electrical field effectively pushes the majority carriers of each side towards the junction: the positive terminal repels the holes that remain at the neutral region of P, and the negative terminal repels the electrons at the neutral region of N. When the battery potential is higher than  $V_{Bi}$ , the diffusion process of charge carriers is restarted, and therefore there is, again, an electrical current flow through the junction.

This causes the shrinkage of the depletion region and the decrease of band bending at the junction.

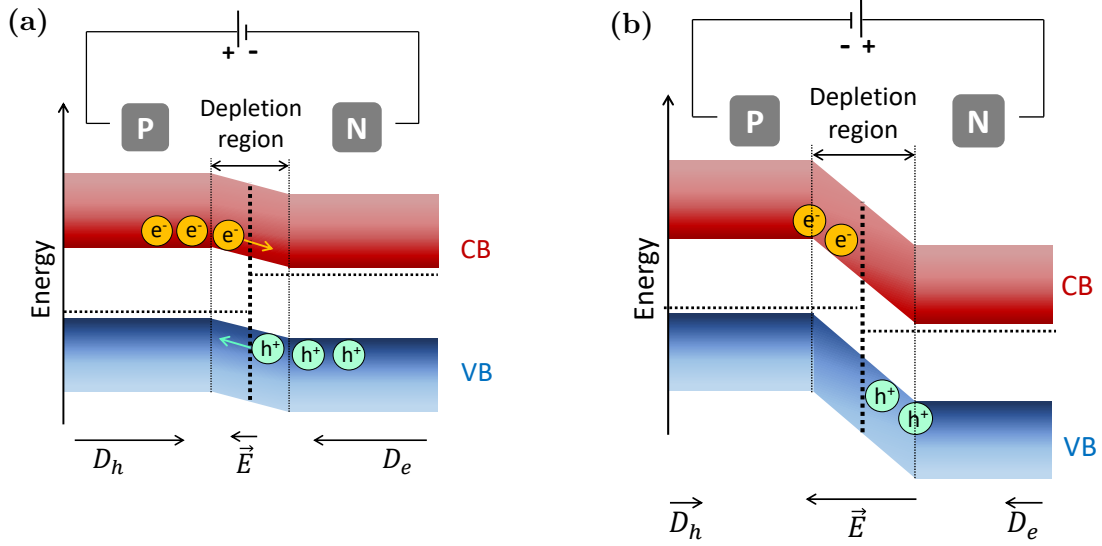


Figure 3.5: Depiction of the behaviour of a PN junction and their charge carriers, depending on the applied potential. (a) Forwards bias. (b) Reverse bias.

**Reverse bias** In the case of reverse bias, where the battery polarity is inverted as shown in figure 3.5(b), the charge carriers are pulled away from the junction, increasing the size of the depletion region and with that, the potential that counteracts the diffusion force. Since the voltage barrier is tremendously increased, only a minimal electric current can flow across the junction, resulting in a insulator-like behaviour. This effect is also evidenced by the pronounced bending of the energy bands.

**Light-sensitive PN junctions** As mentioned previously, when a semiconductor is illuminated with a light source whose photons have equal or higher energy than its band gap, those photons will be absorbed at the semiconductor by triggering the excitation of a electron from the VB to the CB. This transition leaves a hole in the VB, creating an **exciton**, i.e., a quasiparticle constituted of an electron (in CB) and a hole (in VB), bound electrostatically by the Coulomb force.

When a PN junction is made of a P semiconductor with a band gap  $E_g$  lower than the incident photon energy  $h\nu$ , the photogenerated exciton can create a light-generated current  $I_L$ , by connecting it to an -unbiased- external circuit, as depicted in figure 3.6. For this to happen efficiently, the photon has to reach the depletion region of the PN junction. In this manner, the electron is drifted by the built-in  $\vec{E}$  towards N before it recombines with its bound hole, process in which the exciton is dissociated.

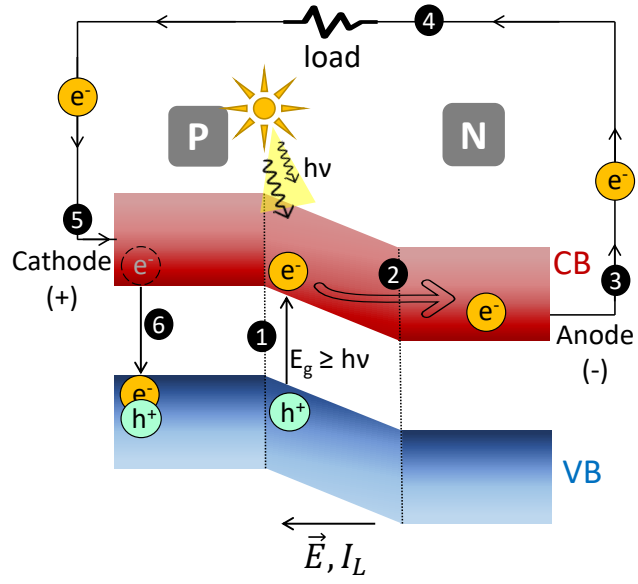


Figure 3.6: Photogenerated excitons in illuminated PN junctions. The numbers indicate the order in which the processes take place, as referenced in the text.

The electron, now at N, is collected by the anode, and travels through the external circuit, powering the battery or the device connected to it (load). As the electron comes back to P through the closed circuit, it finally recombines with the hole.

The aforementioned process, known as **photovoltaic effect**, generates a usable current upon light absorption; for this reason PN junctions have become the basic building blocs of photodetectors and solar cells.

### 3.1.2 Building a heterojunction: the system under study

The PN junction investigated in this thesis, is categorized as a vdW type II heterostructure, due to their respective staggered alignment of the conduction and valence bands of the N and P type, as depicted in figure 3.7.

The inorganic layer will constitute the N-type semiconductor at the heterostructure, having the capacity to accept electrons. Conversely, the electron-donor P layer will be made from an organic nanosheet with energy levels equivalent to those in molecular systems. The latter trait, together with the specific constituents of the investigated heterostructure, will be described in detail in the following subsections.

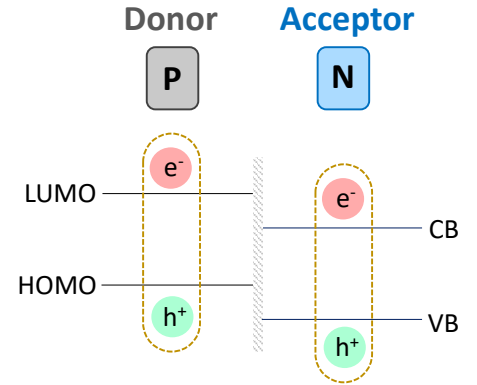


Figure 3.7: Staggered band alignment of the vdW type II heterostructure.

Other types of vdW heterostructures with straddling (type I) or broken (type III) band gap alignment are not good candidates for the fabrication of photoelectric devices, since they cannot offer the same efficiency in charge separation and carrier transfer across the junction [85]. In general, an efficient charge transfer between P and N will dictate the performance of the heterojunction, which is influenced by the band offset between N and P and the built-in electric field at the depletion region [103]. Moreover, the atomically-sharp edge of each layer at the vdW interface diminishes the amount of scatter centers and charge traps, which further promotes a rapid charge transfer and therefore improves the performance of the heterostructure [86].

### N type layer

The electron-rich (i.e., N type) layer of the PN junction under study is made of monomolecular film of Molybdenum disulfide ( $\text{MoS}_2$ ). This molecule belongs to the family of transition metal dichalcogenides (TMD) that comprises all inorganic semiconductors of type  $\text{MX}_2$ , where  $M$  is a transition metal sandwiched in between two layers of  $X$  atoms of the chalcogen family, specifically sulphur (S), selenium (Se) or tellurium (Te). The atoms are disposed forming an octahedral (1T) or a trigonal prismatic (2H) structure, as depicted in figure 3.8. Due to its specific crystalline structure, the vdW interactions between different layers of  $\text{MoS}_2$  are very weak in comparison to the strong interlayer bonding of the atoms on the two-dimensional (2D) plane. This characteristic allows to fabricate a mechanically stable single layer of  $\text{MoS}_2$  by micromechanical cleavage, exfoliation or chemical vapour deposition (CVD), among others [104–106].

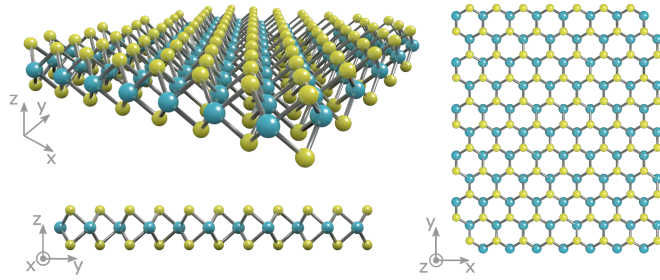


Figure 3.8: Trigonal prismatic (2H) structure of  $\text{MoS}_2$  in different perspectives. Image adapted from [107].

Monolayered  $\text{MoS}_2$  is gaining popularity among other 2D semiconductors due to its comparability to graphene in terms of electron mobility, surface stability and mechanical flexibility [92]. Additionally,  $\text{MoS}_2$  monolayers have much more favourable band structure compared to the gapless graphene, resulting in a finite and tunable band gap in the visible range [108]. Thanks to their great performance, TMD materials are well established as the inorganic side of vdW heterostructures, and therefore the current research is more

focused on finding an appropriate organic material for the donor layer that allows for the construction of suitable heterostructures for given applications [109].

**Optical properties of MoS<sub>2</sub> monolayers** The most important characteristic of TMD materials is that their electronic and optoelectronic properties in bulk are very different than those compared to monolayered TMDs. As shown in figure 3.9, TMDs present a reduced indirect band gap, induced by the lack of out-of-plane quantum confinement that arises from stacking several lattice layers. On the contrary, 2D TMDs exhibit a direct band gap with energies in the visible and near infrared range [17]. Such property allows the utilization of monolayered TMDs in 2D photonic and optoelectronic devices. Moreover, thanks to their high photoresponsivity and low dielectric screening, they become great materials for the construction of ultrafast high-sensitivity photodetectors [110].

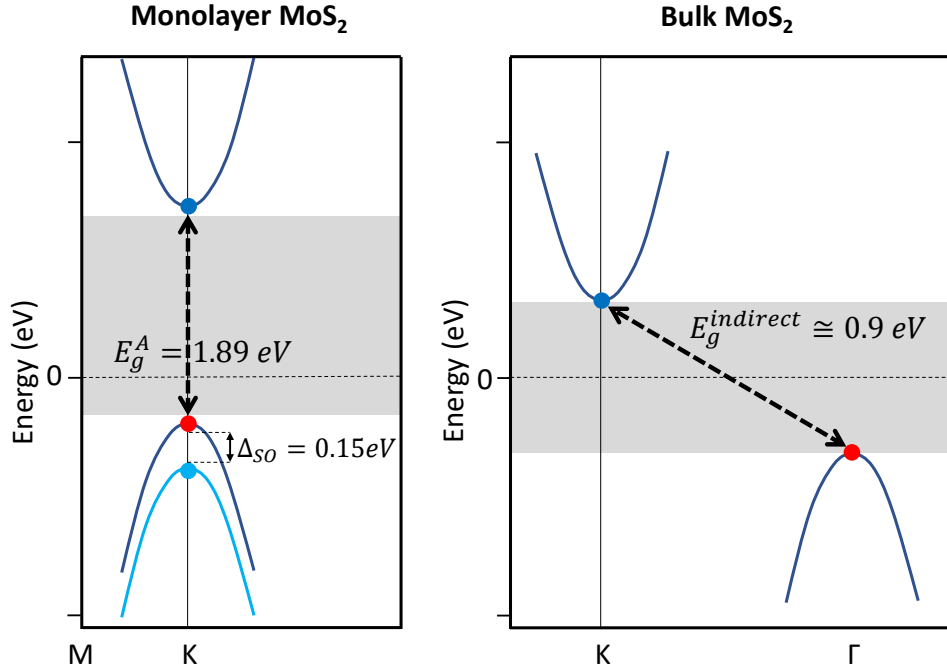


Figure 3.9: Simplified band structures of MoS<sub>2</sub> depending on the layer thickness. On the left, atomically thin layers of MoS<sub>2</sub> present a direct band gap  $E_g^A$ . On the right side, bulk MoS<sub>2</sub> has an indirect band gap  $E_g^{indirect}$ .

The specific optical properties of monolayered MoS<sub>2</sub> include a direct band gap of 1.89 eV, as depicted in figure 3.9. Additionally, numerous investigations have demonstrated the possibility to tailor this direct band gap by means of an externally applied electric field or mechanical strain [111]. A monolayer of MoS<sub>2</sub> has been reported to absorb up to 24 % of the incident light with energy above the band gap [112].

As in all TMDs, MoS<sub>2</sub> is subjected to a spin-orbit splitting of the valence band  $\Delta_{SO}$ , translating into two different excitonic transitions between the valence and conduction bands around the K and K' points of the Brillouin Zone. As demonstrated in figure 3.9, the photogenerated excitons of monolayered MoS<sub>2</sub> are [113]:

- A) The transition between the CB and higher branch of the VB defines the band gap energy of  $E_g^A = 1.89$  eV, and yields the A exciton with a corresponding wavelength of 655 nm.
- B) The lower branch of the of the VB has a the lower energy of  $E_g^A + \Delta_{SO} = 2.04$  eV and bears the B exciton with 608 nm.
- C) Additionally, a broad and strong resonance at  $E^C = 2.9$  eV (428 nm) labelled as C feature arises from exciton resonances at the band nesting region, and has been assigned to van Hove singularities in the density of states<sup>4</sup> [114].

---

<sup>4</sup>Not depicted in figure 3.9.



### P type layer

The P-type layer of a junction is made of a hole-rich material that can act as an electron donor. In the case of the present study, an organic semiconductor under the name of *dinaphtho*[2,3-*b*:2'3'-*f*]-*thieno*[3,2-*b*]-*thiophene* (DNTT) is used. The molecular structure of DNTT is depicted in figure 3.10.

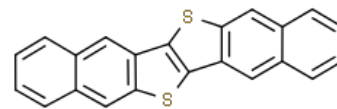


Figure 3.10: Molecular structure of DNTT.

Organic semiconductors are insulators by nature, but can be easily tailored into semiconducting materials upon photoexcitation, with controlled doping, or by injecting charge carriers through electrodes. The biggest advantage of using organic semiconductors is that the manufacturing process is very cost effective, as they are easy to deposit into nanosheets, and therefore layer fabrication is quite unproblematic. Moreover, they present a relatively low dielectric screening compared to other "naturally" semiconducting materials [109].

**Optical properties of DNTT thin films.** A few methods for the fabrication of thin DNTT films offer the possibility to create macroscopic crystalline grains of about 4 to 6  $\mu\text{m}$  that support the semiconducting behaviour of DNTT [109]. Due to the original insulator nature of DNTT, its energy levels are described as discrete molecular orbitals, in opposition to the typical continuous bands of semiconductors, explained in detail in section 3.1.1. In this manner, as shown in figure 3.11, the band gap of DNTT is located between the lowest unoccupied molecular orbital (LUMO) and highest occupied molecular orbital (HOMO), equivalents to the conduction and valence bands of semiconductors, respectively.

Figure 3.11 depicts the band gap of DNTT of 3 eV (413 nm). This transition gives rise to a broad absorption band from 2.6 to 3.2 eV (477 to 387 nm) [94]. Band gap engineering is possible in DNTT by tuning the molecular and ligand design (and not by tuning the crystalline structure as previously seen for TMDs). DNTT nanosheets photoexcited with or above the band gap energy experience excitonic transitions resulting from a mixing of Frenkel excitons with charge-transfer states [115].

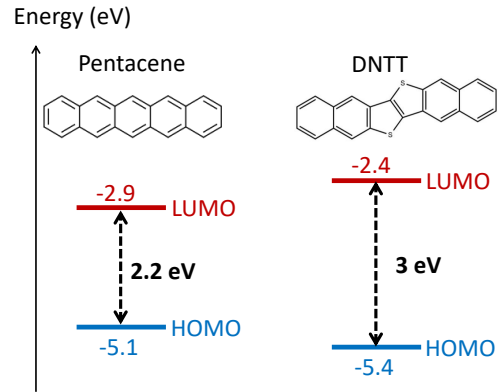


Figure 3.11: Comparison of the band gap and molecular structure of pentacene (left) and DNTT (right).

**Why DNTT?** Previous literature reports have investigated the combination of MoS<sub>2</sub> with pentacene as the organic P-type semiconductor of the vdW heterostructure [84]. These investigations have proven a good coupling between the two layers of the PN junction by the identification of an ultrafast interlayer hole transfer of 6 ps. The main problem of pentacene is that it does not offer a good stability for device applications. The reason is that it degrades in ambient conditions due to its high-lying HOMO that facilitates air oxidation [116]. The ideal candidate to investigate for optoelectronic applications of vdW type II heterojunctions is DNTT, since it is an organic semiconductor from the same family as pentacene with a similar molecular structure, as compared in figure 3.11. More importantly, DNTT offers a great chemical stability in air and a high charge-carrier mobility of  $8 \text{ cm}^2/\text{V} \cdot \text{s}$  [117]. Additionally, the field-effect mobility for DNTT is twice as high than for pentacene, which makes it a great choice for the construction of organic field effect transistors [93].

For this reasons, the current research on DNTT revolves around optimizing the manufacturing methods to obtain stable DNTT nanosheets [116], as well as developing an experimental understanding of the exciton dynamics of the fabricated DNTT layers [115] for applications in organic transistor technology.

## 3.2 Methodology

A full characterization of the photoactivated transitions of the bilayer system under study will be discussed in the following sections. For this purpose, measurements of steady state and excited state absorption spectroscopy are presented. The latter are obtained by transient absorption spectroscopy (TAS), an intricate optical technique that deserves a full chapter of its own, described in detail in the previous section 2.3.1.

### 3.2.1 Experimental design

The purpose of this analysis is to ascertain whether the two distinct layers at the heterostructure are coupled and if they behave like the envisioned PN junction described in the previous sections. In order to carry out such investigation, the exciton dynamics of the heterostructure will be closely compared to the behaviour of the photogenerated excitons of each individual layer. Precisely, the exciton dynamics of the MoS<sub>2</sub> layer are closely examined, and specifically, how their evolution is affected in presence of the layer of DNTT.

### 3.2.2 Samples

The former exploration is performed by comparing the data of three different sets of samples. The full characterization of the heterostructured system is required, but it is also essential to typify the performance of the individual layers of MoS<sub>2</sub> and DNTT. This establishes a reference frame in which to compare the response to light absorption of the heterostructured samples.

All the samples discussed in this chapter have been manufactured externally by two collaborating groups:

1. Emad Najafidehaghani from the Molecular Nanotechnology group of Prof. Andrey Turchanin in *Friedrich Schiller University Jena* synthesised the layer of MoS<sub>2</sub>. During the descriptions in this chapter, this collaboration partner and their work will be referred to as *collaborator 1*.
2. Sirri Batuhan Kalkan from the Soft Condensed Matter group of Prof. Joachim Raedler in *Ludwig-Maximilians-University Munich* deposited the layer of DNTT, either directly on a same substrate (for reference DNTT samples) or on top of the aforementioned MoS<sub>2</sub> layer, making the PN junction or heterostructure. He will be referred to as *collaborator 2*.

For completion, a short description of the fabrication method is provided in the following paragraphs; more detailed information can be found in the cited references.

### MoS<sub>2</sub>

Two reference samples of MoS<sub>2</sub> with a surface area of approximately 50 mm<sup>2</sup> each were produced and transferred onto quartz substrates of 1 mm thickness by *collaborator 1*. By means of optical microscopy and atomic force microscopy (AFM), they have also corroborated the quasi-monolayer quality of the MoS<sub>2</sub> samples, with 1 nm thickness. The reason to call them "quasi-monolayers" is that the single-layer calibre can be only endorsed locally in small regions, where other points of the sample will show a more clustered and rough appearance, as can be seen in the larger-scale microscopy image in figure 3.12(d).

**Fabrication of MoS<sub>2</sub> monolayers** A monolayer of MoS<sub>2</sub> is grown on a silicon wafer by a modified process of CVD with Knudsen-type effusion cells. This method was developed by the group of *collaborator 1* to allow a precise control over the flow rate of precursors, which has a direct effect on the crystalline quality of the resulting TMD monolayer [104].

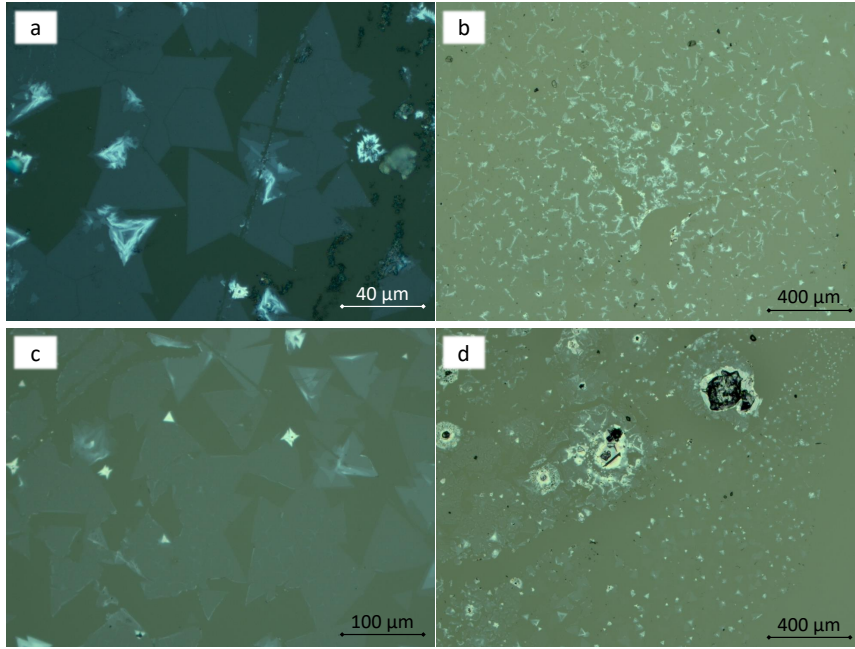


Figure 3.12: Optical microscopy images of the two samples of  $\text{MoS}_2$  transferred on quartz. a and b are different scales of a same sample, also for c and d. The data contained in this figure was provided by *collaborator 1* [personal communication].

The CVD grown layers can be subsequently transferred onto a new silica substrate by employing an assisted transfer protocol with poly(methyl methacrylate) (PMMA). In order to fix the  $\text{MoS}_2$  monolayer into the new substrate and remove the PMMA support, the system is first baked at  $90^\circ\text{C}$ , immersed in acetone, and dried with nitrogen [105].

## DNTT

With the purpose of comparing the effects of the organic layer thickness on the coupling between the distinct layers of the heterostructure, three different thickness of DNTT were fabricated: 15 nm, 55 nm and 100 nm. This comparison also useful to draw conclusions about the thickness of the depletion region, and the efficiency of charge transfer, as discussed in the concluding section 3.5.

**Fabrication of DNTT layers.** Similarly to other organic materials, DNTT is grown by direct sublimation to form a nanosheet layer;

the epitaxial growth method used by *collaborator 2* is known under the name of Stranski-Krastanov [109]. The layer thickness can be controlled during the process of adsorbate sublimation by tuning the evaporation rate and adjusting the waiting time until the desired thickness is reached, which is controlled *in operando* by quartz crystal monitors.

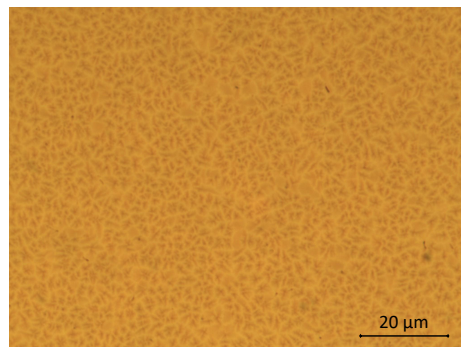


Figure 3.13: Microscope image of a DNTT layer

As the aim is to grow layers with highly ordered molecules, it is important to choose a pertinent substrate whose surface properties support a crystalline growth of the DNTT nanosheet. *Collaborator 2* and their team have developed a specific technique to tackle this issue. As reported in [109] the use of water-soluble polyacrylic acid (PAA) templates on silicon wafers was demonstrated to be an excellent growth substrate to form highly crystalline organic nanofilms. Once the DNTT growth is completed, the sacrificial PAA layer is dissolved, and the mechanically stable DNTT nanosheet is controllably released by means of a water-assisted transfer technique [118]. This step preserves the polycrystalline morphology of the DNTT nanosheet and allows its transfer into any substrate of choice, let it be an empty quartz substrate (for reference DNTT samples) or on top of the aforementioned layer of  $\text{MoS}_2$  (constituting a heterostructured system).

### Heterostructures: making the PN junctions

Equivalent to the various calibers of reference DNTT samples, three different batches of heterostructures are produced, varying the thickness of the top layer of DNTT, while the 1 nm layer thickness of MoS<sub>2</sub> is kept constant. Figure 3.14 represents the final disposition of the heterostructured system; however, it should serve only as a schematic depiction, since it does not account for the roughness of the single layers, the dimensions are not in scale and, as the DNTT nanosheets are polycrystalline, the orientation of the DNTT molecules is only valid locally.

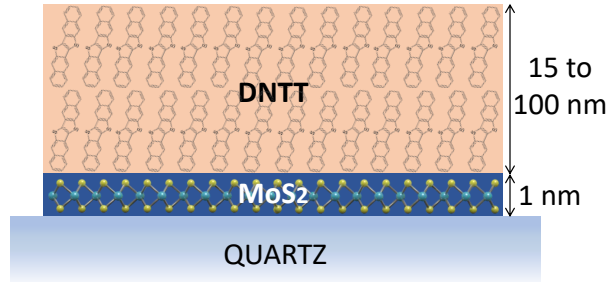


Figure 3.14: Sketch of the heterostructure and the ordered molecular structure of MoS<sub>2</sub> and DNTT. Sizes are not in scale.

### 3.2.3 Steady state absorption measurements

To investigate the light absorption of the systems under study, a commercial UV-Vis Spectrometer Jasco V-530 is utilized in the wavelength range from 330 to 900 nm with the built-in halogen lamp as excitation light source. With this standard machinery, the illuminated sample area is a rectangular-shaped region of about 2x10 mm<sup>2</sup>. For this reason, measurements of steady state absorption do not allow discerning between the different environments of the sample, arising from the uneven and rugged nature of the deposited layers. Instead, the retrieved linear absorption is an integrated result of all the different domains of the sample surface.

Moreover, the sample holder inside the UV-Vis Spectrometer must be modified, since its typical holder can only support cuvettes. For this purpose, the baseplate of the sample



container is removed, giving access to the underlying optical table, in which a thin film holder support is installed.

### 3.2.4 Transient absorption measurements

In the following paragraphs, only those adjustments and parameters that are specific to the measurements of the samples in this section 3.2.2 are described. The working principle and the details of the experimental setup are extensively described in section 2.3.1.

#### Parameters and arrangements in TAS

- The peak pump wavelength is set to 400 nm to excite the transitions of both layers of MoS<sub>2</sub> and DNTT. The frequency-tuning of the fundamental source laser (800 nm), is achieved through second harmonic generation with a BBO crystal. For a brief evaluation the pump wavelength is also tuned to 620 nm to excite the A and B excitons of the MoS<sub>2</sub> monolayer only, via optical parametric amplification (more details to be found in section 2.3.1).
- The repetition rate of the laser source is maintained at 1 kHz.
- The average power of the pump pulses is set to 400  $\mu W$ .
- The diameter of the pump beam at the sample position is  $300 \pm 50 \mu m$ . The diameter of the probe beam at the sample position is made to be slightly smaller, about  $225 \pm 50 \mu m$ .
- To allow for vertical and horizontal scanning of the thin film, all samples are held on a thin film support, mounted on a vertical translating optical post, on top of a linear translational stage.

- Every point in TA data is a result of averaging 300 probe pulses per scan, and a total of 8 scans.
- The data is fitted by GLA, using a parallel model, as described in the previous section 2.3.

**Measurement procedure** All the samples mentioned in section 3.2.2 containing MoS<sub>2</sub> are measured in at least five different spatial points. This procedure intends to account for the different environments present at the samples, originated from the inhomogeneous nature of the MoS<sub>2</sub> layer, as can be seen from their microscope images of figure 3.12. Specifically, those areas with clustered accumulation of MoS<sub>2</sub> are avoided for TAS measurements, since they present a high scattering and consequently high levels of noise. Alternative sample positions with different signal intensities are involved for the full characterization. Nevertheless, the interest is to select those sample regions with low (but measurable) TA signal from MoS<sub>2</sub>, identified by its characteristic excitonic features above 600 nm, that are shown in detail in the following section. These domains would presumably correspond to single monolayered MoS<sub>2</sub>, which is in fact the heterostructured system of relevance to investigate.

Moreover, the heterostructures are measured from both sides with the purpose of investigating the disparities in TAS signal when the DNTT layer is illuminated first (front side of the heterostructure), compared to MoS<sub>2</sub> layer being illuminated first (back side of the heterostructure). This is achieved by simply placing the heterostructure at the sample holder backwards.

For simplicity, only the most representative result are shown in the next *Results* section.

### 3.3 Results

The characterization of the heterostructured samples must focus on identifying the coupling dynamics, i.e., the appearance of transitions and photoproducts originated solely from the effect of coupling between the layers conforming the heterostructure. As mentioned in the previous section 3.2.1, it is of utmost importance to first identify the photoinduced dynamics of each individual layer, for which reference samples of MoS<sub>2</sub> and DNTT are utilized. Subsequently, the heterostructure is investigated under the same conditions of light exposure, allowing for the direct comparison of the excitation dynamics.

From now on, the three different thicknesses of DNTT are referred to with the following nomenclature: "L" stands for *large*, and therefore refers to the thickest DNTT: 100 nm. "M" represents *medium* and corresponds to those DNTT layers with thickness 55 nm. At last, "S" denotes *small*, referring to the thinnest DNTT layers of 10 nm. A compendium of this terminology can be found in table 3.1.

Table 3.1: Nomenclature of different DNTT thickness.

Prefix	DNTT layer thickness (nm)	Name of reference DNTT layer	Name of heterostructure
L	100	L-DNTT	L-het
M	55	M-DNTT	M-het
S	15	S-DNTT	S-het

#### 3.3.1 Steady state absorption (SSA)

The first set of results are intended to analyse the linear absorption of the reference layers of MoS<sub>2</sub> and DNTT, and the heterostructures. The experimentally obtained data of the reference layers are also contrasted with literature findings of similar unilayers of MoS<sub>2</sub> and DNTT [94, 106, 108, 110, 113, 115, 119, 120]. To this date, no reports have been

found describing heterostructures composed by the exact same materials.

Figure 3.15 shows the steady state absorption (SSA) of the reference samples of MoS<sub>2</sub>. The labelled broad absorption peaks denote the position of the photogenerated A (654 nm), B (609 nm) and C (430 nm) excitons of MoS<sub>2</sub> monolayers. As suggested by the cited report [113], the C exciton arises from the photoexcited electronic transition from the deep valence band to the conduction band.

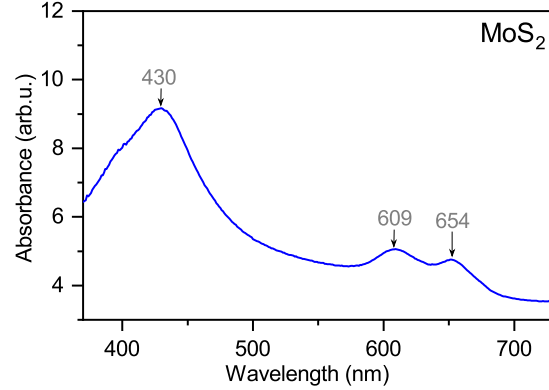


Figure 3.15: Steady state absorption of MoS<sub>2</sub> monolayer.

The same study attributes the A and B excitons to spin-orbit splitting of the valence band, but reports the A and B exciton peak wavelengths to be 660 nm and 614 nm respectively [113]. The small discrepancy between the reported and the measured peak positions is likely due to the different precursors and techniques employed for the fabrication of the MoS<sub>2</sub> monolayers.

Figure 3.16 displays the SSA of the different calibres of DNTT reference layers. Unsurprisingly, the absorption intensity of the DNTT films increases linearly with higher layer thickness, as depicted in the inset of figure 3.16. Although the SSA spectra of all three layers is very similar, there is a slight blueshift of the peak wavelength of the highest absorbing band; for S-DNTT (the thinnest DNTT reference layer) the highest peak is located at 452 nm whereas for L-DNTT (thickest DNTT reference layer) is located at 446 nm. This blueshift indicates a broadening of the band gap of DNTT, probably due to a reduced out-of plane electric screening in thinner DNTT sheets.

Previous research in DNTT thin films reports an equivalent broad ground state absorption below 490 nm, with peak wavelengths at 450 nm and 425 nm; these absorption bands are reported to correspond to clusters of vibronic transitions of excitons with intermolecular charge transfer characters [115]. Nevertheless, the increased thickness does not significantly modify the SSA of the DNTT, at least within the investigated range.

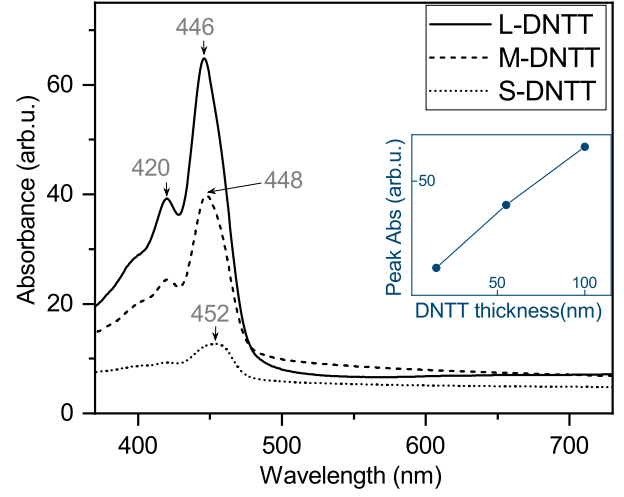


Figure 3.16: SSA of DNTT layers of different thickness. Inset: correlation between peak absorbance and layer thickness.

Figure 3.17 presents the SSA of the different heterostructures with various thicknesses of DNTT top layer. Below 500 nm wavelength, the absorption spectra is dominated by the DNTT layer, presenting the exact same peaks for every distinct calibre. Although they are not very prominent, one can also see the characteristic signatures of the A and B excitons of the underlying MoS<sub>2</sub>, at 653 nm and 607 nm, respectively. This is a first indication that the DNTT is transparent (or transmissive) enough to let the incident light arrive to the MoS<sub>2</sub> layer and photoexcite it.

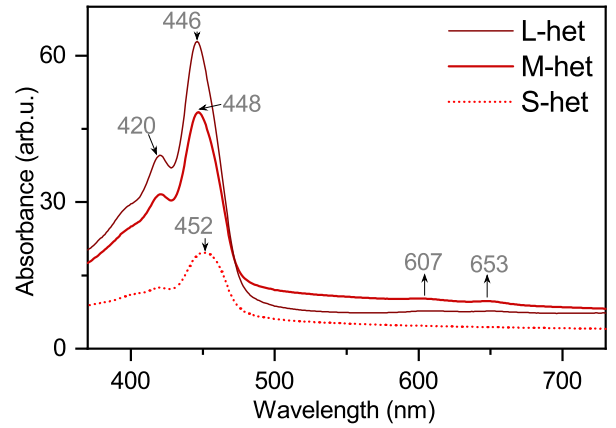


Figure 3.17: Steady state absorption of the heterostructures with different DNTT layer thicknesses.

This forecasts that both layers can be optically pumped at the same time so that their respective excitons can be photogenerated at the two layers simultaneously.

### 3.3.2 Transient absorption spectroscopy (TAS)

In this section, the results of TAS are presented with the aim of investigating the photo-induced dynamics of the various thin film systems.

The main set of measurements for all thicknesses is made by pumping at 400 nm, where both layers of MoS<sub>2</sub> and DNTT efficiently absorb, as seen in the SSA measurements of the previous subsection 3.3.1. Additionally, I wanted to investigate two further scenarios: On the one hand, the variations in exciton dynamics of the MoS<sub>2</sub> monolayer if the pump is set to be resonant with the coupled A and B excitons, i.e., at 620 nm. On the other hand, the TAS signal of the heterostructure placed in the sample holder backwards, illuminating the MoS<sub>2</sub> side first. Therefore, this section will be dedicated to present the results and give a brief analysis of the interesting features and comparisons. Only those results that are relevant for an in-depth analysis of the coupling between layers are taken into the succeeding section 3.4.

#### MoS<sub>2</sub>

The results of exciting a monolayer of MoS<sub>2</sub> at 400 nm are presented in figure 3.18. In the spectral region from 400 upto 450 nm, MoS<sub>2</sub> reveals a strong ground state bleach, negatively contributing to the TAS signal, that indicates a strong absorption of the incident 400 nm pump pulses and the generation of C excitons. Moreover, the typical signatures of the A and B excitons also manifest as negative peaks at 675 nm and 617 nm, respectively, that is equivalent to the one for the C excitonic transition. With this observation, it becomes clear that the photogeneration of the C exciton via optical

pumping at 400 nm can efficiently trigger the formation of the A and B excitons, which points towards the notion that all A, B and C excitons of the MoS<sub>2</sub> monolayer are coupled, as suggested in the literature [113].

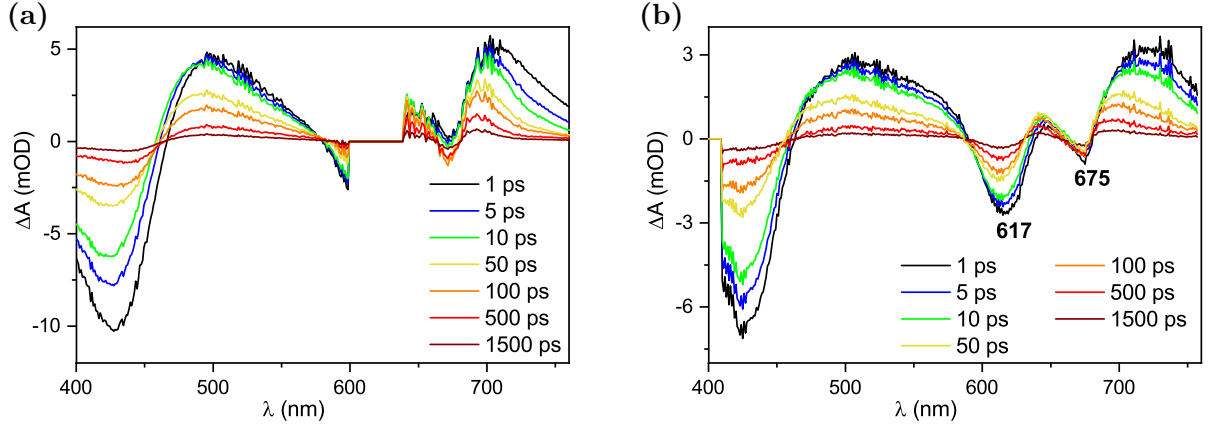


Figure 3.18: TAS of the MoS<sub>2</sub> monolayer with excitation pump at (a) 620 nm and (b) 400 nm.

With the purpose of exploring the preceding conjecture, the same monolayered MoS<sub>2</sub> sample is investigated under 620 nm excitation pump, as presented in figure 3.18(a). By the direct comparison of these two TAS measurements in figure 3.18(b), one can unequivocally assure that the shape and decay rate of the TAS signal is equivalent when pumping either C or A and B excitons (at 400 and 620 nm respectively), which proves the hypothesis that the exciton dynamics of A, B and C are indeed coupled.

Herewith, let us now focus on the TAS signal of the MoS<sub>2</sub> monolayer excited at 400 nm, displayed in figure 3.18(b). The excited state peak positions of the A (675 nm) and B (617 nm) excitons in TAS are redshifted with respect to those same peaks in steady state absorption measurements (654 nm for A exciton and 609 nm for B exciton), presented in the previous section 3.3.1, in figure 3.15. The magnitude of this spectral shift is much more pronounced for the A exciton, consisting of a 21 nm (59 meV) redshift, compared to the

only 8 nm (26 meV) redshift of the B exciton. Literature investigations on the excited state dynamics of monolayered MoS<sub>2</sub> assign the origin of this redshifted ESA to band gap renormalization due to Coulomb interactions within the 2D film [113, 120].

Additionally, when comparing the SSA in figure 3.15 with the TAS in figure 3.18(b) one can appreciate that the relative intensity ratios of the absorption peaks in SSA do not match with the ratios of the negative features of the TAS signal. Precisely, there is more contrast in the negative peak intensities of the TAS: the intensity of the C-excitonic feature is 3 times higher than the one of the B-excitonic signature (2 times in SSA), which in turn is 3 times higher than the intensity of the A-excitonic feature (only about 1.2 times higher in SSA). This indicates that there are further negative contributions to the TAS signals from the A and B excitons corresponding to stimulated emission, that result from the emission arising from the excitonic recombination through the direct band gap transition of MoS<sub>2</sub>.

**Kinetics of MoS<sub>2</sub>** As described in the first chapter in section 2.3.1, the TAS signal versus time (so-called kinetics) can be fitted through a superposition of single exponential functions. In the case of MoS<sub>2</sub>, the experimentally-retrieved kinetics can be precisely fitted by using three decay times,  $s_1^M$ ,  $s_2^M$ ,  $s_3^M$ <sup>5</sup>. These decays are attributed to their corresponding transitions by identifying the analogies with previous literature reports [110, 113, 121–123].

Nevertheless, the first photoinduced signature cannot be experimentally resolved, since it arises together with the pump-probe overlap and therefore it is superimposed with the inherent coherent artifact. This initial photoexcitation corresponds to the photogeneration of the A, B and C excitons that, in agreement with the literature, happens in a sub-ps

---

<sup>5</sup>Errors are calculated by averaging the decay times of 8 fits from different data sets.



regime [122]. These photoinduced excitons possess a high binding energy of around 500 meV and a Bohr radius of  $\approx 1$  nm [110]. These bound electron-hole pairs can recombine radiatively or non-radiatively within the following experimentally-resolved lifetimes:

- $s_1^M = 5 \pm 1$  ps: Non-radiative fast relaxation of charge carriers at A and B exciton bleach bands, leading to a partial annihilation of the photogenerated excitons [122]. Electrons and holes of the bound excitons at the MoS<sub>2</sub> monolayer can be captured by intra-band gap defect states; this can happen either as a result of Auger processes, in which charge carriers transfer to a vacancy generated by a point defect of the semiconductor lattice [123], or in form of charge carrier trapping instigated by surface defect states [122].
- $s_2^M = 61 \pm 3$  ps: Recombination of Coulomb-bound excitons. Coulomb interactions between charge carriers are enhanced in TMDs due to their 2D nature (and therefore lack of out-of-plane confinement) [110]. For this reason, this recombination lifetime depends on thickness of MoS<sub>2</sub> layers, and it has been reported to slow down up to three times for bulk MoS<sub>2</sub> [113].
- $s_3^M = 550 \pm 80$  ps: Attributed to the slow (or long-lived) direct (and therefore radiative) interband recombination [122].

## DNTT

In this subsection, the TAS results of the three calibres of DNTT nanosheets are presented in figure 3.19 and discussed. The ESA of the thicker L-DNTT and M-DNTT, shown in figures 3.19(a) and 3.19(b) respectively, reveals alike TA signals, pointing towards an identical excitonic behaviour in the thicker layers.

It is common to all DNTT layer thicknesses the presence of a derivative-like feature below 500 nm, that modulates the TAS signal during the entire range of experimentally-accessible pump-probe delay. The fitted lifetime of this long-lived feature corresponds to  $s_3^D = 10 \pm 1$  ns, and literature suggests that it becomes steady at  $\geq 1$  ns [115]. This change in signal shape happens upon partial decay of the mixed Frenkel and charge transfer (CT) excitons. As the exciton energy is dissipated as heat, an additional rise of a growing positive contribution is observed, due to thermal effects. As a matter of fact, the TAS kinetics of all three thicknesses of DNTT can be fitted with the same three decay rates.

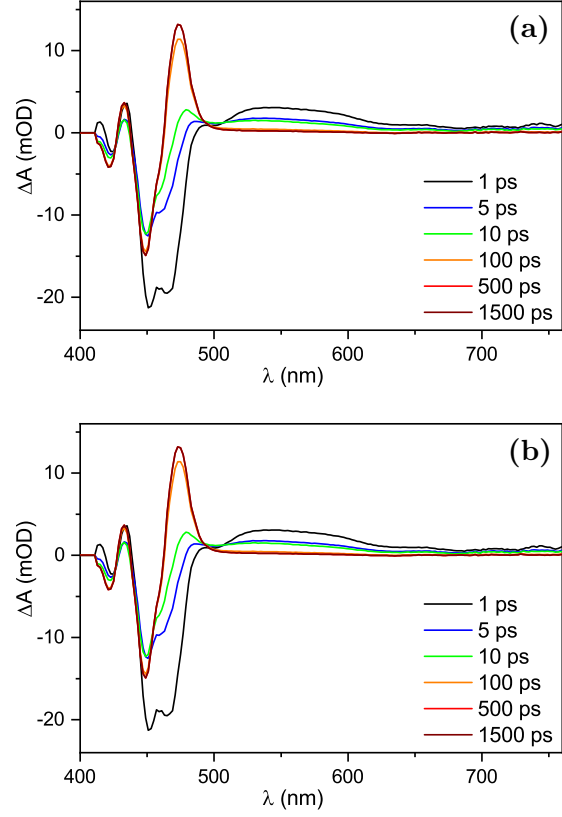


Figure 3.19: TAS of DNTT nanosheets with thicknesses: (a) L-DNTT and (b) M-DNTT, pumped at 400 nm.

The shortest experimentally resolved transition is  $s_1^D = 1.8 \pm 0.2$  ps, assigned by previous investigations to partial internal conversion of the mixed Frenkel-CT excitons towards the lowest singlet excitonic level  $S_1$ . The second lifetime retrieved from experiments is  $s_2^D = 80 \pm 10$  ps, attributed to the relaxation lifetime of the singlet excitons [115].

As suggested from the SSA of DNTT presented at the previous section in figure 3.16, DNTT of any thickness can strongly absorb the pump pulses at 400 nm, but that does not necessarily translate into a negative TAS signal from ground state bleach. This is the case of the thin S-DNTT nanosheet shown in figure 3.20, where the spectral region around the pump is, in fact, showing a positive TA signal.

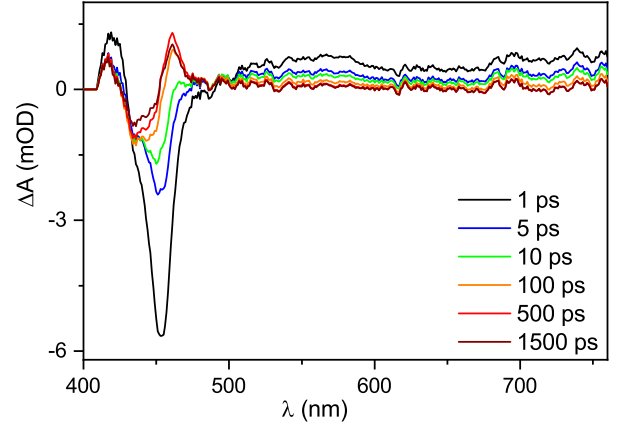


Figure 3.20: TAS of S-DNTT, the thin reference layer of DNTT with 15 nm thickness, pumped at 400 nm.

Previous literature reports assert that this counterbalancing positive contribution arises from a Stark shift in the ground state absorption, caused by the local electric field generated from the CT exciton, upon the neighbouring DNTT molecules [115, 124].

To the best of my knowledge, the dependence of the intensity of the Stark effect on DNTT layer thickness has not (yet) been reported in the literature. Notwithstanding, the fact that the thin S-DNTT presents a positive TA signal right above 400 nm suggests that this Stark effect is stronger in thinner samples. This finding insinuates either one, or both of these following scenarios: Either the photogeneration of the CT exciton is enhanced in thinner DNTT, or the decrease in bulk thickness reduces the screening of the local electric field generated by the CT exciton, and therefore the Stark effect extends over an ampler surrounding. This is an important feature of the thin S-DNTT sample, whose implications in the layer coupling at the PN junction are further discussed in the subsequent section 3.4.

### Heterostructures

This subsection is dedicated to present three sets of data of the heterostructured system, composed by the two semiconducting layers as previously explained: three different thicknesses of DNTT on top of MoS<sub>2</sub>. Additionally, a test measurement is performed from the back side of M-het, to examine the TA signal variations if the back surface (i.e., the MoS<sub>2</sub> layer) of the heterostructure is illuminated first.

As a general remark for all the TA signals of the heterostructures, presented in figures 3.21, 3.22, and 3.23, in the spectral region below 500 nm the layer of DNTT dominates the signal, as it shows the exact same ESA as the reference DNTT layers of their same thickness presented in figures 3.19 and 3.20. Conversely, for wavelengths higher than 500 nm the A and B excitons of the MoS<sub>2</sub> layer dictate the excited state dynamics of the heterostructure.

#### L-het

Figure 3.21 shows the TAS of the L-het, i.e., the heterostructure with a 100 nm layer of DNTT. In this first case, the influence of the thick DNTT layer and its intense negative TAS signal from 450 to 500 nm provokes a shift in the y-axis crossing point for early pump-probe delays: from 487 nm at 1 ps delay to 468 nm at 10 ps delay. Regardless, the excitation beam at 400 nm is not fully absorbed by the top DNTT layer,

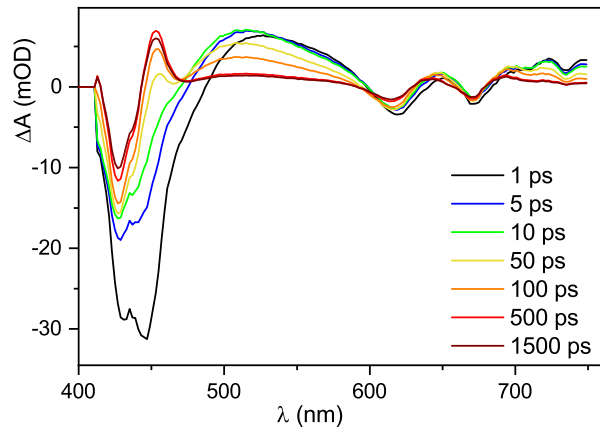


Figure 3.21: TAS of the L-het, i.e., heterostructured sample with a 100 nm layer of DNTT.

allowing it to be partially transmitted to the underlying MoS<sub>2</sub> layer, where it can be also absorbed. This can be noted by recognizing the typical TAS features of the A and B excitons of the MoS<sub>2</sub> layer, that are equivalent to those at the reference MoS<sub>2</sub> monolayer (shown in figure 3.18), since they have a similar amplitude and are spectrally located at the same wavelengths.

In L-het, there is no apparent discernible contribution to the measured TA signal other than the independent exciton dynamics of each individual layer. For this reason, the kinetics of L-het were fitted with a combination of the decay rates derived from each of the layers composing the heterostructure. As a result, a total of four lifetimes were retrieved, which were tentatively assigned to the following transitions in L-het:

- $s_1 = 1.5 \pm 0.8$  ps. Presumably equivalent to  $s_1^D$  from DNTT, reported as internal conversion of the DNTT excitons towards S<sub>1</sub>.
- $s_2 = 5 \pm 3$  ps. Equivalent to  $s_1^M$ , due to the fast trapping of charge carriers in the intraband defect states of the MoS<sub>2</sub> layer, forcing the fast relaxation of the charge carriers of the excitonic bleach bands of MoS<sub>2</sub>.
- $s_3 = 60 \pm 5$  ps. Possibly corresponding to  $s_2^M$  from the decay of the Coulomb-bound excitons generated at the MoS<sub>2</sub> monolayer.
- $s_4 = 10 \pm 1$  ns. Identical to  $s_3^D$  and thus attributed to the long-lived thermal relaxation of the mixed Frenkel-CT excitons of DNTT.

The other time constants that were retrieved from each individual layers but are not mentioned in the previous segment do not play a significant role in the relaxation dynamics of L-het. This does not necessarily mean that the intermediate decay step does not exist at

the L-het; it may only indicate that the kinetics of this specific process are overshadowed by another slower decay.

### M-het

Figure 3.22(a) shows the TA signals of the M-het, i.e., the heterostructured system with a 55 nm layer of DNTT. When pumping the M-het at 400 nm, the ESA resembles the one for L-het in figure 3.21, with decay rates that are also equivalent. Since the DNTT layer in M-het has half the thickness than the DNTT of L-het, a lower signal contribution from the DNTT nanosheet is expected in M-het. In other words, in M-het the negative peak amplitude of the DNTT feature at 425 nm is of the same order as the amplitude of the A-excitonic feature (at 653 nm) of the MoS<sub>2</sub> monolayer; conversely, in L-het the relative amplitude of the aforementioned features is ten times bigger in the case of L-het. As previously appointed for L-het, there is no obvious indication of any mutual influence on the exciton dynamics of each individual layer. For this reason, the kinetics of M-het are fitted with the same aforementioned lifetimes as L-het.

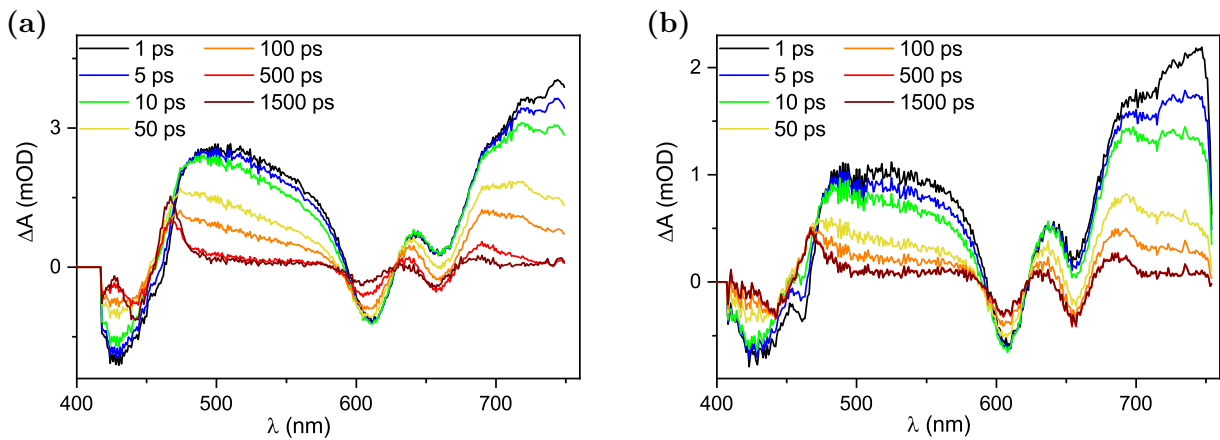


Figure 3.22: TAS of the M-het measured from (a) the front side; (b) the back side.

Figure 3.22(b) displays the TA signal of the same M-het sample measured backwards, i.e., with its back surface facing towards the laser source. Consequently, pump and probe pulses pass through the glass substrate, impinge on the MoS<sub>2</sub> monolayer first, and then the DNTT nanosheet. This experiment yields in a TA signal that is equivalent to that of a front side measurement, which can be observed by comparison of figures 3.22 (a) and (b); the only natural discrepancy is the increased relative amplitude of the A and B excitonic features, arising by exciting the MoS<sub>2</sub> layer first. This is an expected effect, since a higher pump intensity is reaching the MoS<sub>2</sub> layer as it has not been partially absorbed by the DNTT nanosheet yet.

### S-het

Figure 3.23 presents the SSA of S-het, i.e., the heterostructure with a thin (15 nm) DNTT top layer. In this present case, the A and B excitons generated at the MoS<sub>2</sub> monolayer show their ground state bleach features centered at 680 nm and 628 nm respectively, at early delay times (1 ps).

Additionally, these peaks have a five to ten times higher amplitude when compared to the same signatures of the TAS from the reference MoS<sub>2</sub> layer in figure 3.18 and also, their relative amplitude is reversed; at the heterostructure, the A-exciton feature is more pronounced than the B-exciton feature, which is the opposite compared to the reference MoS<sub>2</sub> monolayer.

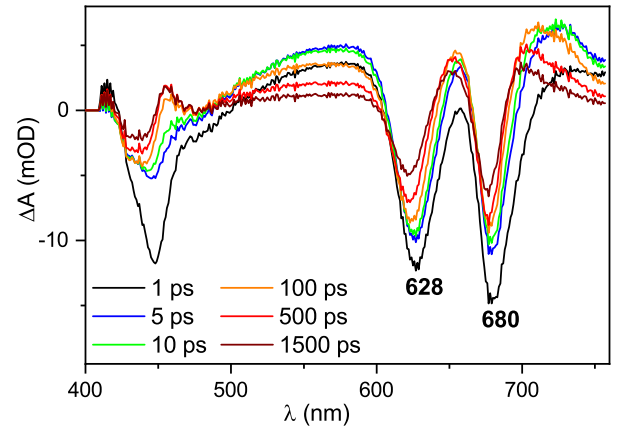


Figure 3.23: TAS of the S-het, i.e., heterostructured sample with a 15 nm layer of DNTT, pumped at 400 nm.

This fact points towards the notion that the excitation probability of the A and B excitons at the S-het is increased at the heterostructure compared to the the excitation probability of the excitons of a MoS<sub>2</sub> monolayer, and that this increase is different for each of the photoexcited excitons.

The latter is not the only transformation in the typical traits of the MoS<sub>2</sub> excitons. In fact, the following two observations are even more interesting for the purpose of our study. On the one side, the A and B excitonic peak positions at the S-het are clearly redshifted with respect to those same features of the MoS<sub>2</sub> reference layers, by 14 meV and 35 meV, respectively. On the other side, the relaxation of these excitations is extensively delayed, from 550 ps in the MoS<sub>2</sub> reference layer, to 2.5 ns at the S-het<sup>6</sup>.

This proves that there are clear changes in the excited state dynamics of the excitons belonging to the MoS<sub>2</sub> layer, due to the presence of S-DNTT. Therefore, for the purpose of analysing the changes in excitonic behaviour of the heterostructure, the data presented in figure 3.23 and the decay rates of the S-het will be extensively discussed in the subsequent section 3.4.

---

<sup>6</sup>These two attributes are not observed in M-het and L-het, fact that will be further discussed in the upcoming section.



### 3.4 Discussion: Coupling analysis

This final section is dedicated to the analysis of the coupling between layers of the heterostructured systems. As the experimental results are already discussed alongside the plotted data in the previous section, the successive discourse only takes into consideration those datasets that contribute to the argumentation. Namely, this concerns the TAS data of the reference MoS<sub>2</sub> monolayer, the DNTT nanosheet with 15 nm thickness (S-DNTT) and the heterostructure with a 15 nm layer of DNTT (S-het). The last subsection 3.4.3 tackles why the succeeding arguments apply only for the thinnest DNTT and not for the other measured compositions, with thicker DNTT layers.

Let us start the presentation of the three sets of TAS data of the aforementioned samples, in figure 3.24. The first obvious observation to make here, as a recapitulation of the preceding section, is that the presence and photoexcitation of both individual layers is obvious at the heterostructure. This can be confirmed by noting that the S-DNTT dictates the ESA below 500 nm, but for longer wavelengths the MoS<sub>2</sub> layer excitonic features take over. Therefore, the observed TA signals at the heterostructure demonstrate that, upon absorption of the 400 nm pump pulses, both A and B excitons (generated from the MoS<sub>2</sub> layer) and the mixed Frenkel-CT excitons (generated at the S-DNTT nanosheet) are photoexcited, and participate in the overall excited state dynamics of the heterostructure.

Nevertheless, the discussion about the effects of layer coupling will focus on the ESA in the spectral region above 500 nm; specifically, most of the following arguments (except one) will be dedicated to inspect the modifications in TA signals of the A and B excitonic features of MoS<sub>2</sub>.

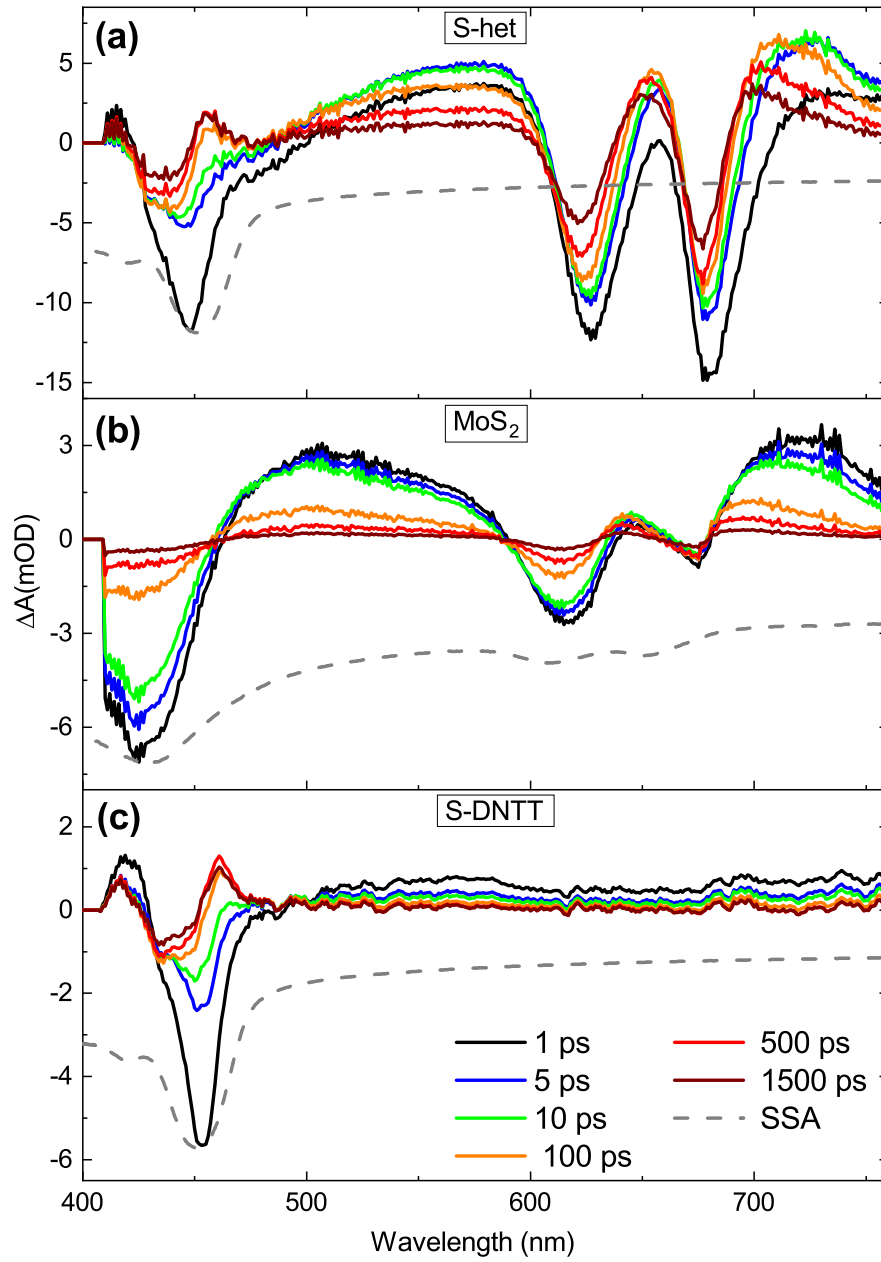


Figure 3.24: TAS of the heterostructure with 15 nm layer of DNTT (a), the MoS<sub>2</sub> monolayer (b) and the thin 15 nm nanosheet of DNTT (c). The grey dashed line represents the normalized inverse if the SSA of each sample. All data contained in the graphs was already presented in the results section.

Prior to the discourse contrasting the MoS<sub>2</sub> excitonic transitions and how they are altered by the presence of S-DNTT, it is worth to enunciate the distinct decay lifetimes  $s_1^{het}$  to  $s_4^{het}$  derived from global fitting analysis of the TAS of S-het. They significantly differ from the retrieved lifetimes of M-het and L-het ( $s_1$  to  $s_4$  presented in the previous section), as the excited state dynamics of S-het provide notable differences in TA signals compared to the TA signals of the heterostructures with thicker layers of DNTT (i.e., M-het and L-het), as discussed at the end of this section. The respective assignments of the decay lifetimes of S-het are explained in detail at the subsequent subsection 3.4.1.

- $s_1^{het} < 1$  ps. Photogeneration of all excitons at the heterostructure and formation of a depletion region near the junction.
- $s_2^{het} = 6$  ps. Interlayer charge transfer. A portion of the majority charge carriers of each layer is transferred across the junction.
- $s_3^{het} = 200$  ps. Assigned to the recombination of the remaining intralayer excitons. As not all the charge carriers are transferred across the junction, those bound excitons that have remained at the MoS<sub>2</sub> layer would recombine faster. This signature appears in the TAS data as a partial recovery (decay to ground state) of the A and B excitonic excitations.
- $s_4^{het} = 2.5$  ns. Long-lived charge separated state for the A and B excitons, with a delayed charge recombination.

### 3.4.1 Indications of layer coupling

The purpose of this final section of the chapter is to discuss the arguments in favour of the coupling between layers at the heterostructure, and to elucidate whether the system behaves like the envisioned PN junction with good optoelectronic qualities, as hypothesised at the beginning of the chapter.

#### I. Redshift of A and B excitonic peaks

The first evidence of the formation of a PN junction arises with the realization of the displaced spectral peak positions of the A and B excitonic signatures, when the MoS<sub>2</sub> layer is part of the heterostructured system. As shown in figure 3.25, these negative peaks at the heterostructure are significantly redshifted at early delay times with respect to those same features of the TA signal of the reference MoS<sub>2</sub> monolayer.

As suggested by literature [84, 119], the instantaneous<sup>7</sup> formation of a depletion region in a PN junction made of a TMD layer, will be accompanied by the redshift of the photoexcited excitonic transitions of this layer.

---

<sup>7</sup>The formation of the depletion region happens in the sub-picosecond regime [119], and therefore is considered instantaneous regarding the temporal resolution of our experiments.

For example, Nie et al. reported a redshift of 14 meV and 10 meV of the A and B excitons, respectively, of MoS<sub>2</sub> in a heterostructure with black phosphorus [119].

The observation in the TA signal of the heterostructure of the 14 meV (5 nm, A exciton) and 35 nm (11 nm, B exciton) redshift compared to the TAS of the MoS<sub>2</sub> layer infers that a depletion region at the boundary between this layer and the DNTT has been formed, and necessarily, that the whole ensemble of the heterostructure operates as a functional PN junction.

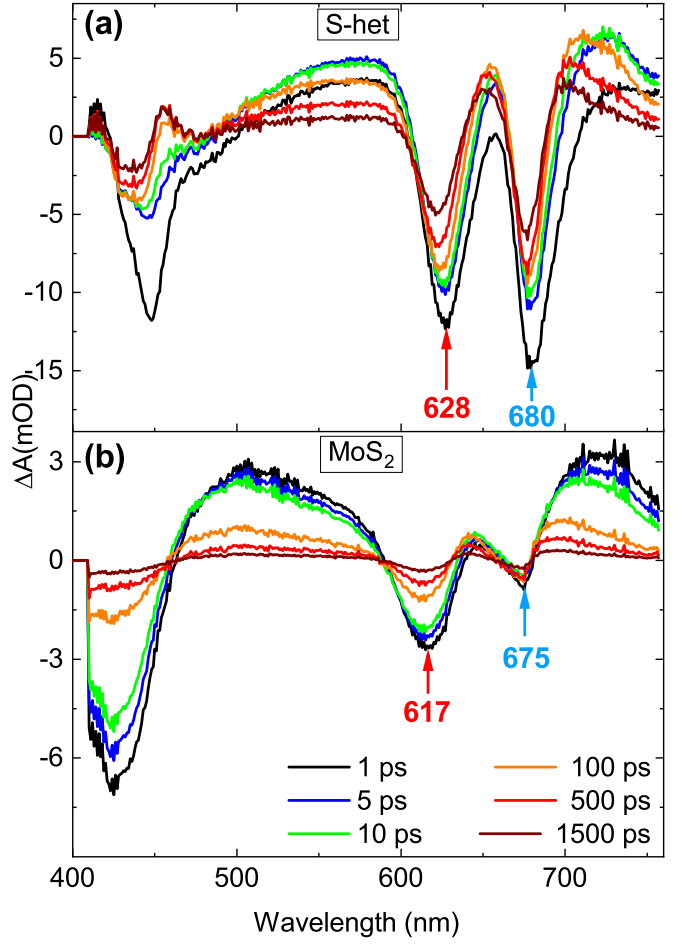


Figure 3.25: TAS of (a) the S-het and (b) the MoS<sub>2</sub> monolayer. The represented data was already shown in the results section.

## II. Interlayer charge transfer

By comparison of the TAS data of the reference MoS<sub>2</sub> and the S-het, one can find three indications that support the attribution of the 6 ps lifetime to interlayer charge transfer:

- i) Photoproduct absorption increasing during the first 6 ps, only in S-het; ii) accelerated decay of the A and B excitonic features in S-het TAS during the first 6 ps; iii) blueshift of the A exciton peak position after 6 ps, only in S-het.

**i) Photoproduct absorption.** The most unambiguous evidence that supports the operational quality of the studied PN heterostructure comes with the recognition of a delayed ESA at the TAS of the heterostructure.

This manifests as a build-up of positive signal in the kinetics<sup>8</sup> plot of figure 3.26. With this kinetics plots one can identify that the increase in positive signal happens during the first 6 ps (corresponding to the second fitted lifetime  $s_2^{het}$ ), at the spectral regions around 540 and 720 nm, and develops only at the heterostructure, where the S-DNTT nanosheet is in contact with the monolayer of MoS<sub>2</sub>. The progressive increase of TA signal during the first 6 ps seems to point towards photoproduct absorption, i.e., a newly emerging species that, as it forms in the heterostructure, triggers the absorption of those probe wavelengths in resonance with its transitions.

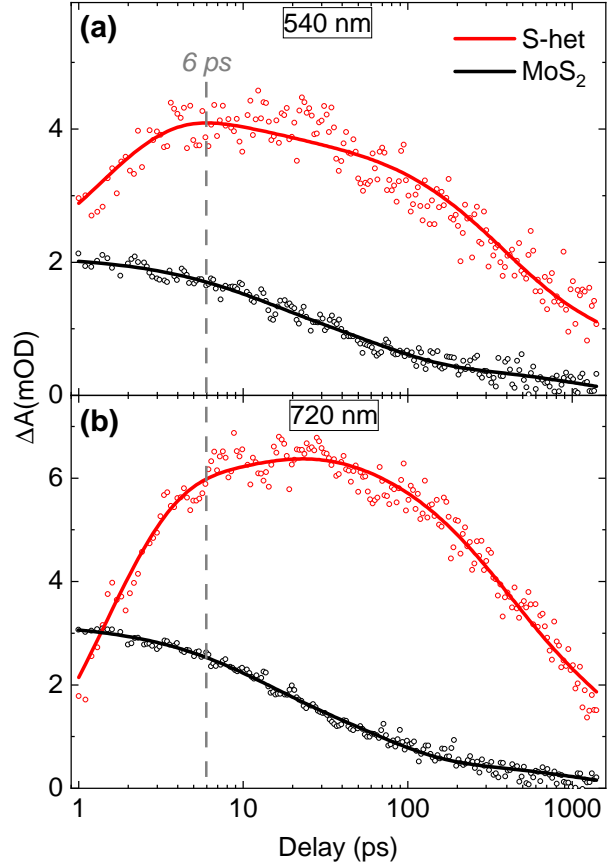


Figure 3.26: Kinetics of the S-het and the MoS<sub>2</sub> reference monolayer at 540 nm (a) and 720 nm (b). The data belongs to the same TAS experiments presented before, now represented as function of pump-probe delay in the x-axis.

<sup>8</sup>In kinetics plots, the sets of TAS data are retrieved from the same measurements explained before, but are now represented as a function of pump-probe delay, for specific wavelengths.

Literature reports show that oxidized DNTT ( $\text{DNTT}^+$ ) presents a featureless absorption band from 620 to 770 nm and a pronounced absorption peak at 540 nm [125]. Therefore the origin of the TA signal build-up can be attributed to the formation of an oxidized layer of DNTT at the heterostructure, as the absorption bands of  $\text{DNTT}^+$  match the spectral regions where the build-up occurs. This implies charge transfer to the  $\text{MoS}_2$ , and hence the function of DNTT as the electron-donor layer of the PN junction is endorsed.

The aforesaid process is sketched in figure 3.27, representing that some excitons dissociate and are transported across the junction, while some others remain bound at their original layer, and will undergo a faster decay (that is related to the lifetime  $s_3^{het}$ ). The formation of the oxidized layer of DNTT ( $\text{DNTT}^+$ ) at the junction boundary it is also depicted; the transfer of holes from  $\text{MoS}_2$  to DNTT, together with the development of a reduced layer of  $\text{MoS}_2$  is also expected, but it is not depicted in the figure as it is not experimentally detected.

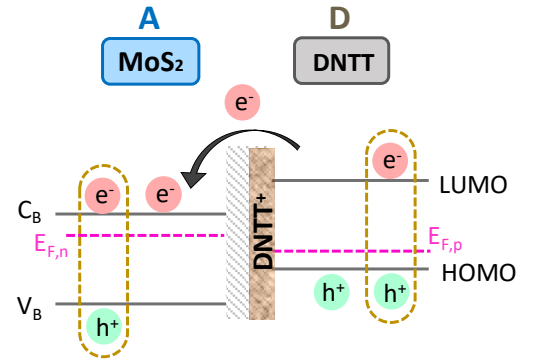


Figure 3.27: Depiction of the interlayer CT at the heterojunction where DNTT donates electrons to  $\text{MoS}_2$ .  $E_{F,n}$  and  $E_{F,p}$  are the Fermi levels of  $\text{MoS}_2$  and DNTT, respectively.

The preceding experimental observation is in good agreement with the literature, as similar vdW heterostructures of  $\text{MoS}_2$  with pentacene are reported to present interlayer hole transfer in a time scale of 6.7 ps [84].

Figure 3.27 displays that the TA signal of S-het becomes about two times higher after the first 6 ps (i.e., after the charge transfer), which can be interpreted as the amount of photogenerated  $\text{DNTT}^+$  absorbers being reasonably big. This assumption would infer

that there are high amounts of electrons transferred towards the MoS<sub>2</sub> monolayer, which can be used as a qualitative indication of an efficient interlayer charge transfer. This may translate as an improvement in the photoresponsivity of the transistors and devices to be fabricated from the proposed combination of materials in a vdW heterojunction.

## ii) Accelerated decay of the A and B excitons in S-het

The comparison of the kinetics of S-het and MoS<sub>2</sub> at the wavelengths of the A (680 nm) and B (628 nm) excitonic features can be found in figure 3.28. The initial decay of both excitons at the heterostructure is accelerated during the first 6 ps, characteristic that is not pronounced in the TAS of the reference MoS<sub>2</sub> layer. This is an expression of an abrupt decrease in the amount of excitons in MoS<sub>2</sub>, which supports the notion that the charge carriers of the A and B excitons are no longer localized at the MoS<sub>2</sub> layer. Instead, they are likely distributed over the two layers of the heterostructure which is only possible after the charge transfer process across the junction.

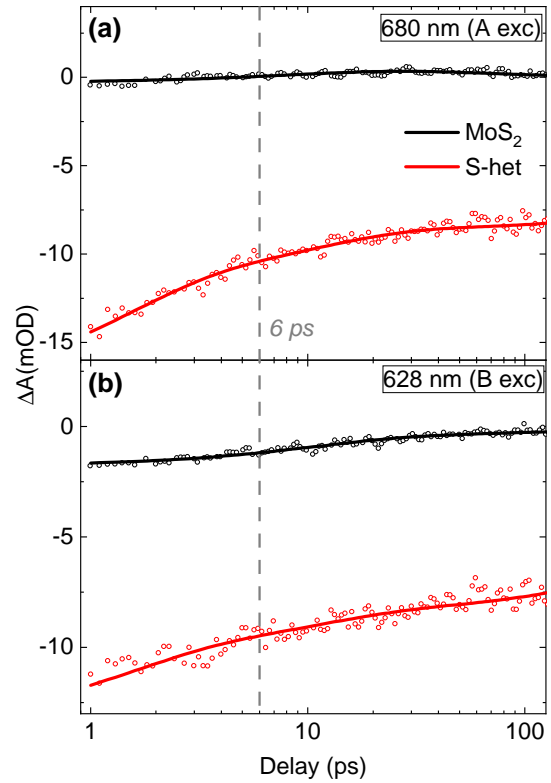


Figure 3.28: Kinetics of S-het and MoS<sub>2</sub> at the wavelengths of: (a) the A exciton -680 nm- and (b) the B exciton -628 nm-.



**iii) Blueshift of the A-excitonic peak in S-het** Aside from the previous observations that compared the kinetics of S-het and MoS<sub>2</sub> in certain wavelengths, another sign of interlayer CT is found while observing the change in the spectral position of the A-excitonic peak in TAS.

As represented in figure 3.29, the TAS of S-het presents an abrupt blueshift of the peak position of the A excitonic feature exactly after 6 ps. This indicates an increase in the band gap energy of the A exciton that is linked to an interlayer CT, as the consequential stretching of the bound A exciton across the junction implies a blueshift (i.e., energy increase) of its spectral signature.

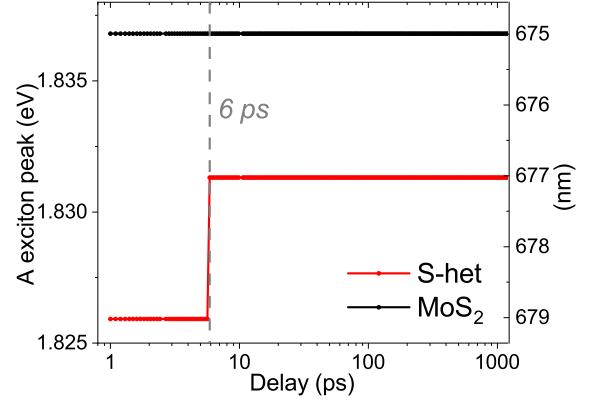


Figure 3.29: Peak position of the A-excitonic feature in TAS for the reference layer of MoS<sub>2</sub> and the S-het.

This blueshift of the A exciton peak after 6 ps delay upon interlayer CT is not observed for the B exciton. To the best of my knowledge, there are no indications in the literature claiming that only the A exciton participates in charge transfer processes. However, in the previous point ii) represented by figure 3.28, one can observe a faster decay during the first 6 ps of the A-excitonic TA signal for S-het, compared to the less accelerated decay of the B exciton in S-het. This supports the argument found in this case, that the A-exciton could be participating more actively in interlayer CT phenomena.

### III. Long-lived charge separation state

As represented in figure 3.30, an extra consequence of having the photogenerated excitons transferred across the junction is that the charge carriers are physically separated in the two local environments of each of the layers at the heterostructure. This makes the charge carriers less available for recombination, which extends the lifetime of the charge-separated A and B excitons to the fitted decay of  $s_4^{het} = 2.5$  ns.

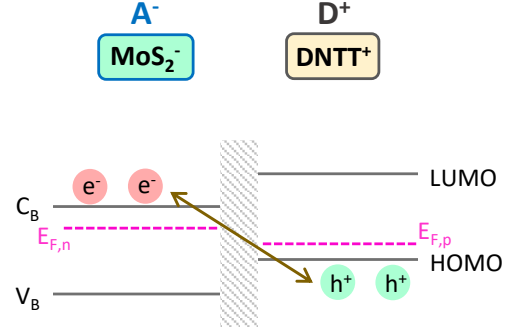


Figure 3.30: Depiction of the long-lived charge separated state at the heterojunction.  $E_{F,n}$  and  $E_{F,p}$  are the Fermi levels of MoS<sub>2</sub> and DNTT, respectively.

In comparison, the A and B excitonic lifetimes of the reference MoS<sub>2</sub> monolayer was about 5 times faster, fitted at  $s_3^M = 550$  ps. The 5 times slower excitonic recombination can also be deduced from the A and B excitonic features of figure 3.25, clearly depicting how their TA signal at the heterostructure is not fully recovered within the experimentally-accessible pump-probe delay. Conversely, this A and B excitonic relaxation is almost fully completed in the reference MoS<sub>2</sub>, where the charge recombination happens within the same layer.

#### 3.4.2 Proposed model for the exciton dynamics

Having discussed all the arguments in favour of a functional PN heterojunction with coupled exciton dynamics, a model of the evolution of the photoexcited transitions can be created, as represented in figure 3.31.

Subfigure 3.31(a) represents the first stage of photogeneration of excitons at both layers of the heterostructure in a sub-picosecond regime upon absorption of the pump pulses, together with the formation of a depletion region near the junction.

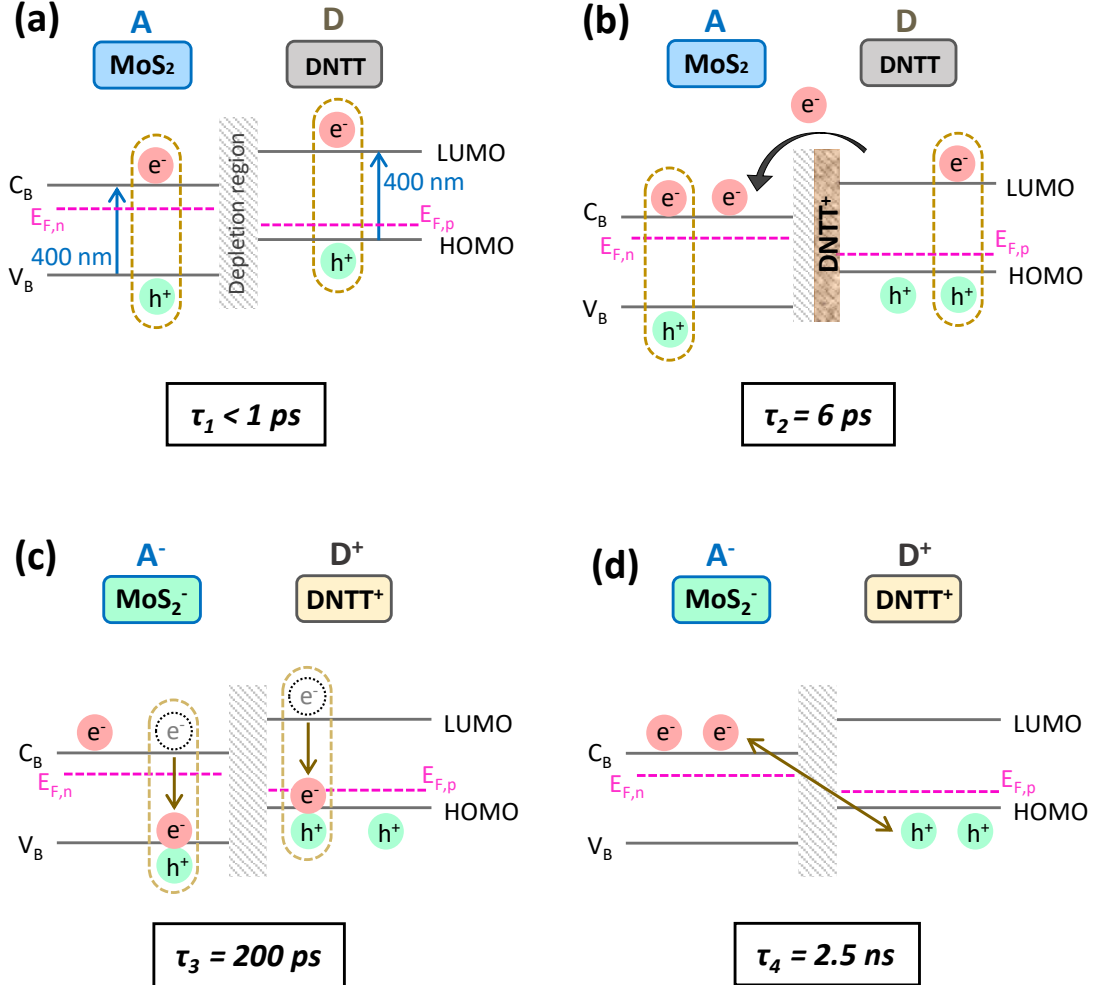


Figure 3.31: Model of the coupled exciton dynamics of the S-het, with the fitted lifetimes corresponding to each stage, derived from the global fitting analysis of TAS measurements.  $E_F$  is the Fermi energy of both layers before the interlayer charge transfer occur. After that, there is a reorganization of the Fermi energies of the individual of MoS<sub>2</sub> and DNTT layers, becoming  $E_{F,n}$  and  $E_{F,p}$ , respectively.

Subfigure 3.31(b) depicts the second proposed step of exciton dynamics. Some of the photogenerated excitons dissociate and the charge carriers are transferred across the junction with a characteristic time constant of 6 ps. The process that is experimentally detected is the formation of oxidized DNTT, depicted in 3.31(b) as a thin layer at the depletion region, close to the boundary with MoS<sub>2</sub>. As the build-up of reduced MoS<sub>2</sub> is also expected it is depicted in figures 3.31(c) and 3.31(d) as a reduced acceptor layer of MoS<sub>2</sub><sup>-</sup>, together with the oxidized donor layer of DNTT<sup>+</sup>. The latter is not intended to imply that all molecules are reduced or oxidized in the respective layers of MoS<sub>2</sub> and DNTT; in fact, this is not expected, and it must be understood as a partial redox of the molecules of each side of the heterostructure.

Subfigure 3.31(c) illustrates the decay of the MoS<sub>2</sub> excitons that have remained bound at the monolayer. This interlayer electron-hole recombination happens in a relatively fast lifetime 200 ps. Reciprocally, the dissociated charges that have been transferred across the heterojunction are physically separated, which causes them to recombine at a much slower rate of 2.5 ns, represented in subfigure 3.31(d). This last step of the exciton evolution constitutes the long-lived interlayer charge-separated state, and serves as a further validation of the previous stages of the proposed model, as this long lifetime cannot be explained in a frame where all excitons are bound and remaining in their original layers.

### 3.4.3 Why only in S-het?

Now that the coupling analysis has concluded, one reasonable question is still left unanswered:

*Why all this indications are not obvious in the other heterostrucutures with thicker layers*

of DNTT?

As a matter of fact, there are multiple causes that may intervene in this circumstance, and many of them do not necessarily imply that a thicker layer of DNTT forbids an operational condition of the PN junction. This being said, the possible reasons for not finding obvious indications of an operational PN junction in heterostructures with thicker layers of DNTT are:

1. **Relative contribution in TAS of DNTT<sup>+</sup> is too small compared to the thick DNTT layer.** Probably, the most likely reason for not finding the same evidences at M-het and L-het is that the thick layer of natural DNTT laying on top of the DNTT<sup>+</sup> makes it more difficult to perceive the relative influence of DNTT<sup>+</sup> in the overall TAS signal, as a lower amount of light intensity can photoexcite it.
2. **Pump pulses barely reach the MoS<sub>2</sub> monolayer.** As the MoS<sub>2</sub> layer rests at the bottom of a thick and heavily absorbing layer of DNTT, A and B excitonic transitions are not as efficiently photoactivated by the pump. As a result, the retrieved TA signal from the MoS<sub>2</sub> would be much lower, and the small nuances that could potentially be perceived in this spectral region are harder to resolve. This is, in fact, quite obvious at the TAS of the L-het (in figure 3.21 from section 3.3.2), where the TA signal coming from DNTT is much more pronounced than that of the A and B excitons. However, the backwards measurement presented in figure 3.22(b) proves that, even when exciting the MoS<sub>2</sub> layer first at the M-het, the TAS signal of the M-het does not change significantly nor reveal any of the indications of layer coupling that were explained above. Therefore, the present argument for the lack of indications of layer coupling in M-het and L-het is not compelling.

**3. Thicker DNTT behaves like bulk.** When the bulk thickness of the DNTT nanosheet is increased, the chances of having a highly-ordered crystalline-like layer decrease. A more amorphous DNTT layer would be detrimental to the charge carrier mobility, and the overall behaviour of the material would no longer resemble a semiconductor. In that scenario, there would be no functional P-type semiconductor at the PN junction and the heterostructure would have practically no use.

**4. Impaired photogeneration of the CT exciton in thicker DNTTs.** The comparison of the experimental ESA of various calibres of DNTT (in section 3.3.2), concluded that the Stark effect in the thicker M-DNTT and L-DNTT layers seemed to be reduced, both at the reference layers and at the heterstructures M-het and L-het. This aftermath pointed towards the possibility that the generation of the CT exciton at the thicker layers of DNTT may be impaired. Less amount of excitons with CT character being photogenerated at the DNTT layer of the heterostructure can potentially disrupt the charge transfer across the junction and consequently diminish the working efficiency of the photovoltaic system.

All the aforementioned possibilities could be taking a part on the indistinct proof of a coupled PN junction of heterostructures with thicker DNTT layers. Nevertheless, the results clearly guarantee that the composition of the PN heterojunction with a thinner 15 nm layer of DNTT accomplishes the hypothesised operational quality of the vdW heterojunction and the intended functional photovoltaic effect.

## 3.5 Conclusions

Within this chapter, TAS was employed to spectroscopically characterize the ESA of vdW heterojunctions made of a combination of two thin films: a nanosheet of the organic semiconductor DNTT, intended as the electron-donor P-type semiconductor side, and a monolayer of TMD, precisely MoS<sub>2</sub>, as the acceptor N-type layer of the heterostructure.

The analysis of different combinations of layer calibres concluded that the heterostructured system that can guarantee a good operation of the PN junction with photovoltaic characteristics is the composite of the monolayered MoS<sub>2</sub> with a 15 nm nanosheet of DNTT.

The arguments in favour of the aforementioned verdict were extensively discussed in the previous 3.4 section, and they include the observation of a depletion region being formed at the heterostructure, an interlayer charge transfer with a lifetime of 6 ps and a long-lived 2.5 ns charge-separated state, that is only possible upon dissociation of the photogenerated excitons.

The ultimate consequence of these favourable conclusions entails that the proposed heterojunction is a good candidate for the construction of optoelectronic devices. Precisely, the collaboration partners that designed and synthesised the semiconducting layers fabricated anti-ambipolar phototransistors by the suggested combination of calibres of DNTT nanosheets and MoS<sub>2</sub>. Their observations<sup>9</sup> of a high photoresponsivity of  $R_\lambda \approx 3.2$  A/W are in consonance with the verdicts derived from the presented analysis of the TAS, and encourages the further experimentation with these vdW heterojunctions as the integrated machinery for novel solar cells and ultrafast photodetectors.

---

<sup>9</sup>Measurements performed by Emad Najafidehaghani (*collaborator 1*).

# Chapter 4

## Cavity ring-down transient absorption spectroscopy (CRD-TAS)

### 4.1 Introduction

In the previous chapter, the analysis of the TAS of thin film systems was demonstrated. The measurements of organic nanosheet layers and monolayered semiconductors were successfully performed by a conventional TAS technique, that proved to have enough sensitivity to detect the TA signals even from samples of a thickness below the nm.

The former is a rather extraordinary case, as thin films provide a very short interaction length for pump and probe beams, where often only one or very few layers of molecules are involved in the generation of a TA signal. This (given that the molecular extinction coefficients are not notably high) results in a very low optical density of the probed material or, in other words, an optically thin sample, whose TA signal cannot be easily



sensed with the traditional techniques for time-resolved spectroscopy.

A representative example of this limitation are the semiconducting thin films of  $GeSe_2$ . Literature reports that  $1\ \mu m$ -thick  $GeSe_2$  sheets show a maximum excited state absorption signal of 3 mOD, when excited with  $5\ \mu J$  pulses at 350 nm [126]. Other manufacturers have synthesized few-monolayer flakes of  $GeSe_2$  by CVD with a thickness of only 7 nm [127]. This implies, assuming a linear correlation between thickness and signal intensity, that the characterization of the excited state dynamics of the thinner  $GeSe_2$  flakes requires a methodology that is able to sense at least a 100th of these 3 mOD obtained for the prior thicker  $GeSe_2$  sheets.

As explained in the previous chapter 3, the optical properties of semiconducting materials such as TMDs differ enormously if they are produced in monolayers in comparison to the bulk material. For this reason, the investigation of the exciton dynamics of the mono- and few-layered semiconductor systems is crucial to understand the mechanics of their distinct photoactivated processes, with the ultimate goal of exploiting their properties for the development of innovative semiconducting devices.

With all the aforementioned aspects into consideration, one can foresee the necessity of a time-resolved technique that is able to resolve the TAS of optically thin samples. In the research project described throughout this chapter, a novel technique is proposed to address the challenge by combining two well-established techniques: TAS with cavity ring-down spectroscopy (CRDS), conceiving the new technique baptised as **cavity ring-down transient absorption spectroscopy (CRD-TAS)**. With such design, two additional advantages come forth:

- The absorption path length of the sample is increased by at least two orders of magni-

tude, which will presumably enhance the sensitivity with respect to TAS.

- The noise becomes independent from pulse-to-pulse fluctuations of the laser source, since the rate of absorption is not extracted from the amplitude but instead from the decay (ring-down) of the probe pulse intensity inside the cavity.

#### 4.1.1 Previous research and state of the art

The first report on cavity-enhanced spectroscopic techniques with pulsed lasers was published by A. O’Keefe and D. Deacon. They employed a broadband pulsed laser to measure the absorption bands of atmospheric gasses, achieving a sensitivity in the detection of absorption coefficients as low as  $10^{-8} \text{cm}^{-1}$  [128]. Moreover, their setup design contributed to the precise determination of the spectral reflectivity of mirror coatings, which impelled the advancement of dielectric coating manufacture with custom-designed specifications [129].

The existing literature on CRDS techniques is extensive, and focuses particularly on the detection of low-absorbing or trace gases in controlled environments [130], and in the atmosphere with open-air cavities [131, 132]. The first study that reported the adaptation of the CRDS technique to investigate the steady state absorption of condensed samples was published by Engeln et al., by the identification of the absorption lines of a 20 nm thick  $\text{C}_{60}$  film deposited on a ZnSe window [133]. Afterwards, a handful of reports of the application of CRDS in thin film characterization were reported with Brewster angle geometry, mostly in the infrared range [134–136], and also to study the evolution of the growth of Si:H films [137].

### Addition of the time resolution

The application of CRDS to study reaction kinetics was explored for the first time by T. Yu and M. Lin; in their investigations of the  $C_6H_5 + O_2$  reaction [138] and phenyl radical reactions [139]. The experiment is repeated over time, monitoring the product concentration over time which yielded in a quantitative measurement of the reaction rate. The product and reactant concentrations could be considered constant for each intracavity pulse, as the kinetics of the reaction were much slower than the decay of the pulse inside of the cavity.

There is also literature describing time-resolved cavity ring-down spectroscopy, where the time resolution is achieved by externally pumping the sample with a photolysis beam, allowing the investigation of kinetics of processes in the micro- or millisecond time range in gases and solutions [140, 141].

Moreover, recent investigations demonstrate a method for broadband cavity-enhanced ultrafast spectroscopy with the capacity to resolve short-lived ( $\approx 1$  ps) transients from dilute molecular beams [142]; the broadband quality is achieved by coupling tunable frequency combs into high finesse cavities with dispersion-managed broadband mirrors [143].

Up to the date of the submission of this thesis, the exhaustive literature research did not reveal the existence of a purely pump-probe cavity-enhanced technique with sub-ps resolution for solid thin film samples. Therefore, the present project aims to fill in the existing gap in cavity-enhanced technologies with intrinsic time resolution.

### 4.1.2 Theory of cavity ring-down spectroscopy (CRDS)

#### Properties of an optical cavity

The conventional CRDS constitutes a spectroscopic technique for the sensitive detection of low attenuations. It profits from a multi-pass interaction by means of a resonator or cavity inside which the sample is placed. The properties of the cavity depend on the following factors, that are graphically depicted in figure 4.1.

**Cavity length  $l$ .** The distance between cavity mirrors, that defines the duration of a round trip of a light pulse oscillating inside of the cavity  $t_{rt}$  as:

$$t_{rt} = \frac{2l}{c} \quad (4.1)$$

There are many possible layouts that allow a folded configuration and a longer cavity length, e.g., L-shaped cavities or ring configurations [28]. For simplicity and ease in alignment, a linear cavity is preferred in this case.

**The reflectivity of the cavity mirrors  $R$ .** The cavity mirrors have two surfaces: On the one side, the front surface facing the laser source on which the laser pulses impinge is usually coated with an anti-reflective (AR) dielectric coating. This maximizes the amount of light that can be transmitted inside the cavity. On the other side, the rear surface (facing the inside of the cavity) is coated with a highly reflective (HR) dielectric coating, that is carefully designed to fit the custom-desired reflectivity  $R$ . A higher  $R$  implies more oscillations of the light pulses inside the cavity, and affects the value of the ring-down time  $\tau$ , i.e., the lifetime of the pulses inside the cavity, that is latter introduced in equation (4.6).

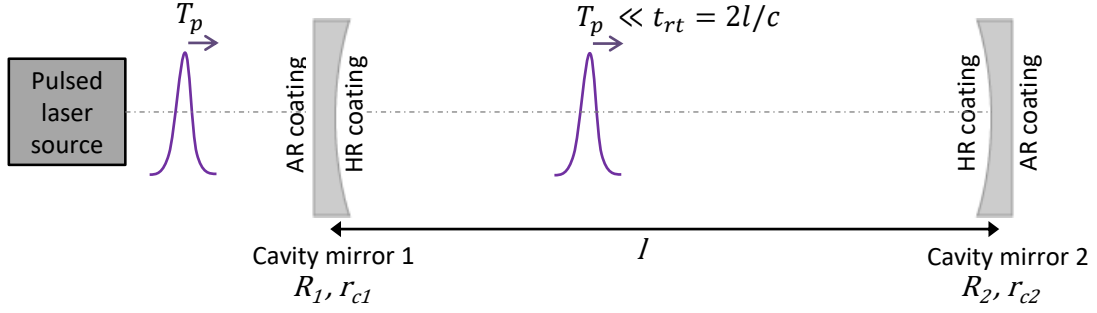


Figure 4.1: Characteristics of a cavity for the design of a cavity-enhanced spectroscopic technique.  $T_p$  corresponds to the pulse duration.

**The radius of curvature of the cavity mirrors  $r_c$ .** The HR-coated surface of the cavity mirror (that faces the inside of the cavity) can be designed as flat ( $r_c = \infty$ ) or curved, usually with a converging surface ( $r_c > 0$ ). This property, together with the length of the cavity, will determine the resonator stability, as explained in detail at the end of this subsection.

### Considerations about the pulse duration versus the cavity length

In general, CRDS can work with a continuous laser source [144] and/or with relatively long pulses [145]. For simplicity, only the theoretical basis of a pulsed CRDS is here explained. Nevertheless, one should be aware of the following main difference between the two frameworks: the *photon bullet model* [145], in which the pulse duration  $T_p$  of the laser source is considerably shorter than the round trip of the pulse inside of the cavity ( $t_{rt}$ ), and the *Etalon* or *Fabry-Perot model* in which the light source is continuous or the pulses are long in comparison to  $t_{rt}$ .

The present case constitutes a clear instance of a *photon bullet model*, as the cavity round-trip time is about four orders of magnitude larger than the pulse duration, i.e.,  $t_{rt} \gg T_p$ . Consequently, the pulse does not last long enough to fold over itself and to self-interfere

[146], there is no generation of a standing wave inside the cavity [147], and therefore the model is not consistent with the idea of a resonator that holds longitudinal cavity modes [128].

On the positive side, this characteristic not only simplifies the theoretical treatment, but also allows to couple any frequency into the cavity, regardless of the cavity spectral range. On the contrary, it also has the drawback of not producing a constructive interference that would induce the standing wave and amplification of the electromagnetic wave [147].

### Retrieval of the sample attenuation

In cavity ring-down techniques, the extinction coefficient  $\bar{\alpha}$  of a sample with thickness  $d$  is retrieved from the detection of the light leaking out of the cavity in which the sample is placed. This transmitted light contains the information of all optical losses  $\mathcal{L}$  that happen inside the cavity, including the transmittance  $T$  of the cavity mirrors with reflectance  $R$ , scattering  $S$ , and absorption by all media inside the cavity  $A$  [144]. Assuming a free-space propagation through air with extinction coefficient  $\bar{\alpha}_0$ , the total absorption  $A$ , including the contributions from the sample and the air in the cavity is given by equation (4.2) as:

$$A = \bar{\alpha}d + \bar{\alpha}_0(l - d) \quad (4.2)$$

The first term in equation (4.2) corresponds to the sample attenuation  $\alpha = \bar{\alpha}d$ . Considering  $T = (1 - R)$  and defining  $\delta$  as the sum of all fixed losses due to scattering and air absorption, one can define  $\mathcal{L}$  by equation (4.3) [145].

$$\mathcal{L} = T + A + S = (1 - R + \bar{\alpha}d + \delta) \quad (4.3)$$

Equation (4.4) describes the temporal decay of the pulses with initial intensity  $I_0$  inside of the cavity, with  $\tau$  being the ring-down time that represents the lifetime of the light oscillating in the cavity. Equation (4.5) reflects a modified Beer-Lambert law, that portrays the intensity of the intracavity light  $I_N$  after  $N$  round trips [148].

$$I(t) = I_0 \exp\left(-\frac{t}{\tau}\right) \quad (4.4)$$

$$I_N = I_0 \exp(-2N\mathcal{L}) \quad (4.5)$$

The typical approach in the derivation of the equation for CRDS measurements is to correlate equation (4.4) with equation (4.5). To finally retrieve the experimentally accessible ring-down time  $\tau$  as shown in equation (4.6), one must also consider  $t$  as the duration of one round trip ( $N=1$ ), as previously defined by  $t_{rt}$  in equation (4.1) .

$$\tau = \frac{l}{c \cdot \mathcal{L}} \quad (4.6)$$

### Gaussian beam propagation

The evolution of the beam profile that propagates in free space is described under the theory of Gaussian beam propagation. This derives from an infinite family of approximate solutions to the wave equation (demonstrated in section 2.1) called the Hermite-Gaussian functions. In the present case of a beam confined in a cavity, the best approximate solutions are alternatively given by Laguerre-Gaussian functions [149]. Generally, all these solutions are referred to as transverse electromagnetic modes ( $\text{TEM}_{ij}$ ), in which the fundamental mode with  $i,j = 0$  constitutes the  $\text{TEM}_{00}$  mode with a Gaussian-shaped transverse electric field distribution [146].

With the purpose of defining the elements of a well-functioning cavity, the relevant parameters of intracavity Gaussian beams are explained and graphically depicted in figure 4.3(a); their corresponding equations can be found on the cited literature [56, 146, 149].

Considering the axial (i.e., longitudinal) coordinate  $\mathbf{r}$  and the radial (i.e. transversal) coordinate  $\mathbf{z}$ , the beam parameters are:

- Size of the beam  $\bar{w}(\mathbf{z})$ : represents the spot size of the beam along the propagation direction  $\mathbf{z}$  by typifying the radius of the beam profile. The smallest radius (focus) in a propagating Gaussian beam is called waist  $\bar{w}_0$ , and establishes the reference axial position  $\mathbf{z} = 0$ .  $\bar{w}_0$  corresponds to half the  $1/e^2$  width, defined as the distance between the two points around the maximum of the intensity distribution that are  $1/e^2 = 0.135$  times the maximum value.
- The wavefront of the Gaussian beam evolves over propagation, changing its radius of curvature  $\bar{R}(\mathbf{z})$ . As depicted in figure 4.2, at the waist position the wavefront is flat yielding in  $\bar{R}(\mathbf{z} = 0) \rightarrow \infty$ . On the right side of the waist position ( $\mathbf{z} > 0$ ) the radius of curvature becomes positive ( $\bar{R}(\mathbf{z} > 0) > 0$ ), denoting a diverging beam.
- Rayleigh length  $\bar{z}_r$  is a measurement of the collimation of a beam, as it represents the distance (from  $\bar{w}_0$ ) necessary for the beam waist  $\bar{w}(\mathbf{z})$  to increase by  $\sqrt{2}$ .



All the aforementioned magnitudes are often expressed in terms of the so-called complex  $q$ -parameter, which simplifies the mathematical treatment of Gaussian beams and allows to perform theoretical analysis of optical cavities under the ray transfer matrix analysis, also known as ABCD-matrix formalism [28, 149].

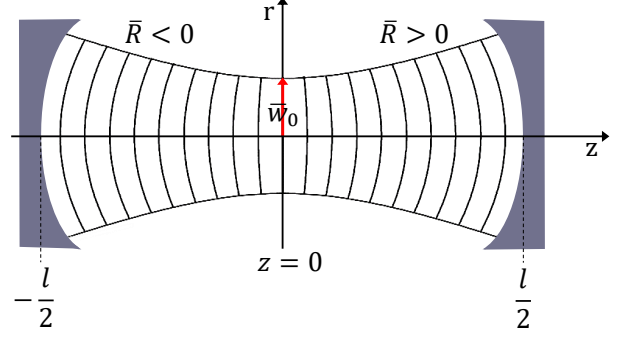


Figure 4.2: Features of the self-reproducing transverse Gaussian modes propagating in a stable cavity.

This framework operates under the paraxial approximation, that assumes small divergence angles (soft focusing) of the Gaussian beams.

**Use.** The ABCD-matrix analysis will be employed in the forthcoming section 4.4 to calculate the theoretical beam waist of the cavity, and compare it to the experimentally measured value. In this manner, the single-mode operation of the cavity is ensured.

### Configuring a stable cavity

The stable propagation of a Gaussian mode inside of a cavity is depicted in figure 4.2. The concept of stable propagation infers not only that the Gaussian beam keeps its profile at any location within the cavity, but also that the width and phase are reproduced identically in every round trip [149]. This self-reproducing pulse propagation happens only for the so-called **transverse resonator modes** which can only be sustained in a cavity when the wavefront of the transverse mode at the cavity mirror position  $\bar{R}(z = \pm l/2)$  is identical to the radius of curvature of the cavity mirrors  $r_c$  [28].

With this additional condition for a cavity-confined Gaussian beam, the rules of what constitutes a stable cavity are derived from the eigenvalues of the ABCD-matrix [150]. As a result of this operation, the stability parameter  $g_i$  described in equation (4.7) is obtained, that must be applied to each of the mirrors (with reflectivity  $R_i$ ) constituting the cavity (of length  $l$ ).

$$g_i = 1 + \frac{l}{R_i} \quad (4.7)$$

Having defined  $g_i$ , the conditions for a two-mirror optical cavity to sustain a stable operation are determined by the following inequality:

$$0 < g_1 \cdot g_2 < 1 \quad (4.8)$$

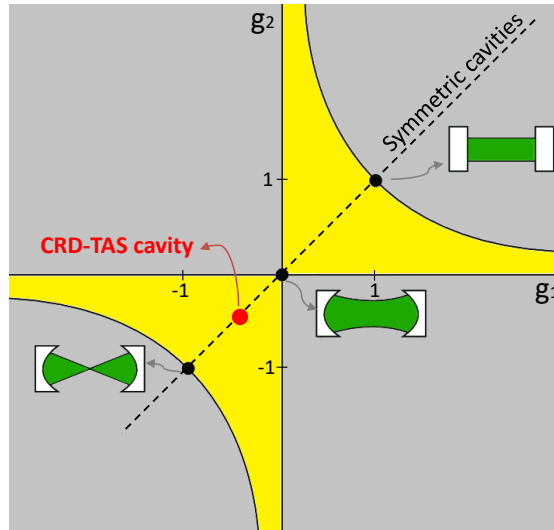


Figure 4.3: Diagram of the stability regions of a cavity design considering the  $g$  values, that depend on the cavity length and curvature of its mirrors.

The allowed solutions of the inequality (4.8) are contained in the highlighted area depicted in figure 4.3, whereas those combinations of  $g$  values upholding an unstable cavity are greyed out.

**Use.** The theoretical definition of a stable cavity provided by the analysis of the  $g$  values allows to design a configuration that is able to uphold a stable operation, removing the uncertainty procured by a trial and error method. By this means, a better decision of the cavity mirrors and length is made. In the present layout design, the selected  $g$  values are  $g_1 = g_2 = -0.4$ , which constitutes a stable symmetrical cavity, with a  $w_0$  waist located at the center. Further details about the specific configuration are given in the following 4.4 section.

### Mode matching

In general, different transverse resonator modes are feasible within the same cavity. Higher-order resonator modes are more lossy, and therefore have their own diminished ring-down times. The technique of mode-matching consists of in-coupling a pulse into the cavity that matches one of the transverse cavity modes, usually the TEM<sub>00</sub> or fundamental Gaussian mode. This configuration supports a low-loss pulse propagation in which the single-mode operation is maintained in the cavity during the entire oscillatory decay of the pulse [145]. Consequently, the ring-down decay can be fitted through the monoexponential temporal evolution described in equation (4.4), and thus, a unique ring-down time  $\tau$  is able to model the lifetime of the single-mode pulse inside of the cavity.

**Use.** Mode-matching is performed experimentally by placing a telescope before the cavity that pairs the size of the collimated beam with an existing transverse resonator mode. As it will be presented in the methodology section 4.4, the combination of mode-matching with an accurate alignment of the in-coupled pulse and the cavity mirrors is crucial for a single-mode stable operation.

### 4.1.3 The novel CRD-TAS technique

The proposed layout of the CRD-TAS technique is very similar to a conventional collinear pump-probe setup, with the difference that the sample is placed in the Brewster angle ( $\approx 56^\circ$  for glass) inside of a cavity, conformed by two highly reflective mirrors. Figure 4.4 depicts a sketched explanation of the CRD-TAS working principle.

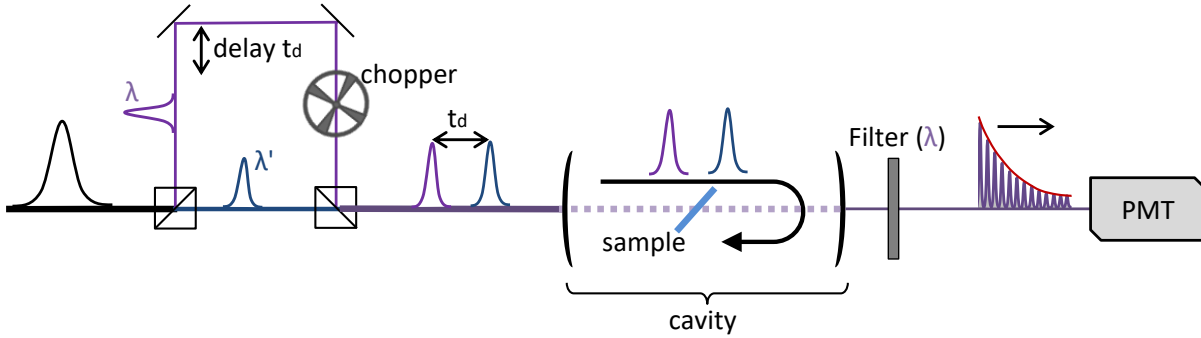


Figure 4.4: Working principle of CRD-TAS. An ultrashort pulse is split into pump (blue) and probe pulse (purple), that are made to have slightly different wavelengths. Probe pulses are temporally delayed ( $t_d$ ) with respect to each other, and are coupled collinearly into the cavity, where the sample is placed at Brewster angle. With a narrowband optical filter in which  $\lambda$  is the central probe wavelength, the pump beam is blocked after the cavity and only the probe ring-down decays are detected with a photomultiplier (PMT).

Identically to TAS, the pump pulse excites the sample and afterwards the probe pulse interacts with it, experiencing the modification in probe transmission generated by the excitation of the pump pulse. This corresponds to a "pumped" condition in which the sample resides in the excited state. Conversely, the transmission of the probe pulse in steady state is measured under "non-pumped" conditions by physically blocking the pump beam from reaching the sample by means of a chopper.

The difference introduced by the presence of the cavity is that this differential transmission accumulates for every round trip of the pulse inside of the cavity, which does not only

increase the interaction length of the light with the optically-thin sample, but also allows to retrieve the differential transmission independently<sup>1</sup> from the resolution of the detection system.

### Timescales involved in CRD-TAS

There are multiple processes involved in the data acquisition and interpretation of a CRD-TAS signal that happen in several time scales.

- (i) The transient processes inherent to the sample under study are photoactivated by the pump pulses and investigated by the probe pulses. These typically range from tens of femtoseconds to few nanoseconds (depending on the sample) and are addressed by the pump-probe delay time  $t_d$  that is experimentally controlled by the movement of a mechanical delay stage.
- (ii) Round-trip time  $t_{rt}$ : The time that the pulses need to travel one full round trip inside of the cavity. The cavity designed for the CRD-TAS is 0.7 m long, and therefore, according to equation (4.1),  $t_{rt} = 4.67$  ns.
- (iii) The ring-down time  $\tau$ : is the measured magnitude in a CRDS setup, and corresponds to the lifetime of the pulse inside of the cavity.  $\tau$  depends on the losses of the cavity and contains the attenuation of the sample inside of it, which can be retrieved through equation (4.6).

As in any TA experiment, the sample should optimally be excited from its vibronic ground state (at the experimental temperature conditions) in each pass of the pump pulses. In the case of the CRD-TAS this implies that the phototriggered processes (timescale (i)) should

---

<sup>1</sup>The detection system must have enough resolution to detect the progressive decrease in signal intensity after every round trip, but does not need to precisely resolve the transmission changes in a single pass regime.

have completely relaxed after half of a cavity round-trip (timescale (ii)), i.e.,  $t_{rt}/2 = 2.34$  ns. This would constitute the maximum lifetime of the transient photoexcitations of the intracavity sample in the current setup design. Nonetheless, this does not intrinsically restrict the applicability of the CRD-TAS technique to short-lived systems, as it depends only on the cavity length and therefore can be extended with larger or folded cavity designs.

### Choice of pump and probe wavelengths

At the present stage of the CRD-TAS setup, the central wavelengths of pump and probe pulses are only separated by a few nanometers. Otherwise, the selection of the Brewster angle for positioning the samples in the cavity would be different for each beam, as it is calculated from the wavelength-dependent<sup>2</sup> refractive index.

Another favourable consequence of choosing similar wavelengths is that pump and probe pulses can be assumed to undergo the same losses in each round trip within the cavity, if oscillating independently. In a more thorough treatment, a varying pump intensity (due to losses inside the cavity), and/or different wavelength-dependent losses of pump and probe pulses could be accounted for. This would result in a more arduous but still analytical equation for fitting the decay times of the pumped and non-pumped cavities [148].

### Interpretation of CRD-TAS signals

In cavity-enhanced techniques, the sample attenuation is retrieved as a function of the cavity ring-down time  $\tau$ . Therefore, the compute of the TA signal in terms of the classical expressions of  $\Delta A$  or  $\Delta T/T$  requires a conversion from the measured magnitude  $\tau$  to a

---

<sup>2</sup>As a consequence of the chromatic dispersion, explained in section 2.1.

differential expression that emphasizes the contrast between pumped and non-pumped cavities, and ultimately allows to compare the signal and noise magnitudes with other time-resolved techniques.

The following discourse is directed towards finding a consistent expression of  $\Delta T/T$  as a function of the pumped ( $\tau_p$ ) and non-pumped ( $\tau_{np}$ ) ring-down times. The reason behind selecting this expression over  $\Delta A$  is that the intrinsic sample absorption cannot be isolated from other sources of sample attenuation (such as scattering or birefringence); moreover, an expression as a function of the transmission offers a more cohesive result as it follows the same tendency (increase or decrease) as the measured  $\tau$ , and will translate into a differential variable of the same sign.

The experimental transient signals are computed as  $\Delta\tau$ , i.e., the difference between the ring-down time of the cavity when the sample is pumped  $\tau_p$  and when it is non-pumped  $\tau_{np}$ . Figure 4.1.3 illustrates the exemplary case of a sample undergoing a photo-induced absorption of the probe pulses: The pump pulse modifies the optical response of the sampled material at the probe frequency causing a higher sample absorption of the probe pulses; consequently, the pumped cavity yields in a shorter ring-down time compared to the non-pumped cavity.

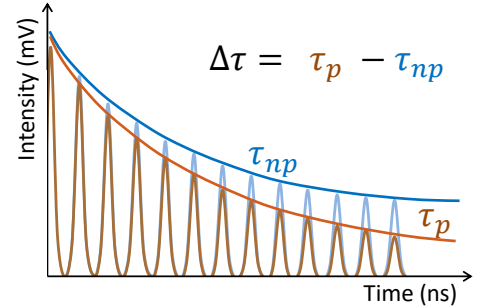


Figure 4.5: Scheme of the ring-down decay of a pumped (brown) and non-pumped (blue) cavity. Every peak under the exponential decay represents a round trip of the pulse in the cavity.

The transmittance of the pumped (non-pumped) sample  $T_p$  ( $T_{np}$ ) is a proportional quan-

tity expressed in terms of the transmitted intensity of the pumped (non-pumped) sample  $I_p$  ( $I_{np}$ ) over the incident intensity of the probe  $I_0$  by:

$$T_p = \frac{I_p}{I_0} \qquad T_{np} = \frac{I_{np}}{I_0} \qquad (4.9)$$

As introduced in the previous section by equation (4.5), the Beer-Lambert law for CRDS can be expressed in terms of  $\tau$  by substituting equation (4.6) into it. This results in equation (4.10) that allows to express  $I_p$  and  $I_{np}$  by:

$$I_p = I_0 \exp \left[ -\frac{2Nl}{c\tau_p} \right] \qquad I_{np} = I_0 \exp \left[ -\frac{2Nl}{c\tau_{np}} \right] \qquad (4.10)$$

Combining equations (4.9) and (4.10) reveals the expression for  $\Delta T/T$  for CRD-TAS signals:

$$\frac{\Delta T}{T} = \exp \left[ 1 - \frac{\tau_{np}}{\tau_p} \right] - 1 \qquad (4.11)$$

The conversion between  $\Delta T/T$  and  $\tau_p$ ,  $\tau_{np}$  provided by equation (4.11) will be utilized to depict the  $\Delta\tau$  signals of CRD-TAS as a function of both magnitudes.



## 4.2 The setup design

This section is dedicated to describe the design of the CRD-TAS technique in detail. For this purpose, the setup layout will be illustrated, alongside the characteristics of the light source, the measuring pulses, and the optics. Moreover, the requirements for the electronic capabilities of the data collecting equipment are specified, to develop into the necessities of the measuring software in the next section.

### 4.2.1 CRD-TAS setup

The final setup design depicted in figure 4.6 required several rounds of troubleshooting until substrates and samples could be properly characterized. The following points describe the setup working at 485 nm wavelenegth (in figure 4.6), in the same order at which the light pulses transmit and/or reflect at every piece of optical equipment, referenced in the text as `typewriter font`.

A laser system consisting of a titanium-sapphire oscillator and chirped pulse amplifier (COHERENT Mantis + Legend) generates ultrashort 85 fs pulses centered at 800 nm with a bandwidth of 14 nm and a repetition rate of 1 kHz. An optical parametric amplifier (OPA: Topas + NirUVis) converts the fundamental wavelength into 485 nm pulses.

A Berek compensator allows to control the light intensity transmitted through a linear polarizer. A `beam splitter` divides the up-converted output into two pulse trains, a `pump` (with 90 % of the total intensity) and a weaker `probe` pulse train. Both beams pass through the same narrow `bandpass filter` (at different angles), which decreases the bandwidth of both pulses and consequently elongates the pulses to 100 fs.

The `probe` beam is transmitted at zero incidence angle through the `bandpass filter`,

resulting in a transmitted pulse spectrally centered at 488 nm. The **pump** beam impinges on the **bandpass filter** at a  $25^\circ$  angle, which shifts the central wavelength to 484 nm. Afterwards the **pump** beam passes through a **chopper** at a frequency of 500 Hz and subsequently enters a 25-mm long, motorized **delay line**.

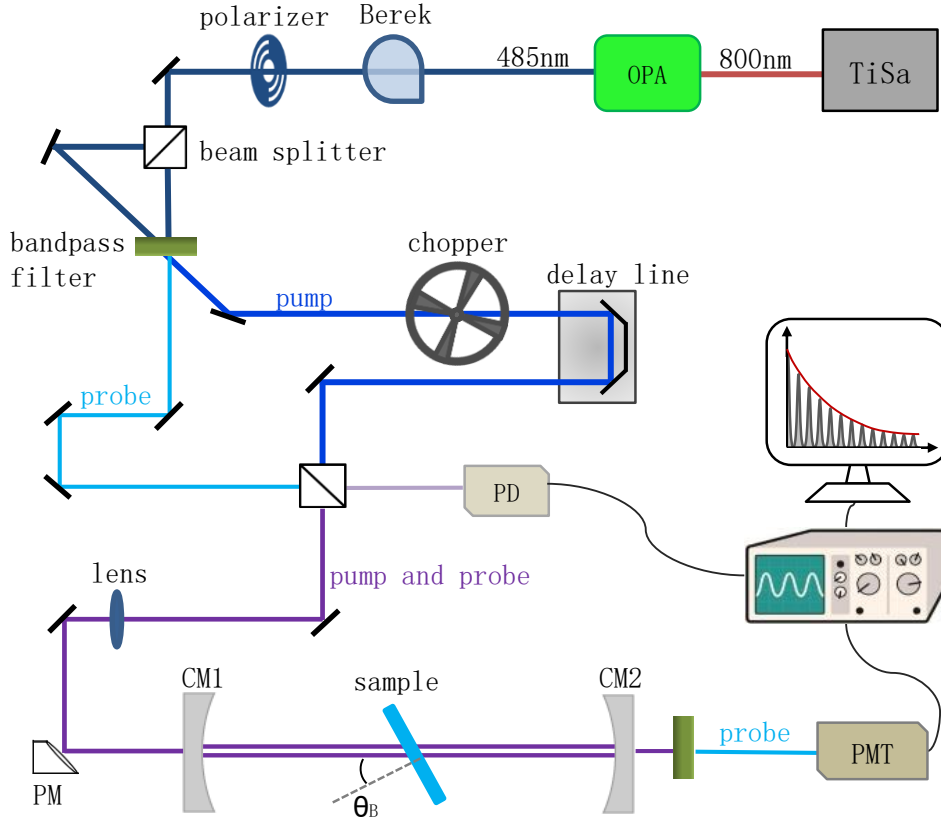


Figure 4.6: Final design of the CRD-TAS measuring setup at 485 nm.

Afterwards, **pump** and **probe** beams are combined by a 50:50 beam splitter and sent towards the cavity collinearly. A sorting photodetector (PD) behind the 50:50 beam splitter allows the software to classify the ring-down traces into pumped and non-pumped measurements.

Before entering the cavity, the pulses pass a mode matching telescope made of a **lens** and a  $90^\circ$  off-axis parabolic mirror (**PM**), that decreases the profile of the beams to 1 mm for a better matching to the  $\text{TEM}_{00}$  mode of the cavity. The linear cavity is comprised of two identical cavity mirrors (**CM1** and **CM2**) which properties are described in the following subsection. Samples are placed inside the cavity under Brewster's angle  $\theta_B$  which, in conjunction with p-polarized **pump** and **probe** pulses, minimizes Fresnel reflections and maximizes transmission through the sample and substrate material. In order to allow a fine tuning of  $\theta_B$  for each sample and substrate with different refractive indices, the sample holder is mounted on a rotational mount.

A small portion of the intensity of both **pump** and **probe** beams is transmitted through the second cavity mirror **CM2**. By placing a second narrow band pass filter (of the same characteristics as the first one), only the **probe** is transmitted and ultimately detected with a photomultiplier (**PMT**, Hamamatsu H6780). The oscilloscope (LeCroy Waverunner 64 Xi) collects the signals from the sorting photodetector and the photomultiplier, and bundles them into multichannel waveforms that are sent to the self-made data analysis software.

### Specific properties of the setups at 485 nm and 800 nm

Both of the measuring setups that were developed to work at different wavelengths (i.e. 485 nm and 800 nm) have an equivalent layout to the one depicted in figure 4.6. The guiding mirrors are protected silver mirrors (Thorlabs) in both setups; conversely, many optics that are custom designed and/or must be wavelength-specific; their different characteristics are compared at the following table 4.1.

Table 4.1: Properties of the wavelength-specific optics of the CRD-TAS setups at 485 nm and 800 nm.

Optics	Property	485 nm	800 nm
<b>Bandpass filter</b>	Central wavelength	488 nm	806 nm
	Bandwidth (FWHM)	3 nm	2 nm
<b>Cavity mirrors</b>	Reflectivity	99.95%	99.995%
	Radius of curvature	500 mm	500 mm
	Group delay dispersion (GDD)	$\leq 10 \text{ fs}^2$	$\leq 50 \text{ fs}^2$

The different parameters in table 4.1 have the following repercussions in the experimental setups:

- The radius of curvature (500 mm) and the distance between cavity mirrors of 0.7 m is the same in both setups, constituting a stable symmetric cavity.
- The dielectric coatings of the cavity mirrors of both setups are designed to have minimal dispersion. However, the cavity mirrors for the 800 nm setup have GDD value that is 5-times more accurate compared to the cavity mirrors for the setup at 485 nm. The reason for this difference is that the first were custom-made about 10 years earlier compared to latter, timespan in which the thin-film coating technology has considerably developed, allowing for a greater accuracy of the coating parameters.
- The choice of distinctive mirror reflectivity was deliberate. In the first stage of the development of the CRD-TAS technique with the setup at 800 nm, the goal was to have as many round trips as possible, which is achieved by maximizing the reflectivity to 99.995 %. However, this comes with a clear drawback: discarding the same proportion of pulse intensity upon entering the cavity. Considering that the number of round trips for the 800 nm setup was large enough ( $\geq 40$ ) for samples with an attenuation of  $\sim 3\%$ , it was regarded as preferable to transmit into the cavity 10 times more optical power.

Consequently, the reflectivity of the 485 nm cavity mirrors was made to have one order of magnitude lower.

The distinctive reflectivity for the cavity mirrors of the setups at 485 nm and 800 nm yields in different values for intracavity powers and ring-down times of the empty cavity, as represented in table 4.2.

Table 4.2: Cavity properties for the CRD-TAS setups at 485 nm and 800 nm.

	485 nm (R = 99.95%)		800 nm (R = 99.995%)	
<b>Ring-down time of empty cavity (<math>\mu\text{s}</math>)</b>	4		7	
<b>Intracavity pulse energy (nJ)</b>	<b>pump</b> 2	<b>probe</b> 0.2	<b>pump</b> 0.5	<b>probe</b> 0.1

### 4.2.2 Electronic equipment

A careful election of electronic equipment has to be made to resolve the fast oscillating signals of the ring-down decay with high resolution. Although this decision was made by Dr. Wolfgang Paa, it is pertinent to elucidate the importance of this characteristics within this thesis, as the understanding of the requirements is indispensable for assuring the retrieval of profitable data. The (self-made) selection of a chopper, a delay stage and photodetector for sorting will not be further discussed as it is not so critical, since the habitual equipment with common specifications serves its purpose.

Using a photodetection system (photomultiplier and oscilloscope) with high sensitivity and sampling rate is of utmost importance, as each of the outcoupled intensities of the probe pulse after every cavity round trip needs to be resolved with precision and with enough data points. Hereby, the crucial properties of the photomultiplier for probe detection and the data-collecting oscilloscope are discussed.

### Oscilloscope

The use of a fast oscilloscope is a prerequisite, as CRD-TAS measurements demand the precise identification the peak intensity of each round trip of the probe pulse, in order to accurately fit the decay time. For this reason, we employ the oscilloscope *LeCroy Waverunner 64 Xi* with a 600 MHz **bandwidth** and a 5 GS/s **sampling rate** (when using three channels) [151].

**Bandwidth.** The bandwidth of an oscilloscope is defined as the maximum frequency that can be measured while keeping the relative error in the amplitude below 30%. The fastest oscillating signal in the CRD-TAS measurements corresponds to one round trip  $t_{rt}$  with a frequency of:

$$\frac{1}{t_{rt}} = \left( \frac{2L}{c} \right)^{-1} \approx (4.67ns)^{-1} \approx 214 MHz \quad (4.12)$$

As the fastest measured frequency (214 MHz) is below half of the oscilloscope's bandwidth (600 MHz), it is granted that the selected oscilloscope has a sufficiently high bandwidth to resolve the probe pulse amplitudes of the cavity round trips accurately.

**Sampling rate.** In addition to the accurate amplitude determination provided by the bandwidth, one needs to make sure that there are also enough data points taken over time.

This is determined by the sampling rate, defining the speed at which the oscilloscope is inquiring the photomultiplier for a new data point. With a sampling rate of 5 Giga samples per second (GS/s), the oscilloscope acquires a data point once every 0.2 ns, which allows to resolve a probe pulse round trip with about 20 points, as represented by the experimental ring-down close-up of figure 4.7.

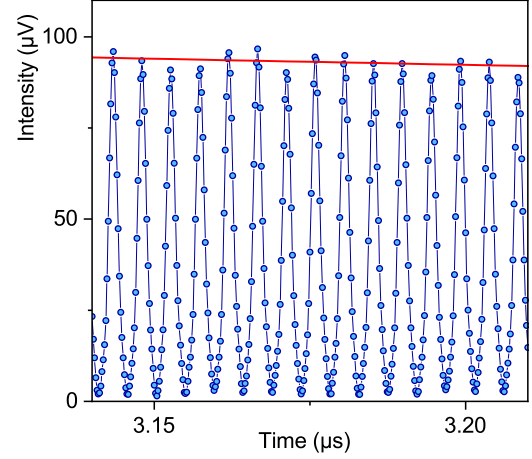


Figure 4.7: Close-up of the data points (blue dots) measured by the photodetection system. The red line represents the exponentially decaying envelope.

### Photomultiplier

The photomultiplier selected for the sensitive detection of the cavity-outcoupled probe pulses is a *Hamamatsu H6780*, with a peak radiant **sensitivity** of  $4 \cdot 10^4$  A/W and a **rise time** of 0.78 ns [152]. The gain of the photomultiplier for CRD-TAS measurements is tuned to relatively low gains (0.25 V to 0.5 V, depending on the wavelength and optical powers achieved), as a higher gain also increases the noise level unnecessarily, and can saturate the response of the detection system.

**Sensitivity.** The probe pulse transmitted through the second cavity mirror has a maximum pulse energy after the first round trip of only 0.1 pJ. Yet, the photomultiplier must have the capacity to detect instantaneous powers that are far below this value, as the interest is to trace the oscillating probe intensities over the pulse round trip inside the cavity (as represented in figure 4.7). The selected photomultiplier has the capability of detecting light intensities  $10^5$  times lower than semiconductor photodiodes [152].

**Rise time.** Considering that the experimental pulse durations are in the order of few hundreds of femtoseconds, there is no photodetector fast enough to resolve the intensity profile of the pulse. This is a universal limitation in ultrafast pulse detection, but it does not restrain the capabilities of the CRD-TAS technique. It is important that the rise time (i.e., reaction time) of the detector is short enough to detect a signal change between two consecutive sampling inquiries of the oscilloscope, so it can reproduce the full round trip of the intracavity oscillating pulse.

With a rise time of 0.78 ns, the photomultiplier is slower than the sampling rate of the oscilloscope, leading to a delayed detection response with respect to the arrival of the pulse at the photomultiplier. However this is not an issue, as this delay is consistent through the experiment and it does not hinder the accurate sampling of the intracavity pulse round trips, as proven by figure 4.7.



### 4.3 The software

The novel CRD-TAS setup requires the development of an operating system that is able to compute the  $\Delta\tau$  signal from the waveforms collected at oscilloscope, and display the calculated  $\Delta\tau$  live. In view of achieving high-quality and user-friendly interfaces with integrated subroutines, all the measuring softwares are developed in Labview (NI Instruments).

Hereunder, the different versions of the software are described. The core unit of the measuring software was self-made, although assistance was provided with the initialization of the devices and the final optimization for computing efficiency, as it will be stated at the specific stages of the software development.

#### 4.3.1 The CRDS software

The program to measure the steady state CRDS is intended to retrieve the ring-down times of the cavity after averaging multiple ring-down decays, with the option to save various sets of data in different files. The user interface and an example measurement are depicted in figure 4.8.

The input parameters selected by the user are:

**Artifact points to dismiss.** At the very beginning of the ring-down decay, there is a signal artifact created by the interaction of the magnetic field of the Pockels cells of the laser source with the photomultiplier circuitry. Although this noise is greatly reduced by using a double-coated coaxial BNC cable (that connects the photomultiplier with the oscilloscope), the signal of the few first round trips is still affected by it. For this reason, it is wise to remove the first 30 to 50 round trips for the exponential fitting and the retrieval

of an accurate ring-down time.

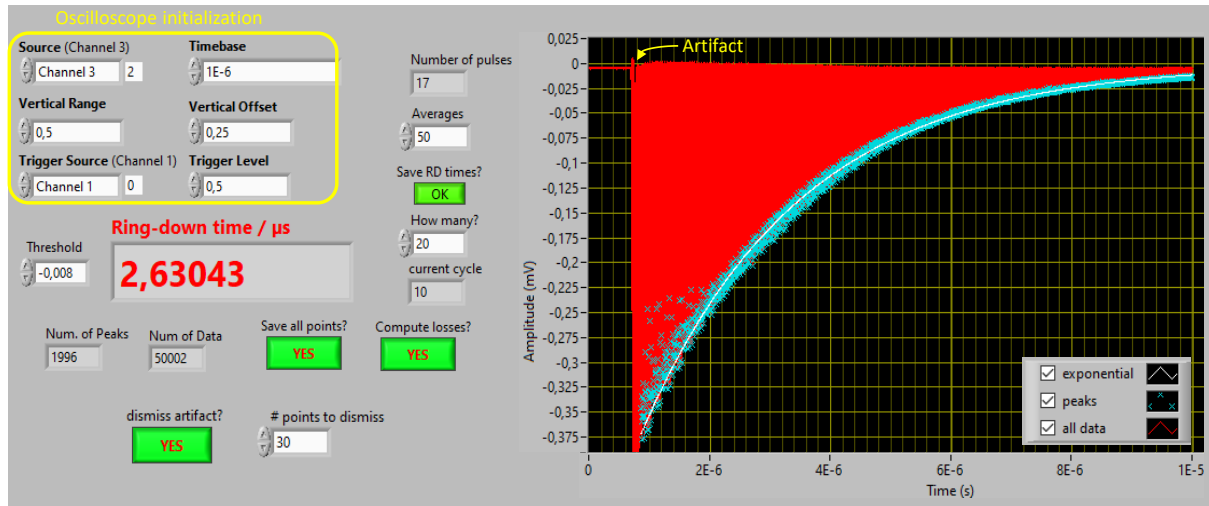


Figure 4.8: User interface of the software made for steady state CRDS measurements.

**Saving.** The user can choose how much data is saved. For a thorough data collection, all data points of all waveforms can be saved in individual files, by clicking "Save all points?" button of figure 4.8. The option "Save RD times" allows for a more memory-economic data record, saving only the individual ring-down times in a file. With the "Compute losses?" option on, one can generate an extra file with the losses related to the ring-down times, computed through equation (4.3) from section 4.1.2. When all these options are deactivated, the results are only displayed but not saved.

**Threshold.** Tells the peak finding subroutine the threshold value above which minima are to be found.

**Loop counter.** The control button "How many?" tells the software the number of iterations to repeat the aforementioned process. This allows to save every measured ring-down time in a new entry of an array, and save the data for post-measurement statistical treatment.

The commands and processes of the software are cued in the following order:

1. All the devices are initialized. The relevant device is the oscilloscope, reading the signal collected by the photomultiplier. However, the delay stage that will be used for the CRD-TAS is also tested and initialized. Subsequently, the user-selected parameters are sent to the oscilloscope to set up the data acquisition. These steps were completed by Dr. Wolfgang Paa, together with the stopping and closing process.
2. The software retrieves from the oscilloscope as many waveforms (i.e. ring-down decays) as the user has specified in the "**Averages**" control value of figure 4.8. The instantaneous number of laser pulses that have been collected is displayed in "**Number of pulses**".
3. The software averages all those data points (red lines in figure 4.8) contained in the waveforms of every collected pulse.
4. After removing the points of the artifact region, the program utilizes the built-in *Peak Detector* subroutine<sup>3</sup> to find the minima of the the data points, displayed in blue crosses in figure 4.8. These peaks represent the maximum amplitude measured at the photomultiplier, and it is the only data necessary to fit the exponential function from which the ring-down times are computed.
5. The built-in *Exponential Fit* subroutine uses the least squares method to fit the minima (blue crosses in figure 4.8) to an exponential decay curve. From this point, the ring-down time is retrieved, saved in an array, and displayed on the interface screen.
6. All the aforementioned processes are enclosed in a loop that repeats as many times as the user defines in the control "**How many?**". After reaching this number of iterations, the program saves the files with the data (if the user has the saving options on) not

---

<sup>3</sup>Finds peaks by fitting a quadratic polynomial to sequential data points.

before asking for the location and the name of the file.

Aside from the data saved in files, the output indicators displayed on the screen during the measurement are: the full set of points defining the ring-down waveform (averaged for multiple pulses), the position of the peaks, and the ring-down times computed from these averaged peak positions. Moreover, the program gives information on the total number of data points collected from the photomultiplier ("Num of Data" in figure 4.8), and the number of peaks ("Num of Peaks") retrieved by the *Peak Detector* subroutine.

### Aid for cavity alignment

As explained in the theory of pulse propagation in optical cavities (section 4.1), the best operation of a cavity fosters a stable propagation of the fundamental transverse mode  $TEM_{00}$ ; additionally, this fundamental mode has a Gaussian beam profile, and a pulse that propagates in this regime will have the longest ring-down time, compared to higher order modes.

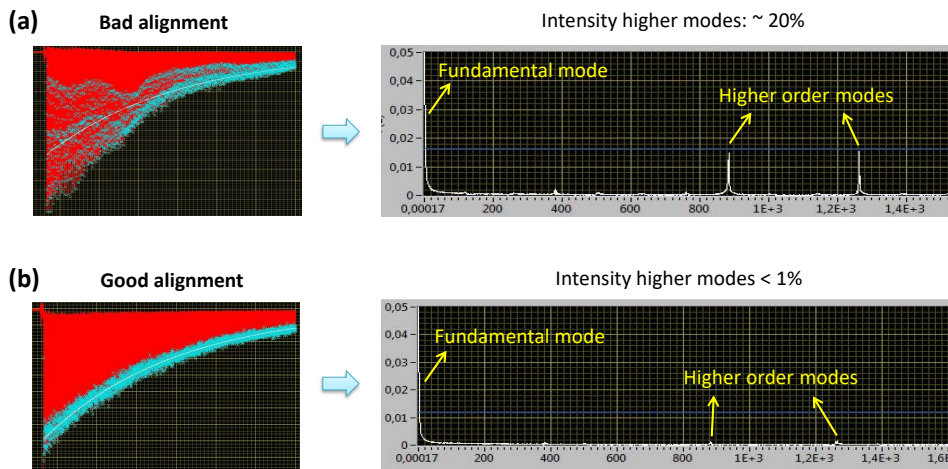


Figure 4.9: Add-on for better cavity alignments using a Fourier-transform analysis of higher order modes.

For this reason, the interest is to optimize the cavity alignment so it can foster the stable operation in  $\text{TEM}_{00}$ , process that can be aided with a Fourier transform analysis of the ring-down waveform. This evaluation reveals how many frequencies (and thus decay rates) are found in the ring-down data and their corresponding amplitudes. The interface of this evaluation software is depicted in figure 4.9.

Once the Fourier analysis is completed, the higher frequencies (i.e. higher cavity modes) can be filtered out with a digital long-pass filter. One possibility is to use this technique to remove all fast oscillations given by the round trips. This process was found to slow down the computing time of the software<sup>4</sup>, without a clear improvement on the noise level of the final signals. For this reason, a long-pass filter was not used for the recording of the data, and only the first strategy in the minimization of the intensities of higher order modes was employed for cavity alignments.

### 4.3.2 The CRD-TAS software

In addition to the routine described before, the measurement of the CRD-TAS signal requires that the data retrieving software accounts for the acquisitions of ring-down times at different positions of the delay stage. Moreover, it must have the capability to calculate the  $\Delta\tau$  signal and display it on the screen in simultaneity with the data acquisition, which demands for a quick processing of the all the tasks queued in the software. To this end, Alexandre Guilbault<sup>5</sup> adapted the routine into a *Producer-Consumer Loop* with a computational efficiency that enables recording measurements two to three times faster, compared with the more simplified timed synchronisation of the software processes.

---

<sup>4</sup>20% to 30% slower depending on the number of total points of the waveform.

<sup>5</sup>QSciTech, Sherbrooke University

### Reading and sending the data to the software

For the CRD-TAS data retrieval, three channels of the oscilloscope are used; the reading of these three signals at the oscilloscope is represented in figure 4.10. **Channel 1** is connected to the trigger signal of the laser source; **channel 2** connects with the chopped pump pulses collected at the photodiode, which are used by the software to sort and classify the ring-down times into pump-on and pump-off; **channel 3** is the cavity ring-down signal collected by the photomultiplier, that detects the probe pulses transmitted through the second cavity mirror after each round trip in the cavity.

The transfer of data from the oscilloscope to the measuring computer is the slowest process of the CRD-TAS software. To optimize it for a quick performance, three further actions are taken:

1. The reading of the pump in **channel 2** is set to switch mode, so it only sends to the software one data point per pulse from **channel 2**.
2. The oscilloscope is set into multiple sequence acquisition mode. This means that, instead of sending the data to the software after each pulse, the oscilloscope accumulates a sequence of maximum 100 pulses and sends them to the measuring computer as a bundle. The amount of pulses in the bundle is user-defined, controlled by the button "Number of Pulses" of the program interface depicted in figure 4.11.
3. As the timespan between pulses (1 ms) is much longer than the ring-down decay ( $\leq 10 \mu s$ ), there is no data contained the oscilloscope after the latter time. For this reason, all data after the first  $10 \mu s$  is discarded at the oscilloscope, which concatenates the multiple sequences by using only the first  $100 \mu s$  of each.

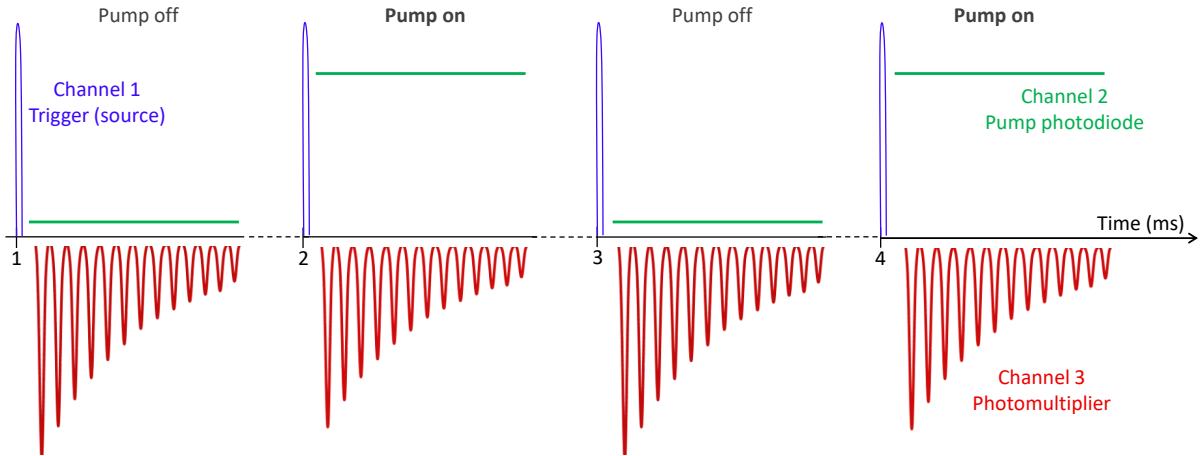


Figure 4.10: Readout of the three channels of the oscilloscope. The bundled sequence is an example of the data package sent to the computer when "Number of Pulses" is set to 4.

### Data sorting

The interface of the CRD-TAS measuring software is shown in figure 4.11. It contains the algorithm for CRDS measurements as a subroutine, utilizing it iteratively to calculate the ring-down times of the pumped and non-pumped cavity, as displayed in the indicators "Pumped Mean ( $\mu s$ )" and "Unpumped Mean ( $\mu s$ )" in figure 4.11, respectively.

However, before the ring-down time is calculated, the program needs to properly sort the ring-down measurements into pumped and non-pumped. For this purpose, the data point that the software receives from the oscilloscope's **channel 2** is compared to a user-defined "pump threshold (V)" value, to be selected at the interface of the CRD-TAS software depicted in figure 4.11. If the retrieved data point from **channel 2** lays below (above) the threshold, the software classifies the simultaneously-recorded ring-down signal as non-pumped (pumped).

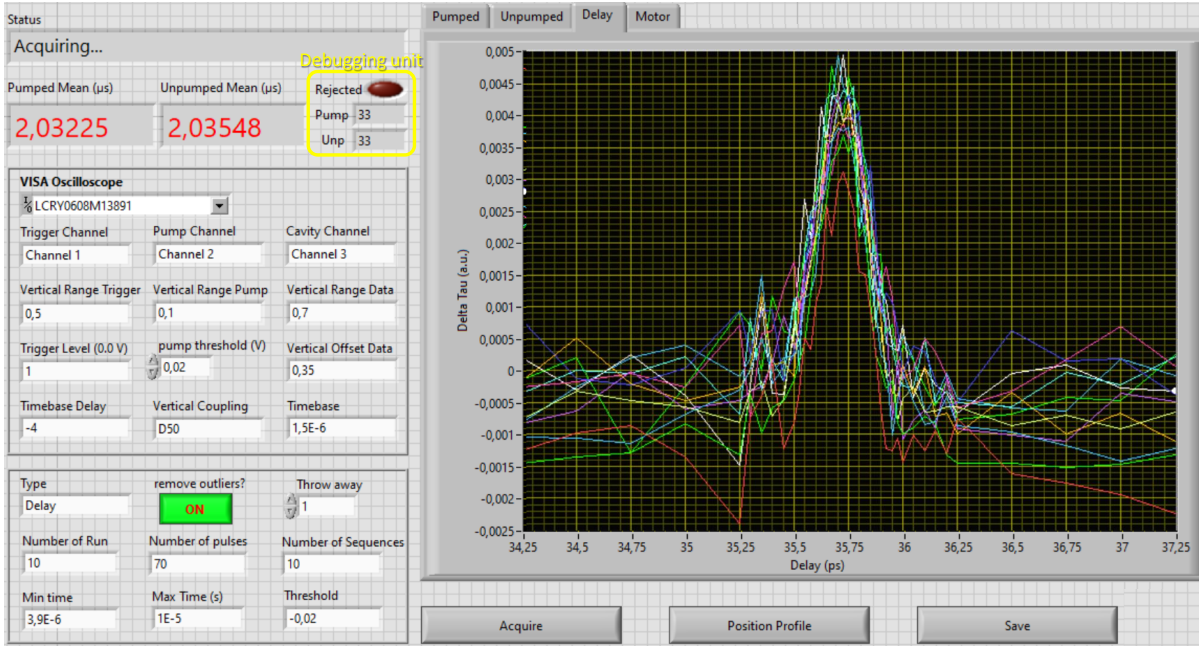


Figure 4.11: User interface of the software for CRD-TAS measurements, showing an example of a  $\Delta\tau$  signal acquisition at the "Delay" tab. The different superimposed lines correspond to multiple scans, that are averaged in signal post-processing.

Furthermore, the software is provided with a debugging unit that displays the number of pumped and non-pumped pulses, and rejects the sequence retrieved by the oscilloscope if these numerical indicators differ by more than two. This mechanism of discarding unevenly-chopped data sequences helps ensuring the quality of the datasets with the additional benefit of pausing the measurement in the case of recurrent beam deviations in intensity or alignment. After the sequence is accepted by the debugging unit, the software chops the sequence into individual pulses and classifies them into pump-off and pump-on measurements. Subsequently, the average is taken from each group and the ring-down times of the pumped and non-pumped pulses are retrieved by the same algorithm described in section 4.3.1. The last calculation consists of retrieving the CRD-TAS signal ( $\Delta\tau$ ) as defined by equation (4.11).



### Other input variables and software options

Additionally to those explained in the last section, the extra options and the new user-controlled parameters are:

**Outlier removal.** The button "remove outliers?" activates a subroutine that discards pulses with data points that are out of range, from each sequence sent by the oscilloscope. Once the pumped and non-pumped pulses are sorted, the *outlier removal* subroutine compares all data points in the waveforms and discards those with the highest and lowest laying values. The number of waveforms that are discarded is two times the value specified in "Throw away".

**Tabs.** The measured data and the current position of the delay stage can be viewed alternatively when navigating the four tabs on the top center of figure 4.11. In the first two tabs "Pumped" and "Unpumped" the ring-down decays and the fitted exponentials of pump-on and pump-off cavities can be viewed, respectively, in the same way as in the previous CRDS software in figure 4.8. The tab "Delay" that is active in figure 4.11 displays the CRD-TAS signal  $\Delta\tau$  for each individual scan.

**Type of acquisition.** To start a measurement the button "Acquire" must be clicked. In the drop-down button "Type" the user can choose among three options for data acquisition: "Single" will take only one sequence of waveforms from the oscilloscope and display the averaged ring-down decays at the "Pumped" and "Unpumped" tabs; "Continuous" repeats the latter in a loop; the "Delay" option records the CRD-TAS signal by repeating the loop at different positions of the delay stage. Within the "Delay" mode for data acquisition, the user must have previously specified the delay positions (i.e., time sheet) by clicking the button "Position Profile". Here, the steps and positions of the delay stage can be defined manually or uploaded from a text file.

**Averaging more data.** Once the software has computed  $\Delta\tau$  for each sequence of pulses, the user can choose to average several  $\Delta\tau$  measurements for every position of the delay line in "Number of Sequences". A reasonable value to select is 8 to 12 sequences; this will amount to a measuring time per point of 2 to 4 minutes, depending on the amount of data points in the ring-down decay. Moreover, the whole  $\Delta\tau(t_d)$  measurement over the different delay stage positions can be repeated as many times as defined by the "Number of Run" control value. The software writes a new *array* for every scan, and generates different traces at the "Delay" tab that superimpose for every iteration (or "Run"), as depicted by figure 4.8, where each trace corresponds to one scan.

**Saving.** Clicking the button "Save" over the course of a measurement saves all the data written in the aforementioned *arrays* in a new text file.

## 4.4 Methodology

The purpose of this section is to describe the methodology used to test the functionality of the novel CRD-TAS technique. The characterization process was done in an iterative manner, as achieving an accurate, time-efficient and reproducible set of results required several revisions on the layout design, along with changes in optics and the data acquisition software. In view of providing a simple and orderly description of the technique development, only the final setup layout that aided in the correct characterization of the CRD-TAS results are hereby described.

### 4.4.1 First steps: Characterization of the light

#### Intracavity beam profile

The beam profile at the center of the cavity is measured to obtain information about the transversal mode propagating in the cavity, and determine the spot size at the sample position.

In order to measure the profile of the cavity mode one must avoid interrupting the intracavity propagation of the beam; therefore, the camera of the beam profiler cannot be located inside of the cavity, as that would measure uniquely the beam profile of the input beam before the first round trip.

For this reason, the profile of the propagating intracavity pulse is measured in an indirect way by placing a transparent substrate at the center of the cavity, in an angle that is close (but not equal) to the Brewster angle. This allows to detect the weakly reflected pump and probe pulses with the beam profiler (Beam profiling camera, Ophir Optonics) outside of the cavity, in an arrangement that is as close as possible to the actual measuring

condition.

Figure 4.12 shows the beam profiles of the intracavity pump and probe beams at the sample position. The software provided with the commercial beam profiler calculates the  $D4\sigma$  values for the horizontal and vertical axis separately. As represented in figure 4.12, both pump and probe beams have an appearance similar to a  $TEM_{00}$  beam with a diameter of  $\simeq 528 \mu m$  and  $\simeq 505 \mu m$  respectively, and a slight uneven diagonal distribution.

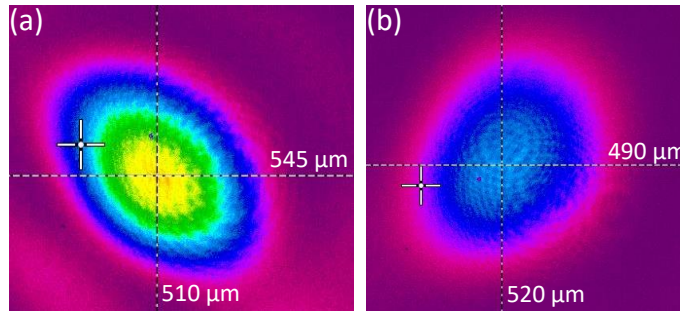


Figure 4.12: Beam profiles of the (a) pump and (b) probe of the 800 nm setup.

**Beam waist predicted by ABCD matrix calculations.** A further step to guarantee that the intracavity beam propagates in  $TEM_{00}$  mode is performed by comparing the experimentally-acquired value with the theoretical calculations of the waist of the Gaussian beam. This is realized through the ABCD-matrix analysis provided with the *WinLASE* software. The experimental parameters introduced in the software for the waist calculation are: the radius of curvature, the length of the cavity, and the diameter of the input beam (1 mm). With this specifications, the ABCD-matrix calculation reveals a beam waist diameter ( $1/e^2$ ) of the  $TEM_{00}$  mode of  $\omega = 487.4 \mu m$ , which applies for both setups at 485 nm and 800 nm as it is not wavelength-dependent.

As the calculated  $1/e^2$  beam diameter is very similar to the measured  $D4\sigma$  value, the pump and probe intracavity beams are considered to propagate in the cavity in the fundamental

TEM<sub>00</sub> mode.

### Pulse duration

As the pump and probe pulses are spectrally filtered before entering the cavity, their pulse duration differs from the laser's output value and needs to be monitored before entering the cavity. Different methods are used for the characterization of the pulse duration in each setup:

1. **Setup at 800 nm.** The pulse duration is measured via autocorrelation of the pump pulses. After converting the measured FWHM, the pulse duration equals  $500 \pm 50$  fs.
2. **Setup at 485 nm.** The duration of the pulses is established through the measurements of the intracavity coherent artifacts generated in thin fused silica substrates [19], resulting in measured pulse durations of  $100 \pm 10$  fs. The methodology of these measurements and their results are presented in later sections.

### 4.4.2 CRDS measurements

The steady state CRDS setup was characterized at 800 nm by measuring the attenuation provided by gold nanodiscs differently spaced on quartz (JGS3) substrates. As represented in figure 4.13, the various nanodisc spacings provide different values of the overall sample attenuation: a wider spacing between nanodiscs yields in a denser packing of nanodiscs per unit area, increasing the global attenuation of the sample.

This characteristic allows to measure different ranges of ring-down times at the steady-state CRDS setup, serving as a first step in the characterization of the technique, as it assesses the systems' ability to detect small changes in sample attenuation.

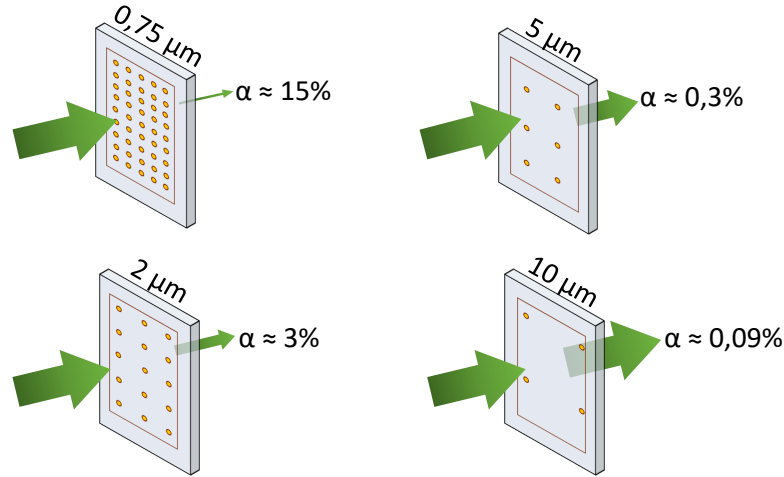


Figure 4.13: Representation of the various nanodisc spacings (in  $\mu m$ ) and its correlation with the attenuation  $\alpha$  of the overall sample. The samples on the right have an attenuation that is high enough to be resolved in commercial UV-Vis spectrometers; the ones on the left have a low attenuation that can only be resolved within the CRDS setup.

Additionally, the attenuation measurements obtained in CRDS are compared to the attenuations retrieved from a commercial UV-Vis spectrometer (Perkin Elmer Lambda 900), which is only possible for samples with an attenuation above 3% due to a limited sensitivity of the spectrometer. In this manner, the dependency of the attenuation on the nanodisc spacing retrieved by the CRDS setup can be verified with a well-established equipment.

The gold nanodiscs have a diameter of  $175 \pm 10$  nm, and a height (or thickness) of  $\approx 30$  nm; the nanodiscs are disposed onto the substrate (covering only half of it) with lithographic techniques by the group of Dr. Uwe Hübner in the *Leibniz-Institute of Photonic Technology (IPHT)*. The same group provided the microscope images depicted in figure 4.14, that show the gold nanodiscs disposed at the nodes of a square grid, whose lateral length corresponds to the nanodiscs spacing, from now on named "period".

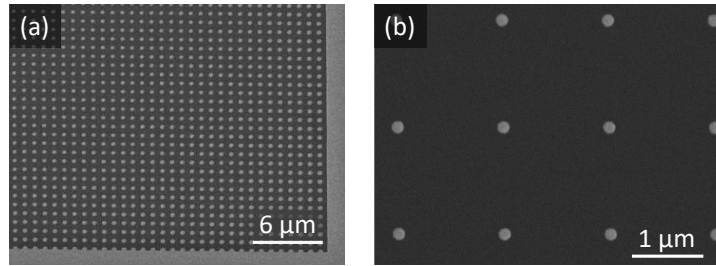


Figure 4.14: Scanning electron microscopy images of the gold nanodiscs samples with spacings (or periods): (a)  $0.75\ \mu\text{m}$  and  $1.5\ \mu\text{m}$ . Obtained from Dr. Hübner's group.

### 4.4.3 CRD-TAS measurements

#### Coherent artifacts at 485 nm

The novel CRD-TAS technique was first characterized through the measurement of coherent artifacts at 485 nm, alongside the comparison of the experimental results with simulations of the physical nonlinear effects contributing to this signal, which are modelled with *Wolfram Mathematica*.

With the purpose of analysing a range of artifacts with different signal shapes, three distinct substrates with different impurity content were utilized. The hypothesis is that XPM is equally present in all types of fused silica, but only those substrates with an increased amount of impurities will display a notable contribution of TPA.

For this reason, the experiment would not be so informative at 800 nm, as there is no expected contribution from TPA in the visible range, implying that the coherent artifact would have the exact same appearance for any substrate composition.

#### Sample measurements at 485 nm and 800 nm

The sample used for attesting the capabilities of the CRD-TAS setup to resolve excited state dynamics of thin films is monolayered graphene. These test samples were manu-

factured externally by the group of Molecular Nanotechnology headed by Prof. Andrey Turchanin in the *Friedrich Schiller University Jena*. They used the technique of CVD to deposit monolayers of graphene on thin fused silica substrates (UVFS from Thorlabs).



## 4.5 Results

In this section, the results that aided on the characterization of the CRD-TAS technique are represented.

### 4.5.1 CRDS results

The capabilities and resolution of the steady state CRDS system at 800 nm are hereby determined. With this aim, several sets of gold nanodisc samples with different amounts of nanodiscs per unit area are measured. The quantity determining the density (or packing) of nanodiscs is the "period", which defines the distance between nanodiscs and alters the attenuation of the global sample. In table 4.3, the various periods considered for the attenuation measurements are disclosed, along with the information about what technique was used to measure its attenuation. The limited sensitivity of the UV-Vis spectrometer cannot resolve the difference in attenuation (compared to a bare substrate) provided by the few illuminated nanodiscs of the (less densely packed) samples with a period below  $2\ \mu m$ .

Table 4.3: Range of periods and technique used to characterize the sample attenuation.

Period ( $\mu m$ )	Technique
0.75	UV-Vis
1	
1.5	
2	
3.5	CRDS
4	
5	
6	
8	
10	

Conversely, the CRDS system at 800 nm cannot work with periods above  $2\ \mu\text{m}$  as the attenuation becomes too high to allow the intracavity pulses perform enough round trips ( $\leq 40$ ) to confidently fit the ring-down decay and extract the losses provided by the cavity.

### UV-Vis

The results of measuring the range of samples with short periods (from  $0.75\ \mu\text{m}$  to  $2\ \mu\text{m}$ ) in the commercial UV-Vis spectrometer are displayed in figure 4.15. Figure 4.15(a) represents the transmission spectra of the different periods, that display a broadband transmission minima centered at 800 nm, being more pronounced for shorter periods.

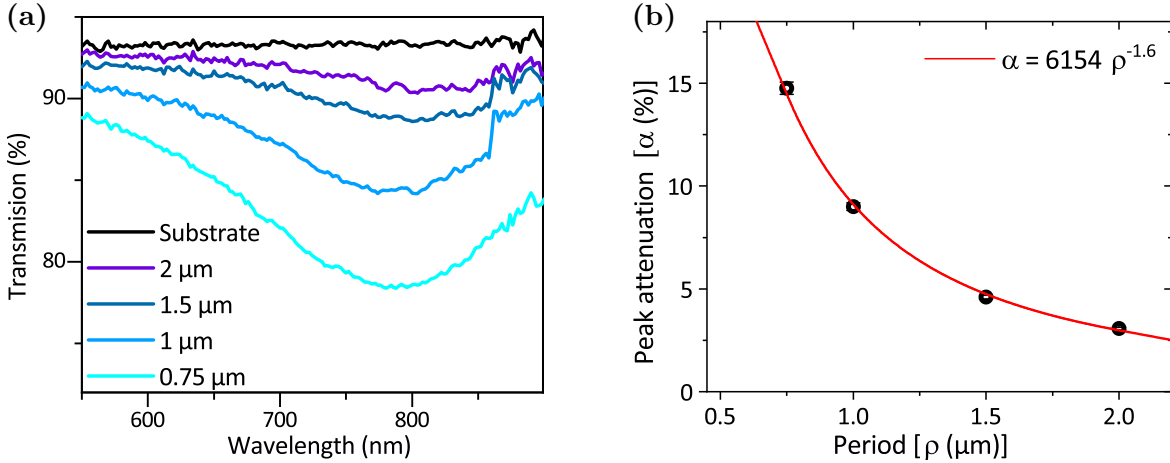


Figure 4.15: Transmission measurements of the gold nanodiscs with short periods; (a) displays the spectral data collected by the UV-Vis spectrometer; (b) depicts the peak attenuation at 800 nm as function of the period (derived from the same dataset as (a)).

Figure 4.15(b) shows the peak attenuation at 800 nm (calculated from the same data set depicted in 4.15(a)), as a function of the period. This calculation is performed by subtracting the transmission of each sample at 800 nm from the substrate transmission at the same wavelength, resulting in the attenuation provided only by the gold nanodiscs. The fit demonstrates that the attenuation is a power function of the period with exponent  $-1.61 \pm 0.05$ .

## CRDS

The CRDS measurements of several gold nanodiscs samples of each period are represented in figures 4.17(a) to (f). Each of the columns in the subfigures represents an average of six measurements of the same sample, from which the error bar is calculated. The full height of one column corresponds to the losses of the whole cavity, calculated according to equation (4.3) of section 4.1.2. The coloured areas of each column indicate the different contributions to the cavity losses, when the sample is placed inside: the **empty cavity**, the **substrate** and the **gold nanodiscs**.

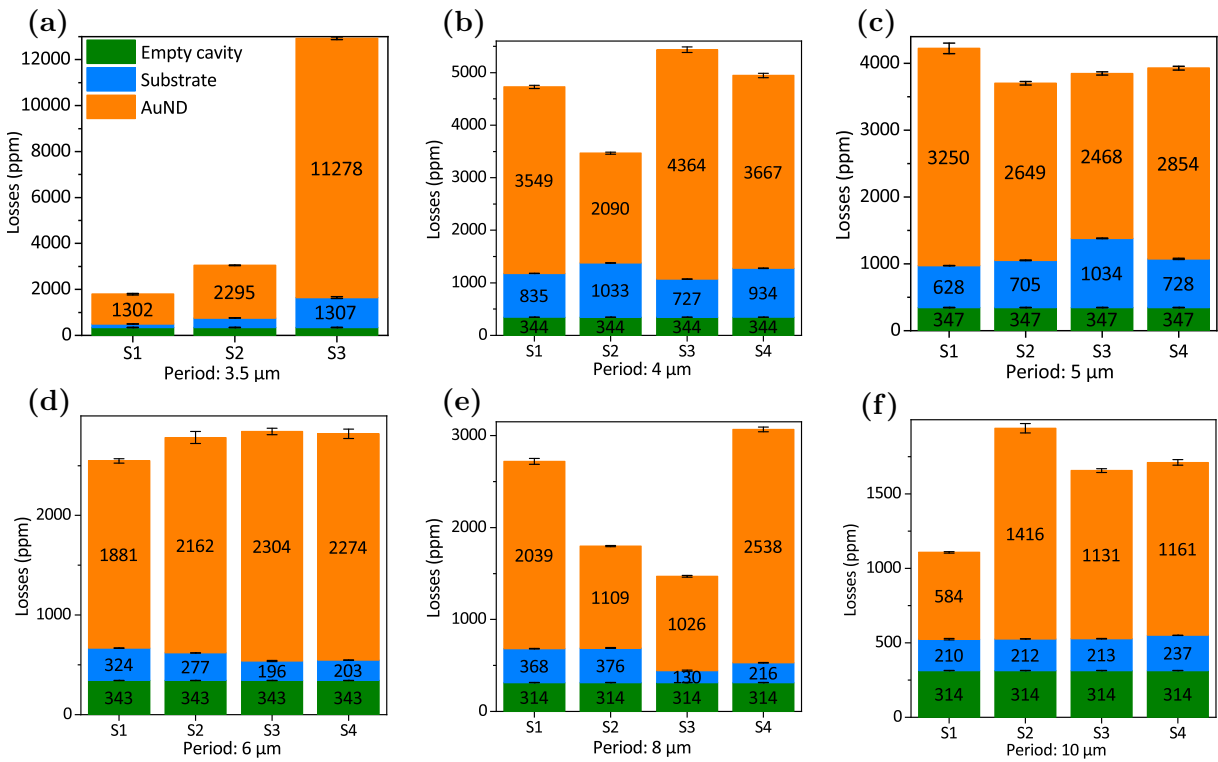


Figure 4.17: CRDS measurements of the gold nanodisc samples with long periods (from  $3.5\mu\text{m}$  to  $10\mu\text{m}$ ). The S1 to S4 columns of each subfigure correspond to different samples of a same period. The legend appearing in subfigure (a) applies to all subfigures; the colors of the bars signify the different contributions to the cavity losses (in parts per million).

**Empty cavity.** This value is fairly constant, as the only possible variations stem from small dissemblances in the daily cavity alignment.

**Substrate.** Although all samples are deposited onto the same fused silica wafer, there are some variations in substrate attenuation. Any manipulation during sample processing can lead to irregularities in transparency, but the most substantial dents and scratches on the substrates are most probably produced during the wafer cutting process. For this reason, each sample's substrate is measured independently on the half side without sample coverage.

**Gold nanodiscs.** The samples display a high uniformity, even when choosing different spots for each measurement, as hinted by the small error bars displayed on top of each column of figure 4.17. However, in some periods -specially  $3.5\mu m$  represented figure 4.17(a)- there are high irregularities from sample to sample. These seem to be originated from the manufacturing itself, as repeated measurements of the same sample result in coincidental values of the cavity losses.

In analogy to figure 4.15(b), the dependence between the longer period samples measured in CRDS and their attenuation is represented in figure 4.18. The calculation of the attenuation from the measured ring-down times is performed through equations (4.3) and (4.6) in section 4.1.2. Each squared point in figure 4.18 correspond to the average of all samples of each period presented in figure 4.17, from which the error bars are derived.

Similarly to the shorter period samples, the attenuation has a power dependency with the period, with exponent  $-1.52 \pm 0.13$ .

A further evaluation of the CRDS setup is developed at the subsequent discussion section, with a closer comparison of the attenuation measurements in CRDS with the attenuations retrieved by the UV-Vis spectrometer.

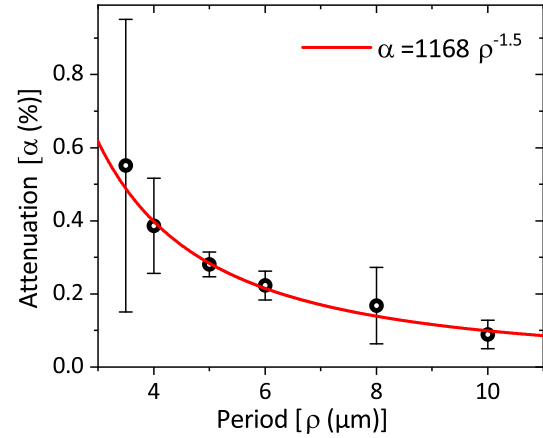


Figure 4.18: Attenuation as a function of the period for the samples with longer periods, measured with the CRDS setup.

#### 4.5.2 CRD-TAS: Coherent artifacts

The next logical step on the characterization of the CRD-TAS technique is to model the strong non-resonant signal that appears consistently in TAS measurements: the coherent artifact of transparent substrates. The physical mechanisms generating coherent artifacts are well known and mathematically defined. This allows for a thorough simulation of the signal that is to be matched and compared to the experimentally-retrieved data from CRD-TAS.

##### Substrates

CRD-TAS experiments are performed in three transparent substrates from different manufacturers and various thicknesses, as specified in table 4.4. With these means, the ability of the CRD-TAS setup to discern among distinctive coherent artifacts arising in similar materials will be probed.

Table 4.4: Sample materials and their specifications, as reported from manufacturers. [OH] content of borosilicate glass is not specified but a moderate amount of metallic impurities is expected, aside from the ~10% content of boric oxide.

Name	Glass type	Metallic impurities	[OH] content	Thickness (mm)
Infrasil (Heraeus)	IR grade	~25 ppm	<8 ppm	1
UVFS (Thorlabs)	UV grade	<1000 ppb	<1000 ppm	1
D236 (Schott)	Zink borosilicate	Very high	High	0.15

As demonstrated in table 4.4, the impurity content of each substrate depends strongly on the “type” of fused silica determined by the manufacturing technique. The [OH] impurities create different point-defects in amorphous silica glasses, from which new absorption bands originate in an a-priori transparent material [153].

### Simulations

The simulations of the experimental coherent artifacts are performed by a superposition of two nonlinear effects, XPM and TPA, with a higher contribution of TPA in those silica materials with an increased amount of [OH] impurities. Thus, the global TA signal of the coherent artifact  $\Delta A_{CA}$  is simulated by equation (4.13), where  $\Delta A_{TPA}$  and  $\Delta A_{XPM}$  represent the TA signals of TPA and XPM, respectively, and  $W_{TPA}$  represents the magnitude of the TPA contribution to the overall  $\Delta A_{CA}$  signal.

$$\Delta A_{CA} = W_{TPA} \cdot \Delta A_{TPA} + \Delta A_{XPM} \quad (4.13)$$

Hereunder, the physical origin of each nonlinearity is explained, in conjunction with the equation used for modelling the experimental data. The graphical result of the simulation is presented in figure 4.19 (in blue lines), superimposed to the experimental CRD-TAS

data.

**XPM** is a non-resonant electronic response of matter upon irradiation with an intense pump pulse, that induces a transient change of the refractive index of the material, modifying the spectral distribution of the probe pulse. This nonlinear effect is most evident when probing with chirped broadband supercontinuum pulses [73]. Hence, considering the experimental narrowband pump pulses employed in CRD-TAS, only a small contribution to the overall coherent artifact is expected, in comparison to TPA.

Nevertheless, the XPM signature appears in all different types of amorphous glasses, as it depends primarily on the nature of the interacting pulses [75]. Considering a constant  $C$ , pump and probe pulses with duration  $T_p$  and delayed by  $t_d$ , the central frequency of the probe  $\Omega$ , and  $\omega_i^{pr}$  each of its frequency components, the  $\Delta A$  signal generated through XPM is described by equation (4.14) as:

$$\Delta A_{XPM}(t_d, \omega_i^{pr}) = \sum_i C \exp \left[ T_p^2 \frac{(\Omega - \omega_i^{pr})}{3} \right] \exp \left[ -\frac{t_d^2}{3T_p^2} \right] \sin \left[ \frac{2}{3} t_d (\Omega - \omega_i^{pr}) \right] \quad (4.14)$$

In order to account for the narrowband filter used in front of the detection system of CRD-TAS it is useful to consider the proportional contribution of each singular wavelength to the total XPM signal. This results in a weighted sum of each of the transmitted frequency components of the probe [56], as exemplified by equation (4.14).

**TPA** is often neglected in fused silica since, in its pure composition, it is transparent in the visible range. In reality, even a small amount of impurities in fused silica cause the presence of intra-bandgap defect states [153]. Precisely, a moderate [OH] content induces an excess of oxygen atoms, that generate nonbridging oxygen hole centers. These

introduce a new absorption band at 4.8 eV (258 nm), allowing TPA to occur even for visible wavelengths by the simultaneous absorption of two photons, whose sum of energies falls below the high energy limit of the 4.8 eV absorption band [75, 80].

Moreover, borosilicate glasses contain a high amount of metallic impurities that introduce a sharp UV edge resulting in full absorption above 4 eV (below 310 nm). This supports a strong TPA contribution to the coherent artifact of borosilicate glasses when excited with pump and probe pulse energies that add up to the aforementioned value.

Based on these considerations, TPA is an expected nonlinearity adding onto the coherent artifact of the UVFS and the D236 substrates. The magnitude of this contribution varies strongly in each material, as the nature and density of defect states that trigger TPA depend on the amount impurities they contain.

For the purpose of simulating the TPA transient signal it is presumed that, at the pump wavelength, the response of the measured transparent materials is fast compared to the pulse duration. Assuming low-intensity plane waves propagating through the medium of thickness  $L$  as Gaussian pulses with intensity  $I(t_d)$ , the TAS signal produced solely by two photon absorption is described by equation (4.15) [80, 154], in which  $K_2$  is a constant containing the TPA coefficient  $\beta$ .

$$\Delta A_{TPA}(t_d) = K_1 \frac{\beta L I^2(t_d)}{1 + \beta L I(t_d)} \approx K_2 L I^2(t_d) \quad (4.15)$$

### CRD-TAS data

In figure 4.19 the CRD-TAS measurements of the three transparent substrates described in table 4.4 are displayed (in black circles), as well as the simulated kinetic traces of the



coherent artifacts for each material. The signal amplitude is expressed on two related ordinals: the left Y-axis represents the signal in terms of the ring-down time difference  $\Delta\tau$  in nanoseconds, and the right Y-axis displays the conversion of the  $\Delta\tau$  signal into the typical expression of TA signals,  $\Delta T/T$ , as explained in the earlier section 4.1.3, equation (4.11).

Figure 4.19(a) shows the coherent artifact recorded from the *Infrasil* substrate. Due to its purity, there are no absorption bands in the near UV and therefore neither linear nor nonlinear absorption are expected, when pumping at 485 nm. Hence, the coherent artifact signal generated in this material is expected to stem solely from XPM. Certainly, figure 4.19(a) presents a derivative-like feature that is characteristic for XPM signals, illustrating the transient phase shift around zero pump-probe delay [75]. The positive feature of the signal is slightly more intense than the negative; this asymmetry points to minor contributions of TPA to the overall artifact signal, which may arise from residual impurities at the surface of the substrate and/or unfocused pump-probe interactions happening before the pump and probe pulses enter the cavity.

Accordingly, the coherent nonlinear response of the UVFS substrate is described by a superposition of XPM and TPA, with a  $W_{TPA} = 0.2$ . Figure 4.19(b) demonstrates how a substrate with increased [OH] content introduces oxygen defects that induce intraband transitions in the UV, and thus allowing TPA at 485 nm. In borosilicate materials, the amount of metallic impurities and the [OH] content are increased to a macroscopically high amount, as reflected in table 4.4. As a consequence, the contribution of TPA introduced by these impurities overshadows the presence of XPM and dictates the shape of the coherent artifact entirely. This is demonstrated in figure 4.19(b), showing the positive-only coherent signal of a 150  $\mu m$  thin borosilicate substrate (D236 in table 4.4).

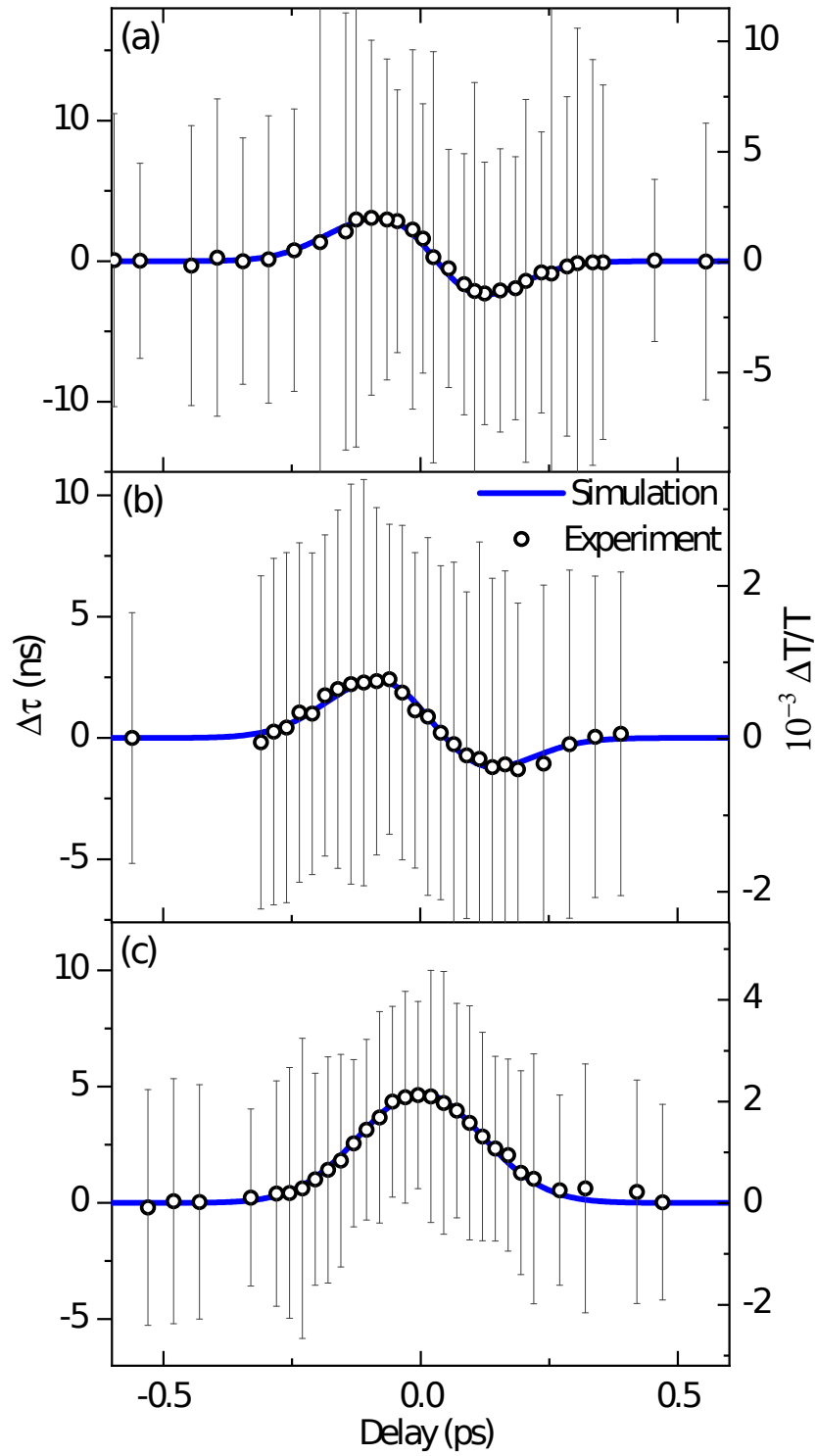


Figure 4.19: Coherent artifacts measured with the CRD-TAS technique (circles) and simulated signals (blue lines) for the three substrates of table 4.4: (a) Infrasil, (b) UVFS and (c) D236.

### 4.5.3 CRD-TAS: Samples

With the aim to demonstrate the full capabilities of the CRD-TAS technique in resolving resonant TA signals, graphene monolayers are measured in the CRD-TAS setup at 485 nm.

#### Graphene measurements at 485 nm

Figure 4.20 presents the results of measuring a graphene monolayer with the CRD-TAS technique at 485 nm. The blue line represents the smoothed set of data points (in blue dots).

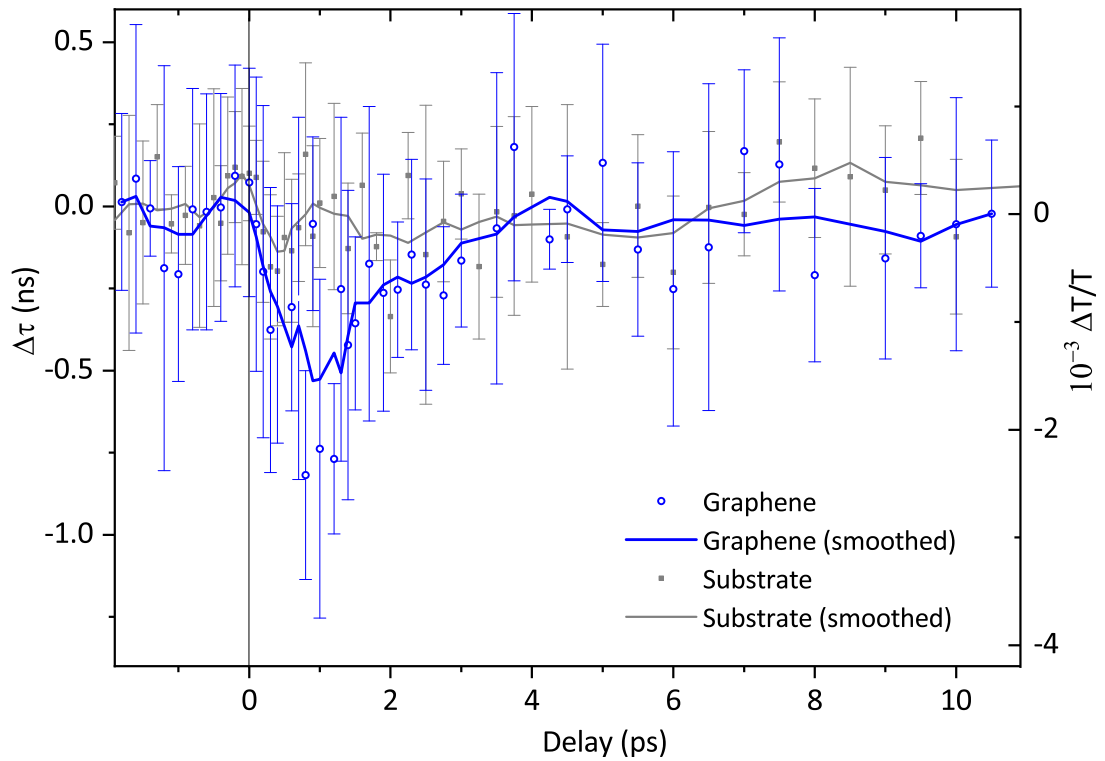


Figure 4.20: CRD-TAS measurements at 485 nm of a graphene monolayer (blue dots) with the smoothed fit (blue line) compared to the same measurements of a bare substrate (grey).

The measured TA signal of graphene presents high error bars in relation to the signal amplitude. The origin of the high levels of noise stems from the fact that  $\Delta\tau$  is retrieved from very low ring-down down times, below  $\tau = 0.2\mu s$ . This offers a limited number of round trips for fitting the exponential decay that provides the value of  $\tau$ , and consequently translates into a more unstable fit of the temporal decay of the intracavity pulse.

Thus, the experimental signal to noise ratio (SNR) is around the unity, which arises the need to use a signal smoothing technique<sup>6</sup> in the signal post-processing to allow for the analysis and fitting of the data. Nevertheless, the TA signal of graphene measured with CRD-TAS revealed a reproducible curve, that is consistently distinct from the measurements of the bare substrate, represented in grey in figure 4.20. As introduced in the previous section, the UVFS substrate only shows a short-lived coherent artifact signal.

These preliminary results present excited stated dynamics with a fitted monoexponential decay of  $2.7 \pm 1.5$  ps. Literature reports similar decay rates when exciting few-layer or monolayer graphene samples with 400 to 500 nm pump wavelengths. The few-ps decay is often considered a slow process in relation to other shorter lived excitations of graphene, and it has been assigned to a range of phonon effects: Ding et al. detected a 1.4 ps excitation and attributed it to an interaction of the phonons of graphene with excited electrons [155]; alternatively, Huang et al. found a 1.8 ps decay that is detectable only in few-layer measurements, which was assigned to hot phonon effects [156]; additionally, Oum et al. distinguished a 4 ps relaxation of the phonons in a graphene monolayer [157].

---

<sup>6</sup>The data was smoothed using the adjacent averaging method.

## 4.6 Discussion

The main interest of the discussion section of this chapter is to evaluate the capabilities of the techniques developed for CRDS and CRD-TAS. In this regard, it is relevant to assess the current resolution and sensitivity of the techniques, as well as their applicability to different types of solid state samples.

### 4.6.1 Evaluation of the steady state CRDS

The measurements of steady state CRDS of the samples with gold nanodiscs provided a consistent set of measurements of the attenuations provided by every period. The fact that only half of the substrate was covered by gold nanodiscs allowed an assessment of the substrate quality of each sample, and consequently a correct distinction between the sample attenuation and the extra losses provided by the varying substrate pristineness.

Figure 4.21 presents all attenuation measurements of the gold nanodiscs arranged in a single plot. It is important to recall that the samples with period below  $2 \mu m$  were measured with UV-Vis spectroscopy, and the samples with periods above  $3.5 \mu m$  are characterized with CRDS, as stated in table 4.3 of section 4.5. With this consideration, figure 4.21 emphasizes the high correlation between the attenuation measurements performed by the two different techniques, as all data points are in good correlation with the fitted power tendency, with exponent  $-1.7 \pm 0.1$ .

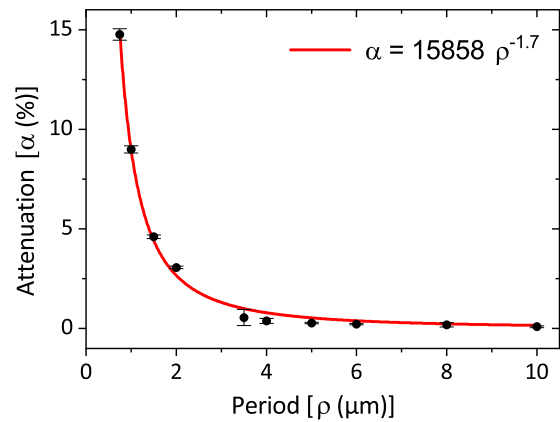


Figure 4.21: Attenuation of the gold nanodiscs measured with UV-Vis spectroscopy (until  $2 \mu m$  period) and CRDS (from  $3.5 \mu m$  period).

CRDS measurements of the longest period of gold nanodiscs samples revealed a capacity to resolve additional sample losses as low as 584 ppm, which corresponds to a sample attenuation of about 0.06 %.

Furthermore, the characterization of the losses provided by the substrates of the same samples (gold nanodiscs) proved a resolution beyond this value, as the smallest loss detected for a pristine substrate is only 130 ppm, with an error as low as 5 ppm. Therefore, it can be concluded that the CRDS setup constructed in the context of this thesis can achieve a maximum sensitivity of 5 ppm in steady state absorption measurements, corresponding to an attenuation of  $5 \cdot 10^{-4}$  %.

On the other end, the highest attenuation represented for the CRDS measurements in figure 4.18 corresponds to the sample with a period of  $3.5 \mu m$ , with an attenuation of 0.6 %. However, many gold nanodisc samples of the  $2 \mu m$  period with an average attenuation of 3% could also be characterized. Attenuation values above 3% presented a ring-down time with an insufficient number of round-trips to perform a fit of the exponential decay, resulting in inconsistent values of  $\tau$ .

### 4.6.2 Evaluation of the CRD-TAS

#### Detection of coherent artifacts

The elementary characterization of the CRD-TAS technique through the identification of different forms of coherent artifacts granted a successful description of the expected TA signals. These corroboration was made by comparing the experimental data with simulations of the nonlinear processes involved in the generation of coherent artifacts in fused silica. The contribution of each of these processes (TPA and XPM) to the global signal was successfully linked to the amount of impurities contained in each of the three

types of substrates that were analysed, which provided a solid physical explanation for each case.

In this preliminary evaluation, the smallest  $\Delta\tau$  difference that could be resolved with confidence is slightly below 0.2 ns, which corresponds to a  $\Delta T/T$  signal amplitude of  $6 \cdot 10^{-5}$ . This value is very close compared to the state-of-the-art highly-sensitive systems for TA measurements that use pulsed laser sources with low repetition rates [71, 158]. However, it does not reach the top-level sensitivity of almost  $10^{-7}$ , recently reported by Huang et al., that use a kHz source combined with the lock-in amplification method to minimize the noise of TA measurements of thin films [159].

#### 4.6.3 Evaluation of sample measurements

CRD-TAS measurements of graphene samples revealed TA signals that are found to be in good agreement with the literature, regarding the relaxation lifetimes of relatively slow processes in the few-ps range [155–157]. The aforementioned references also report a very low signal amplitude of this kinetic feature as it constitutes only a 10 to 20% contribution to the overall TA signal [156]. Other investigators report that the few-ps lifetime can only be confidently resolved in multilayered graphene samples, and becomes extremely noisy in graphene monolayers, to the point of being almost undetectable [157].

In this regard, the CRD-TAS technique shows a comparatively better performance in sensing this minor TA signal contribution of the monolayered graphene system. Conversely, shorter-lived excitations that are often reported in the literature could not be resolved in the CRD-TAS technique due to the limited time resolution for low values of pump-probe delay, as this contribution would be masked by the coherent artifact of the substrate.

A better SNR could potentially be achieved in a graphene monolayer that has a better homogeneity and/or that it is placed on a more transparent substrate. This consideration is based on the very low ring-down time retrieved from the graphene samples. The technical challenge that arises in these cases, is that the value of  $\tau$  must be retrieved from an exponentially decaying pulse that only completes about 40 round trips before the intensity becomes too low to be detected. As explained in previous section 4.3, a minimum of 20 to 30 round trips must be removed at the beginning of the ring-down decay, as they are intertwined with the electromagnetic noise of the Pockels cells of the laser system. This impracticable first round trips must be dismissed, which leaves only 10 to 15 peaks to fit the exponential decay. This represents a clear limitation in the upper boundary of sample attenuations that can be measured in CRD-TAS.

For this reason it is presumed that, if the ring-down times would be longer, the exponential fitting would be more robust, and the retrieval of the  $\Delta\tau$  signal would have lower uncertainty and an overall smoother appearance with lower SNR.

Considering the current stage of development of the CRD-TAS technique for resonant TA measurements, it would be unprofitable to assess the sensitivity achieved in this characterization of monolayered graphene, as the error bars are still too high. The following sections focus on the suggestions for further advancement on the performance of the novel CRD-TAS technique.

#### 4.6.4 Limitations of the CRD-TAS technique

The characterisation and evaluation process of the novel CRD-TAS method has brought to light the current limitations of the technique. In fact, some of these restrictions are intrinsic to the setup design, and bypassing them would require to revisit the arrangement



of the setup layout and possibly the data acquisition technique. Thereupon, these two concluding subsections are dedicated to explore the current limitations of the CRD-TAS method and evaluate their possible resolutions.

### **Intrinsic limitations of the setup design**

**Pump and probe pulses must propagate collinearly.** In order to obtain a multi-pass interaction, pump and probe pulses must spatially overlap at the sample in every round trip, ideally at the exact same spot if the sample is not homogeneous. This, aside from requiring an accurate alignment of the pump and probe beams, forbids to physically block the pump from entering the detector. Hence, another method for separating pump and probe pulses is required.

**Same polarization for pump and probe beams.** The design of a cavity that sustains several round trips with low losses requires the placement of samples in the Brewster angle, as it is the only configuration that allows **p**-polarized<sup>7</sup> pulses to be fully transmitted with virtually no reflection losses. This implies that there cannot be a relative polarization angle between pump and probe pulses and consequently, that the pump cannot be blocked from entering the detector by means of a polarizer.

**Broadband pulses are unsuitable.** Presumably the most inconvenient restriction is the incapability of the cavity to sustain the propagation of different wavelengths with equivalent losses. This limitation is partially imposed by the chromatic dispersion of the sample and substrate, i.e., the wavelength dependency of the refractive index  $n(\lambda)$ . Specifically:

---

<sup>7</sup>**p**-polarized light oscillates parallel to the plane of incidence, also called transverse-magnetic (TM).

1. The Brewster angle is different for every wavelength and therefore a precise angular setting for a sample only allows a very narrow spectral range to be transmitted without reflection losses. This does not only restrict the bandwidth but also the spectral distance between pump and probe pulses.
2. Regardless of the Brewster angle, every pass of the pump and probe pulses through the sample and substrate material creates a temporal mismatch between them, as the propagation speed differs for each wavelength. This implies that, if the wavelengths are too distant<sup>8</sup>, the accumulated mismatch after the  $n$ th round trip will forbid the pulses to temporally overlap at the  $(n+1)$  round trip. As this additional delay deprives the interaction that gives rise to the TA signal, it must be avoided at all costs.

Even though these effects can be minimized by selecting samples and substrates with low chromatic dispersion, an experimentally negligible dispersion is unattainable in practice, specially if the intention is to cover the entire visible range of wavelengths.

However, chromatic dispersion is not the only reason why the cavity cannot sustain the propagation of multiple wavelengths. At the present date, the development of thin-film coating technology for cavity mirrors has not quite achieved a high reflectivity ( $\geq 99.95\%$ ) that is uniform beyond a 50 nm wavelength range, within the visible range of wavelengths [160, 161]. It is worth mentioning that Silfies et al. recently reported technical advancements in their custom design of true broadband coatings for cavity mirrors with a reflectivity approaching 99.9 %. [162].

In any case it is noteworthy that, even if the limitation imposed by dispersion could be circumvented, the use of diverse wavelengths will still be limited by the working range

---

<sup>8</sup>This is aggravated with a thicker substrate and/or a substrate with high chromatic dispersion.

(with equal reflectivity values) of the cavity mirrors.

### Conditions for a sample to be measured with CRD-TAS

The following statements are not strong restrictions, but rather softer constraints regarding the choice of samples and substrates that can be measured in the current CRD-TAS setup.

1. **Substrates must be thin, transparent and with low chromatic dispersion.** In addition to the formerly discussed benefits of low dispersive materials, the choice of thin substrates also supports a more straightforward cavity alignment, as the lateral beam displacements (due to off-normal incidence angle) are minimized. Moreover, a thinner substrate provides a shorter interaction length of the pulses with the substrate material that, even if carefully chosen to have marginal absorption and scattering losses, is bound to be more lossy than the intracavity air.
2. **Maximum attenuation of 3 %.** Given the employed cavity parameters (detailed in tables 4.1 and 4.2), the current upper limit for the attenuation of a sample is 3 %, although the determination of a consistent  $\tau$  and  $\Delta\tau$  is optimal in the range of attenuations from 0.06 to 1 %. On a related note, one must consider that scattering and birefringent samples will not produce a comparable contrast in the differential TA signal, as the ground state losses provided by these effects lower the values of  $\tau$  without a corresponding contribution to a TA signal.
3. **Minimum sample size.** The minimum lateral size of a sample is restricted by the spot size of the measuring beams at the sample position. As the sample is placed at the Brewster angle ( $\approx 56^\circ$ ), the beam spot is projected onto the tilted sample surface, which makes the illuminated sample area to be elongated in the horizontal axis. Considering

the (largest) measurements of the spot size presented in section 4.4, the effective spot size at the sample surface and thus, the minimum sample dimensions corresponds to **640 x 520  $\mu\text{m}$** .

### Current empirical limitations of the CRD-TAS

At the present stage of the development of the CRD-TAS technique, there are some experimental characteristics and findings that have the potential to be further improved.

**Limited time resolution.** Narrowing the spectral bandwidth of the pump and probe pulses entails that the pulse duration is increased as a consequence of the time-bandwidth limit. Measuring with longer pulses decreases the time resolution of the CRD-TAS techniques, whose response function can be calculated equivalently to that of the TAS technique, explained in section 2.3.1. The measurements of coherent artifacts in the 485 nm setup (depicted in figure 4.19) demonstrate that sample dynamics faster than 250 fs would not be confidently resolved, as they would superimpose with the artifact. In consideration of the pulse durations in each setup (presented in section 4.4), it can be extrapolated that the setup at 800 nm would achieve a sub-ps resolution with an artifact duration of  $\approx 1$  ps.

**Noise and error bars.** The low SNR of the present CRD-TAS setup at 485 nm requires to average several pulses per point (8 to 12 sequences of 50 ring-down waveforms each) and on top of that, running 8 to 12 scans over the delay line. This procedure implies a long measuring time, e.g., each of the measurements presented in figures 4.19 and 4.20 required one full day (8 to 10 hours). Additionally, the data points in the aforementioned figures are contained within substantially broad error bars. The full length of the measured error bar represents one standard deviation (SD) of the  $\tau$  value averaged from the sequences

of ring-down waveforms in each delay position and each scan, for either pump or probe pulses. Through the statistical treatment, one obtains the mean SD (of all scans) of the  $\tau_p$  and  $\tau_{np}$  separately. As a result of the statistical combination of SDs of a differential magnitude, the final error bar of the  $\Delta\tau$  plotted in the graphs is roughly two times bigger than SD directly derived from the measurements of  $\tau$ .

#### 4.6.5 Further strategies for an improved CRD-TAS

The closing remarks of the chapter are dedicated to the discussion of some tactics that have the potential to develop into groundbreaking improvements in the efficiency and sensitivity of the novel CRD-TAS technique.

1. **Two non-collinear cavities.** One possible strategy to allow the pump excitation in a different wavelength region than that of the probe would be to build an additional cavity for the pump pulse propagation, in an experimental layout similar to the one proposed by Reber et al. [163]. Different angular orientations of the pump cavity would allow to transmit the pump pulses also in a Brewster configuration fitting to the specific pump wavelength of choice. However, such configuration also entails their own disadvantages: it would not only require an extremely precise alignment of each cavity to ensure a spatial overlap of the pulses, but also demands for a careful synchronisation of pump and probe pulses at the sample position for every round trip of the pulses inside their own cavities. Moreover, it does not solve the problem of the temporal mismatch of pulses caused by chromatic dispersion.
2. **Addition of a lock-in amplifier.** With the purpose of improving the detection sensitivity of the CRD-TAS method, a lock-in amplification technique could be employed, in combination with the presented CRD-TAS layout. Additionally to the

several investigations reporting the combination of lock-in amplification with TAS [14–16, 159] there is also literature dedicated to the successful combination of the lock-in technique with CRDS [164, 165]. One possible complication of the lock-in amplification is that the noise cancellation procedure is based on filtering out the fast frequency components of the signal with a low-pass filter. This would imply losing the single round trip oscillations below the exponentially decaying envelope. Nevertheless, it is in the envelope of the waveform where the relevant information, i.e., the ring-down times, is contained. Hence, one would need to take extra care on the selection of the cut-off frequency, so that the ring-down times are perfectly reproduced after the lock-in amplification, and that the frequency filtering does not remove any of the information encapsulated within the few- $\mu$ s ring-down decays.

3. **Re-injection cavity.** Leen et al. designed a cavity configuration for steady state CRDS with a so-called re-injection mirror in front of the cavity, placed at the specific distance that synchronises the beam injection in the cavity with its oscillation period [166]. Such layout allows a cavity operation similar to that of a Fabry-Pérot resonator with an amplified standing wave propagation. Therefore, the optical power outcoupled through the second cavity mirror increases by one order of magnitude or more. Such boost in the number of detected photons would increase the SNR and possibly allow a better determination of  $\tau$ . However, this would present other technical complications, as either the pulses should be elongated or the size of the cavity would have to be decreased for a standing wave operation, which would negatively impact on the time resolution of the system and/or the lifetime of the kinetics that could be measured in the CRD-TAS setup.

## 4.7 Conclusion

The present chapter has introduced the novel CRD-TAS methodology for the spectroscopic time-resolved characterisation of transparent substrates and thin films. First, a detailed description of the technique, the optical layout and the measuring software was presented, concluded by the explanation of the empirical methodology employed to characterize the setups. Subsequently, the experimental feasibility of two CRD-TAS setups at different wavelengths was demonstrated via steady state measurements of gold nanodisc samples, time-resolved measurements of coherent artifacts and the preliminary results of the excited state absorption of a monolayered graphene sample. Consequently, the presented work is contemplated as a proof of concept of the CRD-TAS technique for the sensitive detection of TA signals in optically very thin samples.

In consideration of the latter discussion section, the CRD-TAS method is considered to be at the midst of its development and has yet to reach its full potential. The combination of the present-day setup with a lock-in amplification machinery should advance on improving the SNR, aiding on a more time-efficient data collection and a shrinkage of the error bars. Moreover, it should also allow to detect lower TA signals and therefore increase the sensitivity even further.

The recommended strategies would presumably contribute to the further development of the here-demonstrated capabilities of the CRD-TAS methodology, ultimately revealing photochemical and structural information in investigations of the excited state absorption kinetics of molecularly (or atomically) thin films with very low optical density.

# Chapter 5

## Summaries

### 5.1 Summary

The work presented in this thesis is focused on the characterization of the excited state dynamics of two-dimensional semiconductor systems through time-resolved spectroscopy. As the conventional methodologies have a limited detection sensitivity, the last chapter is dedicated to the development of a methodology that can resolve weak transient absorption signals from optically thin films.

In the past four decades, the progressive improvement of powerful ultrafast lasers unfolded the development of transient absorption spectroscopy as a robust tool for probing short-lived photoreaction dynamics of atoms, molecules, complexes, and solid-state materials [11]. The investigation of semiconducting materials with transient absorption spectroscopy helps on revealing the nature of their photogenerated excitations and their relaxation pathways. This knowledge allows to understand and fine-tune their optical and



optoelectronic properties for the development of cutting-edge optoelectronic devices and photovoltaic systems.

With the aim of studying the exciton dynamics of van der Waals heterostructures and their individual semiconducting layers, the conventional transient absorption spectroscopy method is first utilized. Although these two-dimensional samples are physically thin, they presented very strong transient absorption signals in relation to their thickness. For this reason, their excited state dynamics could be characterized with the conventional machinery.

In a more general picture, two-dimensional samples with ordinary to low extinction coefficients do not present such a favourable ratio of high transient signals and low thickness. In fact, two-dimensional systems tend to present a very low optical density, and the detection of their weak absorption requires further amplification methods or noise-cleaning techniques. For this purpose, the cavity ring-down transient absorption spectroscopy (CRD-TAS) is proposed for the characterization of the excitonic properties of two-dimensional materials with low optical density and/or weak transient absorption signals. This novel technique has two advantages: On the one hand, the interaction length of the light with the thin sample is multiplied with the cavity-enhanced scheme. On the other hand, the calculation of the transient absorption is free from fluctuation instabilities of the laser source, as the differential attenuation is retrieved from the decay lifetimes of the intracavity pulses.

The proposed CRD-TAS methodology is, at the present time, in the midst of its development. The hereby presented results have demonstrated the capabilities of the technique to detect short-lived transient signals in transparent substrates [19]. Preliminary results on monolayered graphene have ascertained that CRD-TAS is suitable for the characterisation

of thin-film coatings and semiconducting layers. However, the detection sensitivity of the CRD-TAS is currently one order of magnitude below the state-of-the-art sensitivity of transient absorption techniques in the kHz range [159].

## 5.2 Zusammenfassung

In der vorliegenden Arbeit sollen die Dynamiken von Dünnschichtsystemen im angeregten Zustand mittels zeitaufgelöster Spektroskopie untersucht werden. Der Schwerpunkt liegt dabei auf der Entwicklung einer Methodik, mit der schwache transiente Absorptionssignale von optisch dünnen Filmen aufgelöst werden können. In den letzten vier Jahrzehnten hat die Entwicklung immer leistungstärkerer Ultrakurzpulslaser, die Etablierung der transienten Spektroskopie als robustes Werkzeug zur Untersuchung von kurzlebigen Photoreaktionsdynamiken von Atomen, Molekülen, Komplexen und Festkörpermateriale vorangetrieben [11]. Durch die Untersuchung von Halbleitermaterialien, können mittels dieser Technik wertvolle Informationen über die Natur von angeregten Zuständen, sowie möglicher Relaxationspfade erhalten werden. Mit diesem Wissen können deren optische und optoelektronische Eigenschaften in Zukunft besser verstanden und optimiert werden, sowie deren Eignung für künftigen avantgardische optoelektronische Geräte ermittelt werden. Zur Untersuchung der Exzitonendynamiken von van-der-Waals-Heterostrukturen und deren einzelnen Halbleiterschichten wird zunächst die herkömmliche Methode der transiente Spektroskopie angewandt. Obwohl diese zweidimensionalen Proben sehr dünn sind, weisen sie dennoch relativ starke transiente Absorptionssignale von einigen mOD (Einheiten der optischen Dichte) auf, die es ermöglichen, ihre Dynamik im angeregten Zustand mit der herkömmlichen Maschinerie zu charakterisieren, ohne dass zusätzliche Signalverstärkungen oder komplexe Techniken zur Rauschminimierung erforderlich sind. Dies lässt sich allerdings nicht auf die Mehrheit an zweidimensionalen Systeme übertragen, da diese dazu neigen, optisch sehr dünn zu sein, besonders wenn ihre molekularen (oder atomaren) Extinktionskoeffizienten gering sind. Daher ist es notwendig, eine Methode zu entwickeln, die die exzitonischen Eigenschaften von einschichtigen und Nanoblatt-Halbleitermaterialien mit geringer optischer Dichte und/oder schwachen transienten Ab-

sorptionssignalen charakterisieren kann. Hierzu, wird im letzten Kapitel dieser Arbeit ein neuer Ansatz für die sensitive Detektion von zweidimensionalen Proben mit marginalen molekularen Extinktionskoeffizienten vorgestellt: die Entwicklung einer neuartigen Methode, die die Wechselwirkungslänge des Lichts mit der Probe vervielfacht und als Cavity Ring-Down Transient Absorption Spectroscopy (CRD-TAS) bezeichnet wird [19]. Da sich die CRD-TAS-Methode derzeit noch in der Entwicklungsphase befindet, werden ihre Effizienz und ihre Einsatzmöglichkeiten bewertet und die Strategien für weitere Verbesserungen erörtert.

# Bibliography

- [1] K. S. Novoselov, A. K. Geim, S. V. Morozov, D. Jiang, Y. Zhang, S. V. Dubonos, I. V. Grigorieva, and A. A. Firsov, “Electric field effect in atomically thin carbon films,” *Science*, vol. 306, no. 5696, pp. 666–669, 2004.
- [2] K. S. Novoselov, D. Jiang, F. Schedin, T. J. Booth, V. V. Khotkevich, S. V. Morozov, and A. K. Geim, “Two-dimensional atomic crystals,” *Proceedings of the National Academy of Sciences*, vol. 102, no. 30, pp. 10451–10453, 2005.
- [3] “The nobel prize in physics 2010,” Nobel Prize Outreach AB 2023. Accessed on 12.04.2023.
- [4] A. K. Geim and K. S. Novoselov, “The rise of graphene,” *Nature materials*, vol. 6, no. 3, pp. 183–191, 2007.
- [5] E. Rajackaite, D. Peckus, R. Gudaitis, M. Andrulevičius, T. Tamulevičius, D. Volyniuk, Ąarunas Meškiniš, and S. Tamulevičius, “Transient absorption spectroscopy as a promising optical tool for the quality evaluation of graphene layers deposited by microwave plasma,” *Surface and Coatings Technology*, vol. 395, p. 125887, 2020.
- [6] X. Jiang, A. V. Kuklin, A. Baev, Y. Ge, H. Ågren, H. Zhang, and P. N. Prasad,

- “Two-dimensional mxenes: From morphological to optical, electric, and magnetic properties and applications,” *Physics Reports*, vol. 848, pp. 1–58, 2020.
- [7] X. Yu, X. Wang, F. Zhou, J. Qu, and J. Song, “2d van der waals heterojunction nanophotonic devices: From fabrication to performance,” *Advanced Functional Materials*, vol. 31, no. 42, p. 2104260, 2021.
- [8] M. Dantus and P. Gross, *Spectroscopy, Ultrafast*, ch. 1. John Wiley and Sons, Ltd, 2004.
- [9] J.-C. Diels and W. Rudolph, *Ultrashort laser pulse phenomena*. Elsevier, 2006.
- [10] “The nobel prize in chemistry 1999,” Nobel Prize Outreach AB 2023. Accessed on 12.04.2023.
- [11] A. H. Zewail, “Femtochemistry: Atomic-scale dynamics of the chemical bond using ultrafast lasers (nobel lecture),” *Angewandte Chemie International Edition*, vol. 39, no. 15, pp. 2586–2631, 2000.
- [12] L. X. Chen, X. Zhang, and M. L. Shelby, “Recent advances on ultrafast x-ray spectroscopy in the chemical sciences,” *Chem. Sci.*, vol. 5, pp. 4136–4152, 2014.
- [13] M. Hentschel, R. Kienberger, C. Spielmann, G. A. Reider, N. Milosevic, T. Brabec, P. Corkum, U. Heinzmann, M. Drescher, and F. Krausz, “Attosecond metrology,” *Nature*, vol. 414, no. 6863, pp. 509–513, 2001.
- [14] V. I. Klimov and D. W. McBranch, “Femtosecond high-sensitivity, chirp-free transient absorption spectroscopy using kilohertz lasers,” *Opt. Lett.*, vol. 23, no. 4, pp. 277–279, 1998.

- [15] D. P. Khatua, S. Gurung, A. Singh, S. Khan, T. K. Sharma, and J. Jayabalan, “Filtering noise in time and frequency domain for ultrafast pump–probe performed using low repetition rate lasers,” *Review of Scientific Instruments*, vol. 91, no. 10, p. 103901, 2020.
- [16] H. Ardekani, R. L. Wilmington, M. Vutukuru, Z. Chen, R. Brandt, A. k. Swan, and K. Gundogdu, “Broadband micro-transient absorption spectroscopy enabled by improved lock-in amplification,” *Review of Scientific Instruments*, vol. 92, no. 10, p. 104706, 2021.
- [17] K. F. Mak and J. Shan, “Photonics and optoelectronics of 2d semiconductor transition metal dichalcogenides,” *Nature Photonics*, vol. 10, no. 4, pp. 216–226, 2016.
- [18] B. Gburek and V. Wagner, “Influence of the semiconductor thickness on the charge carrier mobility in p3ht organic field-effect transistors in top-gate architecture on flexible substrates,” *Organic Electronics*, vol. 11, no. 5, pp. 814–819, 2010.
- [19] N. A. Calvet, W. Paa, and B. Dietzek-Ivanšić, “Cavity ring-down transient absorption spectroscopy (crd-tas): A proof of concept via detection of coherent artifacts of thin substrates,” *Optics and Laser Technology*, vol. 163, p. 109399, 2023.
- [20] R. L. Sutherland, *Handbook of Nonlinear Optics*. Optical Science and Engineering, Taylor and Francis, 2003.
- [21] R. W. Boyd, *Nonlinear Optics, Third Edition*. USA: Academic Press, Inc., 3rd ed., 2008.
- [22] M. Born, E. Wolf, A. B. Bhatia, P. C. Clemmow, D. Gabor, A. R. Stokes, A. M. Taylor, P. A. Wayman, and W. L. Wilcock, *Principles of Optics: Electromagnetic*

- Theory of Propagation, Interference and Diffraction of Light*. Cambridge University Press, 1999.
- [23] D. M. Siegel, *Innovation in Maxwell's Electromagnetic Theory: Molecular Vortices, Displacement Current and Light*. Cambridge University Press, 1992.
- [24] G. Grynberg, A. Aspect, C. Fabre, and C. Cohen-Tannoudji, *Introduction to Quantum Optics: From the Semi-classical Approach to Quantized Light*. Cambridge University Press, 2010.
- [25] A. Tip, “Linear dispersive dielectrics as limits of drude-lorentz systems,” *Phys. Rev. E*, vol. 69, p. 016610, 2004.
- [26] M. Born and R. Oppenheimer, “Zur quantentheorie der molekeln,” *Annalen der Physik*, vol. 389, no. 20, pp. 457–484, 1927.
- [27] C. Kittel, P. McEuen, and P. McEuen, *Introduction to solid state physics*, vol. 8. Wiley New York, 1996.
- [28] A. E. Siegman, *Lasers*. University Science Books, 1986.
- [29] P. Meystre and M. Sargent, *Elements of Quantum Optics*. Springer, 1991.
- [30] S. V. Sazonov, “On the approximations of slowly varying envelope and slowly varying profile in nonlinear optics,” *Journal of Physics: Conference Series*, vol. 859, 2017.
- [31] R. Loudon, *The Quantum Theory of Light*. OUP Oxford, 3rd ed., 2000.
- [32] C. F. Bohren and D. R. Huffman, *Absorption and Scattering of Light by Small Particles*. Wiley, 1998.



- [33] S. H. Wemple and M. DiDomenico, “Behavior of the electronic dielectric constant in covalent and ionic materials,” *Phys. Rev. B*, vol. 3, pp. 1338–1351, 1971.
- [34] J. Bros, *Dispersion Relations*. Oxford: Academic Press, 2006.
- [35] J. S. Toll, “Causality and the dispersion relation: Logical foundations,” *Phys. Rev.*, vol. 104, pp. 1760–1770, 1956.
- [36] R. Kanwal, *Linear Integral Equations*. Birkhäuser Boston, 1996.
- [37] J. J. Saarinen, “Generalized kramers-kronig relations and sum rules for moments and powers of degenerate four wave mixing susceptibility,” *Optical Review*, 2021.
- [38] C. F. Bohren, “What did kramers and kronig do and how did they do it?,” *European Journal of Physics*, vol. 31, no. 3, p. 573, 2010.
- [39] M. W. Haakestad and J. Skaar, “Causality and kramers-kronig relations for waveguides,” *Opt. Express*, vol. 13, no. 24, pp. 9922–9934, 2005.
- [40] H. Shim, F. Monticone, and O. D. Miller, “Fundamental limits to the refractive index of transparent optical materials,” *Advanced Materials*, vol. 33, no. 43, p. 2103946, 2021.
- [41] M. H. Lee and O. I. Sindoni, “Kramers-kronig relations with logarithmic kernel and application to the phase spectrum in the drude model,” *Phys. Rev. E*, vol. 56, pp. 3891–3896, 1997.
- [42] L. L. G. Celso, *Teaching wavepackets propagation via ultrashort pulses of light*. Optica Publishing Group, 2001.
- [43] P. J. Loughlin and L. Cohen, “The uncertainty principle: global, local, or both?,” *IEEE Transactions on Signal Processing*, vol. 52, pp. 1218–1227, 2004.

- [44] W. Heisenberg, “Über den anschaulichen inhalt der quantentheoretischen kinematik und mechanik,” *Zeitschrift für Physik*, vol. 43, pp. 172–198, 1927.
- [45] D. T. Smithey, M. Beck, J. Cooper, and M. G. Raymer, “Measurement of number-phase uncertainty relations of optical fields,” *Phys. Rev. A*, vol. 48, pp. 3159–3167, 1993.
- [46] E. Nava-Palomares, F. Acosta-Barbosa, S. Camacho-Lopez, and M. Fernandez-Guasti, “Femtosecond laser cavity characterization,” in *Laser Pulses* (I. Peshko, ed.), ch. 2, IntechOpen, 2012.
- [47] D. Popmintchev, S. Wang, X. Zhang, V. Stoev, and T. Popmintchev, “Analytical lah-laguerre optical formalism for perturbative chromatic dispersion,” *Opt. Express*, vol. 30, no. 22, pp. 40779–40808, 2022.
- [48] S. Kasap, *Principles of Electronic Materials and Devices*. USA: McGraw-Hill, Inc., 3 ed., 2005.
- [49] M. Göppert-Mayer, “Über elementarakte mit zwei quantensprüngen,” *Annalen der Physik*, vol. 401, no. 3, pp. 273–294, 1931.
- [50] T. Maiman, “Npg library,” *Nature*, vol. 187, pp. 493–494, 1960.
- [51] P. A. Franken, A. E. Hill, C. W. Peters, and G. Weinreich, “Generation of optical harmonics,” *Phys. Rev. Lett.*, vol. 7, pp. 118–119, 1961.
- [52] W. Kaiser and C. G. B. Garrett, “Two-photon excitation in  $\text{CaF}_2: \text{Eu}^{2+}$ ,” *Phys. Rev. Lett.*, vol. 7, pp. 229–231, 1961.
- [53] J. A. Armstrong, N. Bloembergen, J. Ducuing, and P. S. Pershan, “Interactions between light waves in a nonlinear dielectric,” *Phys. Rev.*, vol. 127, pp. 1918–1939, 1962.

- [54] S. S. Bulanov, T. Z. Esirkepov, A. G. R. Thomas, J. K. Koga, and S. V. Bulanov, “Schwinger limit attainability with extreme power lasers,” *Phys. Rev. Lett.*, vol. 105, p. 220407, 2010.
- [55] J. F. WARD, “Calculation of nonlinear optical susceptibilities using diagrammatic perturbation theory,” *Rev. Mod. Phys.*, vol. 37, pp. 1–18, 1965.
- [56] B. Dietzek, T. Pascher, V. Sundström, and A. Yartsev, “Appearance of coherent artifact signals in femtosecond transient absorption spectroscopy in dependence on detector design,” *Laser Physics Letters*, vol. 4, pp. 38–43, 2007.
- [57] M. Bass, *Handbook of optics: volume iv*. McGraw-Hill Education, 2010.
- [58] Y. R. Shen, *Fundamentals of Sum-Frequency Spectroscopy*. Cambridge University Press, 2016.
- [59] M. Houe and P. D. Townsend, “An introduction to methods of periodic poling for second-harmonic generation,” *Journal of Physics D: Applied Physics*, vol. 28, no. 9, p. 1747, 1995.
- [60] S. E. Harris, M. K. Oshman, and R. L. Byer, “Observation of tunable optical parametric fluorescence,” *Phys. Rev. Lett.*, vol. 18, pp. 732–734, 1967.
- [61] G. Cerullo and S. D. Silvestri, “Ultrafast optical parametric amplifiers,” *Review of Scientific Instruments*, vol. 74, pp. 1–18, 2003.
- [62] E. Garmire, “Nonlinear optics in daily life,” *Optics express*, vol. 21 25, pp. 30532–44, 2013.
- [63] A. S. Rao, “Overview on second and third order optical nonlinear processes,” 2016.

- [64] R. Alfano, *The Supercontinuum Laser Source: Fundamentals with Updated References*. Springer New York, 2006.
- [65] R. L. Fork, C. V. Shank, C. Hirlimann, R. Yen, and W. J. Tomlinson, “Femtosecond white-light continuum pulses,” *Opt. Lett.*, vol. 8, pp. 1–3, 1983.
- [66] J. Bennett, “A letter to the royal society presenting a new theory of light and colours.” <https://www.earlymoderntexts.com/assets/pdfs/newton1671.pdf>. Accessed on 05.04.2023.
- [67] *New Theory about Light and Colours*, p. 1–14. Cambridge Texts in the History of Philosophy, Cambridge University Press, 2 ed., 2014.
- [68] B. A. der Wissenschaften, *Denkschriften der Königlichen Akademie der Wissenschaften zu München*. No. v. 5, Die Akademie, 1817.
- [69] T. Levitt, “Spectrum of belief: Joseph von fraunhofer and the craft of precision optics,” *Isis*, vol. 93, pp. 739–740, 2002.
- [70] J. Lakowicz, *Principles of Fluorescence Spectroscopy*. Springer US, 2007.
- [71] R. Berera, R. van Grondelle, and J. Kennis, “Ultrafast transient absorption spectroscopy: principles and application to photosynthetic systems,” *Photosynthesis research*, vol. 101, no. 2, pp. 105–118, 2009.
- [72] C. Liu, H. Cao, and M. A. Choma, “Coherent artifact suppression in line-field reflection confocal microscopy using a low spatial coherence light source,” *Opt. Lett.*, vol. 41, no. 20, pp. 4775–4778, 2016.
- [73] M. Lorenc, M. Ziolek, R. Naskrecki, J. Karolczak, J. Kubicki, and A. Maciejewski, “Artifacts in femtosecond transient absorption spectroscopy,” *Applied Physics B*, vol. 74, pp. 19–27, 2002.

- [74] M. Lebedev, O. Misochko, T. Dekorsy, and N. Georgiev, “On the nature of coherent artifact,” *Journal of Experimental and Theoretical Physics*, vol. 100, pp. 272–282, 2005.
- [75] S. A. Kovalenko, A. L. Dobryakov, J. Ruthmann, and N. P. Ernsting, “Femtosecond spectroscopy of condensed phases with chirped supercontinuum probing,” *Physical review A*, vol. 59, no. 3, p. 2369, 1999.
- [76] S. Yan, M. T. Seidel, and H.-S. Tan, “Perturbed free induction decay in ultrafast mid-ir pump–probe spectroscopy,” *Chemical Physics Letters*, vol. 517, no. 1, pp. 36–40, 2011.
- [77] P. Hamm, “Coherent effects in femtosecond infrared spectroscopy,” *Chemical Physics*, vol. 200, no. 3, pp. 415–429, 1995.
- [78] K. Ekvall, P. van der Meulen, C. Dhollande, L.-E. Berg, S. Pommeret, R. Naskrecki, and J.-C. Mialocq, “Cross phase modulation artifact in liquid phase transient absorption spectroscopy,” *Journal of Applied Physics*, vol. 87, no. 5, pp. 2340–2352, 2000.
- [79] M. Ziolk, M. Lorenc, and R. Naskrecki, “Determination of the temporal response function in femtosecond pump-probe systems,” *Applied Physics B: Lasers and Optics*, vol. 72, pp. 843–847, 2001.
- [80] M. Rasmusson, A. Tarnovsky, E. Akesson, and V. Sundström, “On the use of two-photon absorption for determination of femtosecond pump–probe cross-correlation functions,” *Chemical Physics Letters*, vol. 335, pp. 201–208, 2001.
- [81] I. H. van Stokkum and R. Larsen, Delmar S. van Grondelle, “Global and target anal-

- ysis of time-resolved spectra,” *Biochimica et Biophysica Acta (BBA)-Bioenergetics*, vol. 1657, no. 2-3, pp. 82–104, 2004.
- [82] H. J. Wörner, C. A. Arrell, N. Banerji, A. Cannizzo, M. Chergui, A. K. Das, P. Hamm, U. Keller, P. M. Kraus, E. Liberatore, P. Lopez-Tarifa, M. Lucchini, M. Meuwly, C. Milne, J.-E. Moser, U. Rothlisberger, G. Smolentsev, J. Teuscher, J. A. van Bokhoven, and O. Wenger, “Charge migration and charge transfer in molecular systems,” *Structural Dynamics*, vol. 4, no. 6, p. 061508, 2017.
- [83] T. Zhu, T. Van Voorhis, and P. de Silva, *Charge Transfer in Molecular Materials*. Springer International Publishing, 2018.
- [84] S. Bettis Homan, V. K. Sangwan, I. Balla, H. Bergeron, E. A. Weiss, and M. C. Hersam, “Ultrafast exciton dissociation and long-lived charge separation in a photovoltaic pentacene–mos2 van der waals heterojunction,” *Nano Letters*, vol. 17, no. 1, pp. 164–169, 2017.
- [85] Z. Hu, X. Liu, P. L. Hernández-Martínez, S. Zhang, P. Gu, W. Du, W. Xu, H. V. Demir, H. Liu, and Q. Xiong, “Interfacial charge and energy transfer in van der waals heterojunctions,” *InfoMat*, vol. 4, no. 3, p. e12290, 2022.
- [86] Y. Yan, Z. Zeng, M. Huang, and P. Chen, “Van der waals heterojunctions for catalysis,” *Materials Today Advances*, vol. 6, p. 100059, 2020.
- [87] D. Davydova, A. de la Cadena, D. Akimov, and B. Dietzek, “Transient absorption microscopy: advances in chemical imaging of photoinduced dynamics,” *Laser and Photonics Reviews*, vol. 10, no. 1, pp. 62–81, 2016.
- [88] H. Marciniak and S. Lochbrunner, “On the interpretation of decay associated

- spectra in the presence of time dependent spectral shifts,” *Chemical Physics Letters*, vol. 609, no. 2-3, pp. 184–188, 2014.
- [89] S. Schott, A. Steinbacher, J. Buback, P. Nuernberger, and T. Brixner, “Generalized magic angle for time-resolved spectroscopy with laser pulses of arbitrary ellipticity,” *Journal of Physics B: Atomic, Molecular and Optical Physics*, vol. 47, no. 12, p. 124014, 2014.
- [90] K. S. Novoselov, A. Mishchenko, A. Carvalho, and A. H. C. Neto, “2d materials and van der waals heterostructures,” *Science*, vol. 353, no. 6298, p. aac9439, 2016.
- [91] A. K. Geim and I. V. Grigorieva, “Van der waals heterostructures,” *Nature*, vol. 499, no. 7459, pp. 419–425, 2013.
- [92] B. Zhao, Z. Gan, M. Johnson, E. Najafidehaghani, T. Rejek, A. George, R. H. Fink, A. Turchanin, and M. Halik, “2d van der waals heterojunction of organic and inorganic monolayers for high responsivity phototransistors,” *Advanced Functional Materials*, vol. 31, no. 42, p. 2105444, 2021.
- [93] Y.-Y. Lin, D. Gundlach, S. Nelson, and T. Jackson, “Stacked pentacene layer organic thin-film transistors with improved characteristics,” *IEEE Electron Device Letters*, vol. 18, no. 12, pp. 606–608, 1997.
- [94] C.-H. Kim and I. Kyminis, “Graphene–organic hybrid electronics,” *J. Mater. Chem. C*, vol. 5, pp. 4598–4613, 2017.
- [95] J. Yao and G. Yang, “Van der waals heterostructures based on 2d layered materials: Fabrication, characterization, and application in photodetection,” *Journal of Applied Physics*, vol. 131, no. 16, p. 161101, 2022.

- [96] E. Braun and S. MacDonald, *Revolution in Miniature: The History and Impact of Semiconductor Electronics*. Cambridge University Press, 1982.
- [97] J. L. Hood, *Chapter 2 - Tuners and radio receivers*. Oxford: Newnes, second edition ed., 1998.
- [98] D. J. Griffiths and D. F. Schroeter, *Introduction to Quantum Mechanics*. Cambridge University Press, 3 ed., 2018.
- [99] H. W. van Zeijl, “Thin film technologies for micro/nano systems; a review,” *ECS Transactions*, vol. 61, no. 3, p. 191, 2014.
- [100] F. Catania, H. D. S. Oliveira, P. Lugoda, G. Cantarella, and N. Münzenrieder, “Thin-film electronics on active substrates: review of materials, technologies and applications,” *Journal of Physics D: Applied Physics*, vol. 55, no. 32, 2022.
- [101] S. A. Holgate, *Understanding solid state physics*. Taylor and Francis, 2009.
- [102] P. Moontragoon, Z. Ikonić, and P. Harrison, “Band structure calculations of si-ge-sn alloys: achieving direct band gap materials,” *Semiconductor Science and Technology*, vol. 22, no. 7, p. 742, 2007.
- [103] W. Xia, L. Dai, P. Yu, X. Tong, W. Song, G. Zhang, and Z. Wang, “Recent progress in van der waals heterojunctions,” *Nanoscale*, vol. 9, pp. 4324–4365, 2017.
- [104] S. Shree, A. George, T. Lehnert, C. Neumann, M. Benelajla, C. Robert, X. Marie, K. Watanabe, T. Taniguchi, U. Kaiser, B. Urbaszek, and A. Turchanin, “High optical quality of mos2 monolayers grown by chemical vapor deposition,” *2D Materials*, vol. 7, no. 1, p. 015011, 2019.



- [105] A. George, C. Neumann, D. Kaiser, R. Mupparapu, T. Lehnert, U. Hübner, Z. Tang, A. Winter, U. Kaiser, I. Staude, and A. Turchanin, “Controlled growth of transition metal dichalcogenide monolayers using knudsen-type effusion cells for the precursors,” *Journal of Physics: Materials*, vol. 2, no. 1, p. 016001, 2019.
- [106] K. F. Mak, C. Lee, J. Hone, J. Shan, and T. F. Heinz, “Atomically thin  $\text{mos}_2$ : A new direct-gap semiconductor,” *Phys. Rev. Lett.*, vol. 105, p. 136805, 2010.
- [107] Ossila, “Molybdenum disulfide. theory and applications..” <https://www.ossila.com/en-eu/pages/molybdenum-disulfide-mos2>. Accessed on 22.11.2022.
- [108] X. Li and H. Zhu, “Two-dimensional  $\text{mos}_2$ : Properties, preparation, and applications,” *Journal of Materiomics*, vol. 1, no. 1, pp. 33–44, 2015.
- [109] S. B. Kalkan, E. Najafidehaghani, Z. Gan, F. A. C. Apfelbeck, U. Hübner, A. George, A. Turchanin, and B. Nickel, “Wafer scale synthesis of organic semiconductor nanosheets for van der waals heterojunction devices,” *2D Materials and Applications*, vol. 5, no. 1, pp. 1–6, 2021.
- [110] G. Moody, J. Schaibley, and X. Xu, “Exciton dynamics in monolayer transition metal dichalcogenides,” *J. Opt. Soc. Am. B*, vol. 33, no. 7, pp. C39–C49, 2016.
- [111] H. J. Conley, B. Wang, J. I. Ziegler, R. F. Haglund Jr, S. T. Pantelides, and K. I. Bolotin, “Bandgap engineering of strained monolayer and bilayer  $\text{mos}_2$ ,” *Nano letters*, vol. 13, no. 8, pp. 3626–3630, 2013.
- [112] P. Tonndorf, R. Schmidt, P. Böttger, X. Zhang, J. Börner, A. Liebig, M. Albrecht, C. Kloc, O. Gordan, D. R. T. Zahn, S. M. de Vasconcellos, and R. Bratschitsch,

- “Photoluminescence emission and raman response of monolayer mos2, mose2, and wse2,” *Opt. Express*, vol. 21, no. 4, pp. 4908–4916, 2013.
- [113] P. D. Cunningham, K. M. McCreary, A. T. Hanbicki, M. Currie, B. T. Jonker, and L. M. Hayden, “Charge trapping and exciton dynamics in large-area cvd grown mos2,” *The Journal of Physical Chemistry C*, vol. 120, no. 10, pp. 5819–5826, 2016.
- [114] A. R. Klots, A. K. M. Newaz, B. Wang, D. Prasai, H. Krzyżanowska, J. Lin, D. Caudel, N. J. Ghimire, J. Yan, B. L. Ivanov, K. A. Velizhanin, A. Burger, D. G. Mandrus, N. H. Tolk, S. T. Pantelides, and K. I. Bolotin, “Probing excitonic states in suspended two-dimensional semiconductors by photocurrent spectroscopy,” *Scientific Reports*, vol. 4, 2014.
- [115] Y. Ishino, K. Miyata, T. Sugimoto, K. Watanabe, Y. Matsumoto, T. Uemura, and J. Takeya, “Ultrafast exciton dynamics in dntt thin films,” *Phys. Chem. Chem. Phys.*, vol. 16, pp. 7501–7512, 2014.
- [116] M. Sawamoto, M. J. Kang, E. Miyazaki, H. Sugino, I. Osaka, and K. Takimiya, “Soluble dntt derivatives for solution-processed organic field-effect transistors,” *ACS Applied Materials and Interfaces*, vol. 8, no. 6, pp. 3810–3824, 2016.
- [117] S. Haas, Y. Takahashi, K. Takimiya, and T. Hasegawa, “High-performance dinaphtho-thieno-thiophene single crystal field-effect transistors,” *Applied Physics Letters*, vol. 95, no. 2, p. 022111, 2009.
- [118] J. Kan, S. Wang, Z. Wang, S. Guo, W. Wang, and L. Li, “Fabrication of flexible thin organic transistors by trace water assisted transfer method,” *Chinese Chemical Letters*, vol. 29, no. 11, pp. 1681–1684, 2018.

- [119] Z. Nie, Y. Wang, Z. Li, Y. Sun, S. Qin, X. Liu, I. Turcu, Y. Shi, R. Zhang, and Y. Ye, “Ultrafast free carrier dynamics in black phosphorus–molybdenum disulfide (bp/mos<sub>2</sub>) heterostructures,” *Nanoscale Horizons*, vol. 4, no. 5, pp. 1099–1105, 2019.
- [120] P. Schiettecatte, P. Geiregat, and Z. Hens, “Ultrafast carrier dynamics in few-layer colloidal molybdenum disulfide probed by broadband transient absorption spectroscopy,” *The Journal of Physical Chemistry C*, vol. 123, no. 16, pp. 10571–10577, 2019.
- [121] S. Sim, J. Park, J.-G. Song, C. In, Y.-S. Lee, H. Kim, and H. Choi, “Exciton dynamics in atomically thin mos<sub>2</sub>: Interexcitonic interaction and broadening kinetics,” *Phys. Rev. B*, vol. 88, p. 075434, 2013.
- [122] H. Shi, R. Yan, S. Bertolazzi, J. Brivio, B. Gao, A. Kis, D. Jena, H. G. Xing, and L. Huang, “Exciton dynamics in suspended monolayer and few-layer mos<sub>2</sub> 2d crystals,” *ACS nano*, vol. 7, no. 2, pp. 1072–1080, 2013.
- [123] H. Wang, J. H. Strait, C. Zhang, W. Chan, C. Manolatou, S. Tiwari, and F. Rana, “Fast exciton annihilation by capture of electrons or holes by defects via auger scattering in monolayer metal dichalcogenides,” *Phys. Rev. B*, vol. 91, p. 165411, 2015.
- [124] G. Soavi, F. Scotognella, D. Brida, T. Hefner, F. Spath, M. R. Antognazza, T. Hertel, G. Lanzani, and G. Cerullo, “Ultrafast charge photogeneration in semiconducting carbon nanotubes,” *The Journal of Physical Chemistry C*, vol. 117, no. 20, pp. 10849–10855, 2013.
- [125] K. Miyata, S. Tanaka, Y. Ishino, K. Watanabe, T. Uemura, J. Takeya, T. Sugimoto,

- and Y. Matsumoto, “Microscopic hole-transfer efficiency in organic thin-film transistors studied with charge-modulation spectroscopy,” *Physical Review B*, vol. 91, no. 19, p. 195306, 2015.
- [126] A. Barik, M. Bapna, D. Drabold, and K. Adarsh, “Ultrafast light induced unusually broad transient absorption in the sub-bandgap region of gese2 thin film,” *Scientific reports*, vol. 4, p. 3686, 2014.
- [127] X. Zhou, X. Hu, S. Zhou, Q. Zhang, H. Li, and T. Zhai, “Ultrathin 2d gese2 rhombic flakes with high anisotropy realized by van der waals epitaxy,” *Advanced Functional Materials*, vol. 27, no. 47, p. 1703858, 2017.
- [128] A. O’Keefe and D. A. G. Deacon, “Cavity ring-down optical spectrometer for absorption measurements using pulsed laser sources,” *Review of Scientific Instruments*, vol. 59, no. 12, pp. 2544–2551, 1988.
- [129] A. O’Keefe, J. J. Scherer, J. B. Paul, and R. J. Saykally, *Cavity Ringdown Laser Spectroscopy (CRDS) : History, Development and Applications*. John Wiley and Sons Chichester, UK, 2002.
- [130] D. Romanini and K. K. Lehmann, “Ring-down cavity absorption spectroscopy of the very weak hcn overtone bands with six, seven, and eight stretching quanta,” *The Journal of Chemical Physics*, vol. 99, no. 9, pp. 6287–6301, 1993.
- [131] R. T. Jongma, M. G. H. Boogaarts, I. Holleman, and G. Meijer, “Trace gas detection with cavity ring down spectroscopy,” *Review of Scientific Instruments*, vol. 66, no. 4, pp. 2821–2828, 1995.
- [132] A. O’Keefe and O. Lee, “Trace gas analysis by pulsed laser absorption spectroscopy,” *American Laboratory*, vol. 21, no. 12, pp. 19–22, 1989.

- [133] R. Engeln, G. von Helden, A. J. A. van Roij, and G. Meijer, "Cavity ring down spectroscopy on solid  $c_{60}$ ," *The Journal of Chemical Physics*, vol. 110, no. 5, pp. 2732–2733, 1999.
- [134] D. Kleine, J. Lauterbach, K. Kleinermanns, and P. Hering, "Cavity ring-down spectroscopy of molecularly thin iodine layers," *Applied Physics B*, vol. 72, pp. 249–252, 2001.
- [135] S. L. Logunov, "Cavity ringdown detection of losses in thin films in the telecommunication wavelength window," *Applied optics*, vol. 40, no. 9, pp. 1570–1573, 2001.
- [136] G. A. Marcus and H. A. Schwettman, "Cavity ringdown spectroscopy of thin films in the mid-infrared," *Applied optics*, vol. 41, no. 24, pp. 5167–5171, 2002.
- [137] A. Smets, J. van Helden, and M. van de Sanden, "Bulk and surface defects in a-si:h films studied by means of the cavity ring down absorption technique," *Journal of Non-Crystalline Solids*, vol. 299-302, pp. 610–614, 2002.
- [138] T. C. Yu and M.-C. Lin, "Kinetics of the  $c_6h_5 + o_2$  reaction at low temperatures," *Journal of the American Chemical Society*, vol. 116, pp. 9571–9576, 1994.
- [139] T. Yu and M.-C. Lin, "Kinetics of phenyl radical reactions studied by the cavity-ring-down method," *Journal of the American Chemical Society*, vol. 115, no. 10, pp. 4371–4372, 1993.
- [140] A. J. Alexander, "Reaction kinetics of nitrate radicals with terpenes in solution studied by cavity ring-down spectroscopy," *Chemical physics letters*, vol. 393, no. 1-3, pp. 138–142, 2004.
- [141] D. Melnik and T. A. Miller, "Kinetic measurements of the  $c_2h_5o_2$  radical using time-

- resolved cavity ring-down spectroscopy with a continuous source,” *The Journal of Chemical Physics*, vol. 139, no. 9, p. 094201, 2013.
- [142] M. C. Silfies, G. Kowzan, N. Lewis, and T. K. Allison, “Broadband cavity-enhanced ultrafast spectroscopy,” *Phys. Chem. Chem. Phys.*, vol. 23, pp. 9743–9752, 2021.
- [143] T. K. Allison, “Cavity-enhanced ultrafast two-dimensional spectroscopy using higher order modes,” vol. 50, no. 4, p. 044004, 2017.
- [144] D. Z. Anderson, J. C. Frisch, and C. S. Masser, “Mirror reflectometer based on optical cavity decay time,” *Applied optics*, vol. 23, no. 8, pp. 1238–1245, 1984.
- [145] G. Berden and R. Engeln, *Cavity ring-down spectroscopy: techniques and applications*. John Wiley and Sons, 2009.
- [146] K. K. Lehmann and D. Romanini, “The superposition principle and cavity ring-down spectroscopy,” *The Journal of Chemical Physics*, vol. 105, no. 23, pp. 10263–10277, 1996.
- [147] P. Zalicki and R. N. Zare, “Cavity ring-down spectroscopy for quantitative absorption measurements,” *The Journal of Chemical Physics*, vol. 102, no. 7, pp. 2708–2717, 1995.
- [148] T. Stacewicz, J. Wojtas, Z. Bielecki, M. Nowakowski, J. Mikołajczyk, R. Medrzycki, and B. Rutecka, “Cavity ring down spectroscopy: detection of trace amounts of substance,” *Opto-Electronics Review*, vol. 20, no. 1, pp. 53–60, 2012.
- [149] B. E. Saleh and M. C. Teich, *Fundamentals of photonics*. Wiley and sons, 2019.
- [150] A. Gerrard and J. M. Burch, *Introduction to matrix methods in optics*. Courier Corporation, 1994.

- [151] T. L. Corporation, *LeCroy Waverunner Xi Series*. Chestnut Ridge, New York, U.S., Sep. 2006.
- [152] Hamamatsu, *Hamamatsu Photosensor Modules H6780*. 314-5, Shimokanzo, Toyooka-village, Iwata-gun, Shizuoka-ken, 438-0193, Japan, Sep. 2001.
- [153] L. Skuja, “Optically active oxygen-deficiency-related centers in amorphous silicon dioxide,” *Journal of Non-crystalline Solids*, vol. 239, no. 1-3, pp. 16–48, 1998.
- [154] D. N. Nikogosyan, A. A. Oraevsky, and V. I. Rupasov, “Two-photon ionization and dissociation of liquid water by powerful laser uv radiation,” *Chemical Physics*, vol. 77, no. 1, pp. 131–143, 1983.
- [155] Q. Ding, Y. Shi, M. Chen, H. Li, X. Yang, Y. Qu, W. Liang, and M. Sun, “Ultrafast dynamics of plasmon-exciton interaction of ag nanowire-graphene hybrids for surface catalytic reactions,” *Scientific reports*, vol. 6, no. 1, pp. 1–10, 2016.
- [156] L. Huang, G. V. Hartland, L.-Q. Chu, Luxmi, R. M. Feenstra, C. Lian, K. Tahy, and H. Xing, “Ultrafast transient absorption microscopy studies of carrier dynamics in epitaxial graphene,” *Nano Letters*, vol. 10, no. 4, pp. 1308–1313, 2010.
- [157] K. Oum, T. Lenzer, M. Scholz, D. Y. Jung, O. Sul, B. J. Cho, J. Lange, and A. Müller, “Observation of ultrafast carrier dynamics and phonon relaxation of graphene from the deep-ultraviolet to the visible region,” *The Journal of Physical Chemistry C*, vol. 118, no. 12, pp. 6454–6461, 2014.
- [158] M. Murai, Y. Tamaki, A. Furube, K. Hara, and R. Katoh, “Reaction of holes in nanocrystalline  $\text{tio}_2$  films evaluated by highly sensitive transient absorption spectroscopy,” *Catalysis today*, vol. 120, no. 2, pp. 214–219, 2007.

- [159] H. Li, G. Hu, B.-H. Li, W. Zeng, J. Zhang, X. Wang, C. Zhou, Z. Ren, and X. Yang, “Ultrahigh sensitive transient absorption spectrometer,” *Review of Scientific Instruments*, vol. 92, no. 5, p. 053002, 2021.
- [160] J. Chen, D. P. Fullam, S. Yu, O. Böge, P. H. Le, H. Herrmann, and D. S. Venables, “Improving the accuracy and precision of broadband optical cavity measurements,” *Spectrochimica Acta Part A: Molecular and Biomolecular Spectroscopy*, vol. 218, pp. 178–183, 2019.
- [161] E. Optics, “Reflectivity: More complicated than it seems.” <https://www.edmundoptics.com/knowledge-center/trending-in-optics/high-reflectivity-mirrors/>. Accessed on 18.04.2023.
- [162] M. C. Silfies, G. Kowzan, Y. Chen, N. Lewis, R. Hou, R. Baehre, T. Gross, and T. K. Allison, “Widely tunable cavity-enhanced frequency combs,” *Opt. Lett.*, vol. 45, no. 7, pp. 2123–2126, 2020.
- [163] M. A. R. Reber, Y. Chen, and T. K. Allison, “Cavity-enhanced ultrafast spectroscopy: ultrafast meets ultrasensitive,” *Optica*, vol. 3, no. 3, pp. 311–317, 2016.
- [164] T. G. Spence, C. C. Harb, B. A. Paldus, R. N. Zare, B. Willke, and R. L. Byer, “A laser-locked cavity ring-down spectrometer employing an analog detection scheme,” *Review of Scientific Instruments*, vol. 71, no. 2, pp. 347–353, 2000.
- [165] T. K. Boyson, T. G. Spence, M. E. Calzada, and C. C. Harb, “Frequency domain analysis for laser-locked cavity ringdown spectroscopy,” *Opt. Express*, vol. 19, no. 9, pp. 8092–8101, 2011.
- [166] J. B. Leen and A. O’Keefe, “Optical re-injection in cavity-enhanced absorption spectroscopy,” *Review of Scientific Instruments*, vol. 85, no. 9, p. 093101, 2014.



### **Selbständigkeitserklärung**

Ich erkläre, dass ich die vorliegende Arbeit selbständig und unter Verwendung der angegebenen Hilfsmittel, persönlichen Mitteilungen und Quellen angefertigt habe.

Jena, 04.09.2023

Neus Allande Calvet

